Efficient Space Domain Method of Moments for Large Arbitrary Scatterers in Planar Stratified Media

Jagath Kumara Halpe Gamage

A dissertation submitted in partial fulfillment
of the requirements for the degree of *Doktor Ingeniør*

Report No 420403
Department of Electronics and Telecommunications
Norwegian University of Science and Technology
N-7491 Trondheim, Norway
June, 2004

Contents

Abstract xv

Preface xvii

Acknowledgment xix

Nomenclature xxi

Abbreviation xxiii

1 Introduction 1

- 1.1 Motivation 2
- 1.2 Outline 2
  - 1.2.1 Chapter 2 : Green's functions for stratified media 3
  - 1.2.2 Chapter 3 : Discrete complex image method 3
  - 1.2.3 Chapter 4 : Method of moments 3
  - 1.2.4 Chapter 5 : Numerical evaluations in MoM 3
  - 1.2.5 Chapter 6 : CG-FFT 3
  - 1.2.6 Chapter 7 : De-embedding techniques 4
  - 1.2.7 Chapter 8 : Results 4
  - 1.2.8 Chapter 9 : Discussion and conclusions 4

2 Green's Functions for Stratified Media 5

- 2.1 Introduction 5
- 2.2 Dyadic Green's Function 6
- 2.3 Spectral Green's Functions vs Spatial Green's Functions 7

2.3.1 Two-dimensional Fourier transformation 8

2.4 Mixed Potential Integral Equation 9

2.4.1 Maxwell's equations 9

2.4.2 Continuity equation 9

2.4.3 Potentials 10

2.4.4 Integral equation method 11

2.4.5 Electric field integral equation 11

2.4.6 Mixed potential formulation 12

2.5 Field Propagation in Stratified Media 14

2.6 Unified Transmission Line Theory for Spectral Green's Functions 14

2.6.1 Electric sources in multilayer media 18

2.6.2 Horizontal electric dipole 20

2.7 Characteristics of Spectral Green's Functions for a Stratified Medium . . 21

2.8 Numerical Evaluation of Spatial Green's Functions 23

2.8.1 Sommerfeld integrals 24

2.8.2 Numerical evaluation of Sommerfeld integrals 25

2.8.3 Methods for accelerating the numerical evaluations 25

2.8.4 Surface and space wave components 28

3 Discrete Complex Image Method 33

3.1 Introduction 33

3.2 Discrete Complex Image Method 34

3.2.1 Original approach 34

3.2.2 Robust approach 34

3.2.3 Methods for extracting exponential functions 41

3.2.4 Prony's method 41

3.2.5 Generalized pencil-of-functions method 44

3.2.6 Prony's method vs GPOF method 47

3.3 On the Implementation of DCIM 48

3.4 Exact vs Approximated Spatial Green's Functions 48

3.5 Comments on Numerical Stability and Convergence 49

3.6 Advantages and Limitations of Robust-DCIM 53

4 Method of Moments 55

4.1 Introduction . . . 55

4.2 General Formulation . . . 55

4.3 Basis and Testing Functions . . . 57

4.3.1 Entire domain functions . . . 57

4.3.2 Subdomain functions . . . 58

4.3.3 Galerkin's method . . . 58

4.4 Application of MoM to Stratified Media . . . 58

4.4.1 Space domain method of moments . . . 58

4.4.2 Admissible class of basis and testing functions for MoM . . . 61

4.4.3 Simplifying the elements in Z . . . 61

4.4.4 Symmetries exist in impedance matrix Z . . . 63

5 Numerical Evaluations in MoM 65

5.1 Introduction . . . 65

5.2 Quadrature Integration . . . 65

5.2.1 Gaussian quadrature integration . . . 66

5.2.2 Adaptive quadrature integration . . . 66

5.2.3 Quadrature method in our implementation . . . 67

5.3 Evaluating Two-Dimensional Generalized Exponential Integral . . . 67

5.3.1 Theory . . . 67

5.3.2 Accuracy and efficiency . . . 70

5.3.3 Applications . . . 71

6 Conjugate Gradient Fast Fourier Transform Method 75

6.1 Introduction . . . 75

6.2 Direct Methods vs Iterative Methods . . . 76

6.2.1 Direct methods . . . 76

6.2.2 Iterative methods . . . 76

6.3 Basic Conjugate Gradient Method . . . 77

6.3.1 Adjoint operator . . . 77

6.3.2 CGM algorithm . . . 77

6.4 Conjugate Gradient Method Combined with Fast Fourier Transform . . . 79

6.4.1 Discrete Fourier transform 79
6.4.2 More on convolution property of DFT 82
6.4.3 Practical 2D CG-FFT implementation 87
6.4.4 Convergence and accuracy of 2D CG-FFT 88

7 De-embedding Techniques 95
7.1 Introduction 95
7.1.1 De-embedding 95
7.1.2 Scattering (S) parameters 95
7.1.3 Common feeding techniques 97
7.2 Different De-embedding Techniques 98
7.2.1 A method based on transmission line theory 100
7.2.2 A method based on Prony's method 101
7.2.3 A method based on GPOF method 101
7.2.4 Example 1: Microstrip patch antenna 101
7.2.5 Example 2 : Two patches close to each other 104

8 Results 111
8.1 Introduction 111
8.2 Application to Linear Patch Antenna Array 111
8.2.1 Stand alone patch antenna with inset microstrip line feed 111
8.2.2 Linear antenna array consisting of three patches 112
8.3 Application to Finite Frequency Selective Surfaces 115
8.3.1 Introduction 115
8.3.2 Element structure : Jerusalem cross 123

9 Discussion and Conclusions 131
9.1 Discussion 131
9.2 Conclusions 132
9.3 Suggestions for Future Work 133
9.3.1 Implementation 133
9.3.2 Discrete complex image method 133
9.3.3 Method of moments 134

9.3.4 De-embedding 134

Appendix **135**

9.4 List of publications 135

References **135**

List of Figures

2.1 Simple one section transmission line 15

2.2 Stratified medium with infinitesimal HED 16

2.3 Cascaded sections of transmission line 17

2.4 Spectral Green's function of a thin grounded dielectric layer 21

2.5 Magnitude of spectral Green's function 22

2.6 Real part of spectral Green's function 22

2.7 Imaginary part of spectral Green's function 23

2.8 A HED on a stratified medium 24

2.9 Sommerfeld integration path of a typical spectral Green's function 25

2.10 Modified Sommerfeld integration path 25

2.11 Behavior of modified SIP near singular points of spectral GF 26

2.12 Modified SIP separating surface and space waves 26

2.13 A typical Green's function along SIP and modified SIP 27

2.14 Magnitude of the spatial Green's function of a thin grounded dielectric layer 29

2.15 Magnitude of the spatial Green's function of a thick grounded dielectric layer 30

2.16 Phase of the spatial Green's function of a thin grounded dielectric layer . 31

2.17 Phase of the spatial Green's function of a thick grounded dielectric layer . 31

3.1 Discrete complex image method : A block diagram 35

3.2 The integration contours on the complex k_{zs} plan 37

3.3 The integration contours on the complex k_ρ plan 37

3.4 Static and dynamic parts of a typical spectral Green's function 49

3.5 Dynamic part of a typical spectral Green's function 50

3.6 Static part of a typical spectral Green's function 50

3.7 Static part compared with its approximation 51
3.8 Residue of the dynamic part compared with its approximation 51
3.9 Magnitude of the spatial scalar Green's function 52
3.10 Phase of the spatial scalar Green's function 52

4.1 Simple planar metallic structure on a grounded substrate 59
4.2 Basis functions representing current densities 60
4.3 Example of a piecewise continuous cross-correlation function 62

5.1 Two-dimensional generalized exponential integral 69
5.2 Accuracy in evaluating 2D-GEI 71
5.3 Efficiency in evaluating 2D-GEI 72
5.4 Rectangular plate in the presence of x-polarized plane wave 72
5.5 Normalized magnitude of the surface x-current density 73
5.6 Normalized magnitude of the surface y-current density 73
5.7 Normalized magnitude of the induced surface x-current density in [1] . . . 74
5.8 Normalized magnitude of the induced surface y-current density in [1] . . . 74

6.1 Discret function x(n) 79
6.2 DFT of the discret x(n) 79
6.3 FFT vs DFT : Number of complex multiplications 83
6.4 FFT vs DFT : Number of complex additions 84
6.5 Monotonic decrease of residue norms vs iterations 89
6.6 Surface x-current density on a square patch 90
6.7 Surface y-current density on a square patch 90
6.8 Surface x-current density along xx 91
6.9 Surface x-current density along yy 91
6.10 CG-FFT vs direct matrix inversion : J_x along xx 92
6.11 CG-FFT vs direct matrix inversion : J_x along yy 93

7.1 An arbitrary N-port network 96
7.2 Common feeding techniques for patch antenna element 97
7.3 Current standing wave pattern on a stripline 99
7.4 Wave propagation in a transmission line 99

7.5 Stand alone patch antenna 102
7.6 Comparing results for a single patch 102
7.7 Normalized x-current density induced on a patch 103
7.8 Normalized y-current density induced on a patch 103
7.9 Normalized total current density induced on a patch 104
7.10 Two patches closer to each other 105
7.11 Comparing S_{11} results for two patch array 106
7.12 Comparing S_{12} results for two patch array 107
7.13 Normalized x-current density induced on two patch array 108
7.14 Normalized y-current density induced on two-patch array 108
7.15 Normalized total current density induced on two-patch array 109

8.1 Layout of the patch antenna fed by microstrip line 112
8.2 Prototyped inset patch antenna 113
8.3 Measured and simulated S_{11} of the stand alone patch 113
8.4 x-directed surface current density on the stand alone patch 114
8.5 y-directed surface current density on the stand alone patch 114
8.6 Total surface current density on the stand alone patch 115
8.7 Layout of the linear array consisting of three equivalent patches 116
8.8 Prototyped linear patch array 117
8.9 x-directed surface current density on the linear patch array 118
8.10 y-directed surface current density on the linear patch array 118
8.11 Total surface current density on the linear patch array 119
8.12 Measured and simulated S_{11} of the linear patch array 120
8.13 Measured and simulated S_{22} of the linear patch array 120
8.14 Measured and simulated S_{33} of the linear patch array 121
8.15 Measured and simulated S_{12} of the linear patch array 121
8.16 Measured and simulated S_{13} of the linear patch array 122
8.17 Measured and simulated S_{23} of the linear patch array 122
8.18 The layout of the loaded Jerusalem cross 123
8.19 A plane wave incident on an array of Jerusalem crosses 123
8.20 Grid applied for a loaded Jerusalem cross 124
8.21 Normalized J_x on a Jerusalem cross at 8 GHz 124

8.22 Normalized J_y on a Jerusalem cross at 8 GHz 124
8.23 Normalized J on a Jerusalem cross at 8 GHz 124
8.24 Scattering patterns of a free standing 4 by 4 array of Jerusalem crosses . . 125
8.25 Normalized J on 4 by 4 elemet FSS at 6 GHz 126
8.26 Normalized J on 4 by 4 elemet FSS at 8 GHz 127
8.27 Normalized J on 4 by 4 elemet FSS at 10 GHz 128
8.28 Scattering patterns of a free standing 8 by 8 array of Jerusalem crosses . . 129
8.29 Normalized J on 8 by 8 elemet FSS at 8 GHz 129
8.30 Reflection coefficient of an infinite structure of Jerusalem crosses 130

List of Tables

6.1 Properties of 1D DFT 81
6.2 Properties of 2D DFT 81

To My Family

Abstract

Keywords : *Conjugate gradient fast Fourier transform (CG-FFT), Discrete complex image method (DCIM), Electric field integral equation (EFIE), Frequency selective surfaces (FSS), Generalized pencil-of-functions (GPOF), Green's function (GF), Method of moments (MoM), Prony's method (PM), Sommerfeld integral (SI), Two-dimensional generalized exponential integral (2D-GEI)*

As the need for more frequency spectrum drives the design of antennas and other microwave components at higher frequencies, compact but electrically large microwave components are beginning to appear. Since a significant share of these components comprises scatterers etched on planar stratified layers, efficient tools analyzing and optimizing such structures are invaluable. The work carried out here is in fact a continuation of the research performed in the past at the *Department of Electronics and Telecommunications* at the *Norwegian University of Science and Technology* in Trondheim, Norway.

The conventional method of moments for analyzing and optimizing scatterers in stratified media is simple in formulation but computationally very intensive. Moreover, the computer memory usage of the software based on conventional MoM is high. Both these factors have so far limited the application of conventional MoM to electrically small and simpler stratified structures. Therefore, the present work focuses on introducing and implementing an improved space domain MoM for large radiating or scattering structures etched on planar stratified media. The space domain method of moments is selected due to its simplicity and potential for further improvements when compared with the spectral domain method of moments.

The major areas of space domain MoM such as finding spectral Green's functions, deriving spatial Green's functions, matrix formulation and matrix inversion are addressed. The existing methods are evaluated with respect to their pros and cons. In addition, in order to extract the scattering parameters a few simple de-embedding techniques are introduced. We have attempted to optimize each stage of the conventional space domain MoM such that it can handle electrically large scatterers in planar stratified media. Each method is discussed independently and proved to be performing well compared with the corresponding method applied in conventional space domain MoM. In deriving spectral Green's functions, a novel formulation of transmission line theory is applied easing the analytical derivation and the software implementation significantly. A robust form of discrete complex image method (DCIM) is used in deriving spatial Green's functions from the corresponding spectral Green's functions. DCIM is an accurate and efficient way of evaluating Sommerfeld integrals without resorting to multi-dimensional numerical integration. The accuracy and efficiency of DCIM are affirmed by applying it to simple scatterers. The outcome of DCIM is a sum of complex exponential functions. These are then used to calculate the impedance matrices of MoM. It is also shown that when using mixed potential integral formulation, the original four-dimensional numerical integration can be simplified to two-dimensional integration with no loss of accuracy, thus reducing the mathematical complexity during matrix filling phase. Nevertheless, some of the complex exponential functions can lead to two-dimensional singular integrals. These singular two-dimensional generalized exponential integrals(2D-GEI) are efficiently handled by generalizing an innovative numerical integration method, thus saving the processing time further. The last but most important operation of MoM, the matrix inversion is achieved by using an iterative algorithm known as conjugate gradient method. It is then combined with fast Fourier transform to exploit the space invariant property present in the impedance matrices of MoM. A new compact formulation of the matrices is also presented to facilitate the programing task. To our knowledge, this is the first time such formulation is presented explicitly. A brief chapter is reserved for de-embedding of scattering parameters from the surface current densities resulting from MoM.

In order to present the thesis as a collection of self-containing and independent chapters, results are included in each chapter whenever it is appropriate. These partial results confirm the accuracy and the efficiency of each method introduced in the corresponding chapter before we move on to the next.

The conclusion on the overall method introduced in this work is that the space domain method of moments combined with the discrete complex image method and the conjugate gradient fast Fourier transform presents a very powerful tool for analyzing and optimizing large arbitrary stratified structures. However, to be competitive with commercial products based on either spectral domain method of moments or finite element methods, further improvements in its implementation and methodology are needed. Few improvements such as more efficient implementation of the entire method, inclusion of surface wave contribution in DCIM, integration of non-uniform basis and testing functions and need for better de-embedding techniques are already identified at the end of this work.

Finally we hope that this work clarifies some important issues relating to space domain method of moments when applied to large scatterers etched on planar stratified media and encourages the further research on this particular method.

Preface

This dissertation is submitted in partial fulfillment of the requirements for the degree of *doktor ingeniør* at the *Norwegian University of Science and Technology* (*NTNU*).

The major part of the theoretical studies and the programming presented here were carried out during the time period from 1996 to 2001. The first two years of my research were partly spent on compulsory courses, which laid a solid foundation for this dissertation. In addition, I spent one year working as a teaching assistant at the *Radio Systems Group*, *Department of Electronics and Telecommunications* at *NTNU*. The studies and the research were entirely performed at the *Radio Systems Group*. However, most of the writing was done during the late hours, weekends and holidays while I was working as a research engineer at *SINTEF Information and Communication Technology*, which is a research organization affiliated with *NTNU*.

This work was funded by internal scholarship offered by the *Department of Electronics and Telecommunications* at *NTNU*. In return I was obligated to work there as a teaching assistant.

During the past few years, the important results and achievements of this dissertation were reported in five different conference papers where I received constructive criticism as well as encouraging comments. I hope that anyone who has a comment on this dissertation will contact me even in the future.

Acknowledgments

First of all, I would like to thank my advisor Jon Anders Aas for his guidance, patience and helpfulness during the course of this endeavour. Without his wisdom, encouragements and help, this thesis would have never been a reality.

I am indebted to the *Radio Systems Group*, *Department of Electronics and Telecommunications* at *NTNU* for financially supporting this study during the first four years. My thanks also go to my current employer, *SINTEF Information and Communication Technology* for offering me a livelihood during the last phase of the writing, which seemed to be never-ending.

In addition, I would like to thank all my colleagues at *Radio Systems Group* and *SINTEF Information and Communication Technology* for continuously encouraging me to achieve this final goal. I still wonder without their motivation, moral support and inspiration whether I had dared to continue this work. In particular, I am deeply grateful to our secretary, Kari Berit Øien, for lending a helping hand with all the non-technical issues concerning this dissertation.

I am very thankful to Juan R. Mosig for his brief but valuable comments. They really managed to eliminate the last speck of doubt I had in the success of this attempt. The email communiqué I had with Ismo V. Lindell and N. Hojjat about the discrete complex image method have been the most interesting and enlightening. I am obliged to both of them. Without their help, I would hardly be able to apply this novel, but complicated method in my work.

A special thank goes to Torbjørn Hallgren for making my stay in Norway more pleasant and for helping me with all sorts of bureaucracy whenever it came in my way. I expressed my gratitude to Knut Vidar Skjersli for sacrificing his valuable time and his effort to help me with all sorts of time-consuming undertakings I happened to involve myself in during the last mile of this dissertation. I thank Narada Dilip Warakagoda for being my mentor and for helping me out of all sorts of difficulties I encountered in my word processor. I dearly appreciate the help I got from Lalith Attanapola with my home-pc, whenever it ran amok.

At last, but not least, this dissertation would never have been ended unless I was continuously pushed by the following three parties: My parents, who always started and ended our weekly telephone conversations with asking about my progress. My sister who motivated me to start this hard venture and go through it for so long time. I want to remind her that if I have accomplished something during this time period, she has definitely been a part of it. After all, it was my loving wife who constantly reminded me of the time and drove me to sacrifice even our leisure time for this great cause. I know that I will never be able to make it up to her for that lost time together.

I am also very grateful to my younger brothers Nihal, Nishantha and Keerthi for taking care of my parents during the past few years, thus letting me concentrate on this work. Finally, I convey my gratitude to all the friends whom I was privileged to keep company with during the past decade or so. They always manage to refill me with new energy when I needed it most.

Nomenclature

Coordinate systems

(x, y, z) - Cartesian coordinates

(ρ, ϕ, z) - Cylindrical coordinates

(r, ϕ, θ) - Spherical coordinates

Constants

π - Mathematical constant $\simeq 3.14159265358979$

μ_0 - Permeability of free space $= 4\pi \cdot 10^{-7} (H\, m^{-1})$;

ϵ_0 - Permittivity of free space $= 8.854 \cdot 10^{-12} \simeq \frac{1}{36\pi} \cdot 10^{-9} (F\, m^{-1})$;

Quantities

ω - Angular frequency

λ - Wavelength

$\mathbf{k}$ - Vector wave number

k - Scalar wave number

$\mathbf{E}$ - Electric field intensity

$\mathbf{H}$ - Magnetic field intensity

$\mathbf{D}$ - Electric flux density

$\mathbf{B}$ - Magnetic flux density

$\mathbf{J}_i$ - Impressed (source) electric current density

$\mathbf{J}_c$ - Conduction electric current density

$\mathbf{J}_d$ - Displacement electric current density

$\mathbf{J}_{ic} = \mathbf{J}_i + \mathbf{J}_c$

$\mathbf{M}_i$ - Impressed (source) magnetic current density

$\mathbf{M}_d$ - Displacement magnetic current density

q_{ev} - Electric volume charge density

q_{mv} - Magnetic volume charge density

$\mathbf{A}$ - Magnetic vector potential

$\mathbf{F}$ - Electric vector potential

V - Scalar potential

Notations

$\bar{x}$ - Dyadic x

$\mathbf{x}$ - Vector x

$\hat{x}$ - Unit vector x

$\tilde{x}$ - Spectral domain variable of space domain variable x

The time harmonic variation is assumed to be $\exp(j\omega t)$ where j, ω and t represent $\sqrt{-1}$, angular frequency and time, respectively.

Operations

$\mathbf{x}.\mathbf{y}$ - Dot product of vectors $\mathbf{x}$ and $\mathbf{y}$

$\mathbf{xy}$ - Dyad defined by juxtapositioning the vectors $\mathbf{x}$ and $\mathbf{y}$

$\mathcal{L}$ - Linear operator

$x \otimes y$ - Cross-correlation between x and y

$< x, y >$ - Inner product between x and y

$x * y$ - Linear convolution between x and y

$x \circledcirc y$ - Circular convolution between x and y

$\nabla \bullet \mathbf{x}$ - Divergence of $\mathbf{x}$

$\nabla \times \mathbf{x}$ - Curl of $\mathbf{x}$

$\nabla^2 x = \nabla \bullet \nabla x$ - Laplacian of x

∇x - Gradient of x

Abbreviations and Acronyms

1D - One-Dimensional

2D - Two-Dimensional

2D - GEI - Two-Dimensional Generalized Exponential Integral

CG-FFT - Conjugate Gradient Fast Fourier Transform

CGM - Conjugate Gradient Method

CSWP - Current Standing Wave Pattern

CSWR - Current Standing Wave Ratio

DCIM - Discrete Complex Image Method

EFIE - Electric Field Integral Equation

FFT - Fast Fourier Transform

FSS - Frequency Selective Surfaces

GF - Green's Function

GFC - Green's Function Coefficient

GPOF - Generalized Pencil-Of-Functions

GQ - Gaussian Quadrature

HED - Horizontal Electric Dipole

IE - Integral Equation

LSE - Least Square Estimator

LSI - Linear Space Invariant

LSPM - Least Square Porny's Method

MFIE - Magnetic Field Integral Equation

MoM - Method of Moments

MPIE - Mixed Potential Integral Equation

PBG - Photonic Band Gap

PEC - Perfectly Electric Conductor

PM - Prony's Method

POF - Pencil-Of-Functions

SDP - Steepest Descent Path

SI - Sommerfeld Integral

SIP - Sommerfeld Integration Path

SVD - Singular Value Decomposition

SWR - Standing Wave Ratio

TE - Transverse Electric

TEM - Transverse ElectroMagnetic

TM - Transverse Magnetic

VMD - Vertical Magnetic Dipole

Chapter 1

Introduction

The method of moments (MoM) has been used for analyzing scattering and radiation problems for decades. According to [41], MoM can be interpreted as a method which transforms a continuous operator equation describing the physical problem into a set of matrix equations by first discretizing the operator equation and then performing a inner product on it with selected weighting functions. Many varieties of MoM version have been developed in the past though, they can be broadly divided into two groups, a spectral domain version and a space domain version. Spectral domain MoM relies on evaluating the matrix elements based on spectral domain Green's functions(GFs) whereas the space domain MoM performs the same operation based on space domain GFs.

When analyzing scatterers in planar stratified media, spectral domain MoM has the upper hand due to the existence of spectral GFs in closed form. On the other hand, space domain MoM is frequently based on interpolated or asymptotic spatial GFs. However, recently introduced discrete complex image method [28],[29],[30] has shown to eliminate this barrier faced by space domain MoM by accurately and efficiently approximating the spatial GFs with finite number of complex exponential functions. Nevertheless, corresponding spectral GFs are to be found first. A methodical and programmer-friendly version of determining spectral GFs for planar stratified media was also presented recently in [7]. These two methods finally led to four-dimensional integrals which if not handled carefully, could lead to time consuming numerical integrations. Aiming to reduce these computational complexities, an analytical approach was taken in [47] to reduce the four-dimensional integrals into two-dimensional integrals. The resulting two-dimensional (2D) integrals were referred in [49] and were evaluated efficiently when singularities were present. Moreover, the implicit symmetries among the matrix elements corresponding to an uniform discretization were well known and clearly stated in [48], further relaxing time consuming matrix filling operation in space domain MoM. When applied to large arbitrary scatterers in stratified media, MoM results in a large matrix with poor numerical properties. Inversion of such matrices are efficiently and accurately performed by conjugate gradient fast Fourier transform method [56].

Above methods were mostly presented independently and occasionally cross referred. However, according to our knowledge none in the past had addressed the possible combination of all these techniques for an efficient MoM implementation, which is a must for analyzing large arbitrary scatterers in planar stratified media, for which there is an obvious lack of analytical tools. Therefore this dissertation looks into the ways of accelerating the traditional space domain MoM based on the preceding methods. It involves all major steps in the conventional formulation, such as determining Green's functions, calculating coefficient matrices, solving the resulting matrix equations, etc. For the sake of completeness, a short description on de-embedding techniques is also included. At last, a complete space domain MoM is implemented as a set of MATLAB programs and, sample results are demonstrated for two different cases; a linear patch array and a frequency selective surface. In conclusion, pros and cons of the present MoM are discussed along with the potential improvements.

The original contributions of this work include the introduction of a generalized numerical integration technique that efficiently evaluates singular two-dimensional exponential integrals encountered in space domain MoM and a compact formulation of conjugate gradient fast Fourier transform method appropriate for solving large number of linear equations resulting from space domain MoM for large scatterers in planar stratified media. In addition, minor modifications introduced for a stable implementation of discrete complex image method, the discussion on symmetric properties found in impedance matrices of MoM, and the application of the present method for analyzing finite frequency selective surfaces are also to be in focus.

1.1 Motivation

The motivation behind this thesis is mainly to elaborate the recently developed techniques within space domain MoM. Though the initial idea was to investigate the mutual coupling as a non-ideal effect present in adaptive array implementation, that idea was somewhat generalized and in other ways specialized as the years passed by. Finally, I ended up with implementing an efficient MoM for analyzing large planar structures defined in planar stratified media. Special attention is given to patch antenna arrays and frequency selective surfaces. Here the main idea is to come up with a method which is more efficient than the classical MoM without compromising the accuracy. The present method could be applicable in other areas such as reflectarrays, fractal antennas, PBG (Photonic Band Gap) structures etc.

1.2 Outline

I have tried my best to present each chapter of this thesis as self-contained. Therefore each chapter contains results and partial conclusions dedicated to it. The intention for doing so is to let the reader go through each chapter independent of the rest. Moreover, such independency gave me the opportunity to publish the contents of each chapter with minimum effort. Nevertheless, in order to avoid unnecessary duplication of the texts, the chapters are rarely cross-referred. Major chapters of this dissertation are :

1.2.1 Chapter 2 : Green's functions for stratified media

The basics of the dyadic Green's function for planar stratified media are discussed here. The relationship between space domain and spectral domain Green's functions is stated. The mixed potential integral equation for determining fields, in terms of scalar and vector Green's functions, is then formulated. Moreover, a novel transmission line theory is reviewed as an efficient way of finding spectral vector and scalar Green's functions in stratified media.

1.2.2 Chapter 3 : Discrete complex image method

The recently introduced robust discrete complex image method (DCIM) is reviewed and the difficulties encountered during implementation are addressed. The techniques and tricks used to work around the difficulties are presented. The Prony's method and Generalized Pencil-of-Functions (GPOF) method are revisited briefly. Finally, few spectral domain Green's functions are transformed into space domain applying DCIM. The results are shown to agree well with the numerical values.

1.2.3 Chapter 4 : Method of moments

This core chapter is devoted to the principles of the space domain method of moments used in analyzing stratified media. The criteria for selecting basis and testing functions and the symmetries existing in coefficient matrices are addressed here. This chapter is the backbone of this dissertation whereas the other chapters are more or less concerned with the ways of optimizing the space domain MoM.

1.2.4 Chapter 5 : Numerical evaluations in MoM

At the beginning, this chapter introduces the numerical integration techniques applied in evaluating Sommerfeld type integrals and the problems faced during their practical implementation. A specific method suitable for evaluating singular two-dimensional exponential integrals is then introduced and generalized. Its efficiency and accuracy are affirmed based on simulation results.

1.2.5 Chapter 6 : CG-FFT

This chapter describes the application of the conjugate gradient method (CGM) for solving the equation system derived by the space domain MoM. The fast Fourier transformation (FFT) is associated with CGM for speeding up the matrix multiplications, thus the name *'conjugate gradient fast Fourier transform method' (CG-FFT).* Its performance is then assessed in terms of accuracy and efficiency.

1.2.6 Chapter 7 : De-embedding techniques

This brief chapter outlines several methods of extracting S parameters based on the current densities induced on striplines. It merely presents the mathematical background for de-embedding. The de-embedding method applied here for extracting S parameters is then verified using simple examples.

1.2.7 Chapter 8 : Results

This chapter presents a few illustrative results in analyzing practical patch antenna structures. The simulated results are also compared with measured results. This chapter tests the software developed here for its accuracy and efficiency. More examples dealing with frequency selective surfaces are also included in order to demonstrate the versatility of the developed method.

1.2.8 Chapter 9 : Discussion and conclusions

This chapter includes the conclusive remarks on the present methodology and the simulation software developed. The accomplishments and the limitations are mentioned. Potentials for further improvements are also discussed.

Chapter 2

Green's Functions for Stratified Media

2.1 Introduction

In the area of electromagnetism, solutions to many problems are obtained starting from an uncoupled partial differential equation derived from Maxwell's equations and the appropriate boundary conditions. The use of Green's function offers an easy way of representing most of these solutions in a rather compact form. With the Green's function technique, a solution to the partial differential equation is first obtained by considering a unit source (i.e. impulse or a Dirac delta) as the driving function and by satisfying the imposed boundary conditions. This solution, which is the impulse response of the given system, is also known as the Green's function of that system. The solution to the actual driving function, which is often much more complex than a unit source, is then obtained by the superposition of the impulse response with varying location of the unit source. This summation can ultimately be expressed as an integral. The major advantage of the Green's function technique is that when the necessary Green's functions are derived for a given set of boundary conditions for a particular problem, solving the same problem for a different source constrained to the same boundary conditions is simple and straightforward.

Let us formulate these relationships mathematically. Given the linear differential equation of the form

$$\mathcal{L}\, y = f \tag{2.1}$$

where

$\mathcal{L}$ denotes a linear differential operator in one dimension,

y is a scalar response function and

f is a scalar source function.

If the Green's function G for this particular system exists, the solution for y can be expressed as

$$y = \int_S G \, df \tag{2.2}$$

where S is the domain of the source function f.

2.2 Dyadic Green's Function

Most electromagnetic problems are vectorial in nature. Therefore, the need for extending the above one-dimensional scalar Green's function to multi-dimensional vectors emerges. Vectors and dyadics are often used to describe linear transformations within a given orthogonal system and to simplify the mathematical manipulations.

Let us write the linear vector problem that generalizes the scalar version (2.1) as

$$\mathcal{L}\, \mathbf{h}(\mathbf{r}) = \mathbf{f}(\mathbf{r}') \tag{2.3}$$

where

$\mathcal{L}$ is a vector differential operator,

$\mathbf{h}(\mathbf{r})$ is a vector field function,

$\mathbf{f}(\mathbf{r}')$ is a vector source function and

$\mathbf{r}$ and $\mathbf{r}'$ are position vectors of the field- and source-point, respectively.

However, the solution of (2.3) can not in general be written following the scalar solution (2.2) since the relation

$$\mathbf{h}(\mathbf{r}) = \iiint_V \mathbf{f}(\mathbf{r}')\, G(\mathbf{r}, \mathbf{r}')\, dv' \tag{2.4}$$

with G as a scalar Green's function would imply that a component of the source $\mathbf{f}(\mathbf{r}')$ parallel to a given axis produces a field parallel to the same axis, which is not generally true. On the other hand, a general solution, for example in rectangular coordinate system, can be written by expressing each component along the x, y and z direction in the same form as (2.4).

$$\mathbf{h}(\mathbf{r}) = \iiint_V [f_x(\mathbf{r}')\mathbf{G}_x(\mathbf{r}, \mathbf{r}') + f_y(\mathbf{r}')\mathbf{G}_y(\mathbf{r}, \mathbf{r}') + f_z(\mathbf{r}')\mathbf{G}_z(\mathbf{r}, \mathbf{r}')]\, dv' \tag{2.5}$$

$$\begin{array}{rclclcl}
\mathbf{G}_x(\mathbf{r}, \mathbf{r}') & = & \hat{x}\, G_{xx}(\mathbf{r}, \mathbf{r}') & + & \hat{y}\, G_{yx}(\mathbf{r}, \mathbf{r}') & + & \hat{z}\, G_{zx}(\mathbf{r}, \mathbf{r}') \\
\mathbf{G}_y(\mathbf{r}, \mathbf{r}') & = & \hat{x}\, G_{xy}(\mathbf{r}, \mathbf{r}') & + & \hat{y}\, G_{yy}(\mathbf{r}, \mathbf{r}') & + & \hat{z}\, G_{zy}(\mathbf{r}, \mathbf{r}') \\
\mathbf{G}_z(\mathbf{r}, \mathbf{r}') & = & \hat{x}\, G_{xz}(\mathbf{r}, \mathbf{r}') & + & \hat{y}\, G_{yz}(\mathbf{r}, \mathbf{r}') & + & \hat{z}\, G_{zz}(\mathbf{r}, \mathbf{r}')
\end{array} \tag{2.6}$$

Note that $\mathbf{G}_x(\mathbf{r},\mathbf{r}')$, $\mathbf{G}_y(\mathbf{r},\mathbf{r}')$ and $\mathbf{G}_z(\mathbf{r},\mathbf{r}')$ in this representation are vector Green's functions. More compact representation of (2.5) can be given as

$$\mathbf{h}(\mathbf{r}) = \iiint\limits_V \mathbf{f}\,(\mathbf{r}') \cdot \bar{G}(\mathbf{r},\mathbf{r}')\; dv' \tag{2.7}$$

The notation $\cdot$ denotes the dot product and $\bar{G}$ is the dyadic Green's function, which can be expressed as

$$\bar{G}(\mathbf{r},\mathbf{r}') = \hat{x}\;\mathbf{G}_x(\mathbf{r},\mathbf{r}') + \hat{y}\;\mathbf{G}_y(\mathbf{r},\mathbf{r}') + \hat{z}\;\mathbf{G}_z(\mathbf{r},\mathbf{r}') \tag{2.8}$$

Here **ab** defines a dyad by juxtapositioning the vectors **a** and **b**. In matrix form, a dyad can be represented as follows [2]

$$\mathbf{ab} = (\langle a_1, a_2, a_3\rangle\,\langle b_1, b_2, b_3\rangle) = \begin{bmatrix} a_1b_1 & a_1b_2 & a_1b_3 \\ a_2b_1 & a_2b_2 & a_2b_3 \\ a_3b_1 & a_3b_2 & a_3b_3 \end{bmatrix} \tag{2.9}$$

Accordingly, (2.7) can be written in the following matrix form

$$\begin{bmatrix} h_x & h_y & h_z \end{bmatrix} = \iiint_V \begin{bmatrix} f_x & f_y & f_z \end{bmatrix} \begin{bmatrix} G_{xx} & G_{yx} & G_{zx} \\ G_{xy} & G_{yy} & G_{zy} \\ G_{xz} & G_{yz} & G_{zz} \end{bmatrix} dv' \tag{2.10}$$

The dyadic Green's function $\bar{G}(\mathbf{r},\mathbf{r}')$ can be found by first solving the following individual homogeneous differential equations (2.11). They resemble (2.3) and satisfy the specified boundary conditions. Their individual solutions are then used to build up the more general dyadic Green's function by combining them according to (2.8).

$$\begin{aligned} \mathcal{L}\;\mathbf{G}_x(\mathbf{r},\mathbf{r}') &= \hat{x}\;\delta(\mathbf{r}-\mathbf{r}') \\ \mathcal{L}\;\mathbf{G}_y(\mathbf{r},\mathbf{r}') &= \hat{y}\;\delta(\mathbf{r}-\mathbf{r}') \\ \mathcal{L}\;\mathbf{G}_z(\mathbf{r},\mathbf{r}') &= \hat{z}\;\delta(\mathbf{r}-\mathbf{r}') \end{aligned} \tag{2.11}$$

2.3 Spectral Green's Functions vs Spatial Green's Functions

In the previous section Green's functions are introduced solely based on spatial coordinates $\mathbf{r}$ and $\mathbf{r}'$ and hence is commonly known as the spatial Green's functions or space-domain Green's functions. They are more intuitive when compared to their spectral counterparts, the spectral Green's functions. In electromagnetic field propagation terminology, a spatial Green's function simply describes the propagation of fields produced by a point source as a function of space coordinates, whereas the corresponding spectral Green's function expresses the field propagation in another conveniently selected spectral domain. The propagation constant vector is often selected as the spectral variable. Let us further elaborate on the exact relationship between these two domains.

2.3.1 Two-dimensional Fourier transformation

The two-dimensional (2D) Fourier transformation and 2D inverse Fourier transformations are defined respectively by

$$\Psi(\varsigma_1, \varsigma_2) = \frac{1}{4\pi^2} \int_{-\infty}^{+\infty} \int_{-\infty}^{+\infty} \psi(\xi_{1,}\xi_2) e^{-j(\varsigma_1 \xi_1 + \varsigma_2 \xi_2)}\, d\xi_1\, d\xi_2 \tag{2.12}$$

$$\psi(\xi_{1,}\xi_2) = \int_{-\infty}^{+\infty} \int_{-\infty}^{+\infty} \Psi(\varsigma_1, \varsigma_2) e^{j(\xi_1 \varsigma_1 + \xi_2 \varsigma_2)}\, d\varsigma_1\, d\varsigma_2 \tag{2.13}$$

Here $\Psi(\varsigma_1, \varsigma_2)$ is called the Fourier transformation of the function $\psi(\xi_{1,}\xi_2)$. The variables ς_1 and ς_2 represent the Fourier (or spectral) domain whereas ξ_1 and ξ_2 represent the corresponding variables in the spatial domain. Although the functions Ψ and ψ given in (2.12) and (2.13) are scaler functions, these relationships can readily be generalized to vector quantities by applying these scalar transformations to each component of the vector [3].

If the Green's dyadic $\bar{G}(\mathbf{r}, \mathbf{r}')$ in (2.7) is translational-invariant, i.e. $\bar{G}(\mathbf{r}, \mathbf{r}')$ depends solely on the difference $(\mathbf{r} - \mathbf{r}')$ rather than the separate values of $\mathbf{r}$ and $\mathbf{r}'$, $\mathbf{h}(\mathbf{r})$ in (2.7) can be written as a convolution between $\mathbf{f}\,(\mathbf{r})$ and $\bar{G}(\mathbf{r})$ in 3D space.

$$\mathbf{h}(\mathbf{r}) = \iiint_V \mathbf{f}\,(\mathbf{r}') \cdot \bar{G}(\mathbf{r} - \mathbf{r}')\, dv' \tag{2.14}$$

Assuming a rectangular coordinate system, the application of 2D Fourier transformation (2.12) to (2.14) leads to [3]

$$H(\mathbf{k}, z) = \int_{z'} F(\mathbf{k}, z') \cdot \bar{\mathcal{G}}(\mathbf{k}, z - z')\, dz' \tag{2.15}$$

Here $\mathbf{k}$ is the 2D spectral domain variable given as $\mathbf{k} = \hat{x}\, k_x + \hat{y}\ k_y$. $\bar{\mathcal{G}}(\mathbf{k}, z')$ denotes spectral dyadic Green's function. $H(\mathbf{k}, z)$ and $F(\mathbf{k}, z')$ denote 2D Fourier transform of $\mathbf{h}(\mathbf{r})$ and $\mathbf{f}\,(\mathbf{r}')$ respectively. When (2.15) applies to a stratified medium that is parallel to the xy plane and a source parallel to the xy plane, it can be simplified to the following form [3]

$$H(\mathbf{k},z) = F(\mathbf{k}, z').\bar{\mathcal{G}}(\mathbf{k}, z - z') \tag{2.16}$$

Therefore, based on the above Fourier transformation pair, (2.12) and (2.13), and the Maxwell's equations (presented in section 2.4.1) the propagation of electric and magnetic fields in a given medium can be described in both space- and spectral domain. Since both formulations lead to an identical solution, it is advantageous to formulate the problem in hand using the most convenient domain. Which domain to be used depends entirely on the nature of the problem and the complexity of the boundary conditions.

2.4 Mixed Potential Integral Equation

2.4.1 Maxwell's equations

The variations of electric and magnetic fields, charges and current associated with electromagnetic waves are governed by physical laws known as Maxwell's equations. They were first introduced by James Clark Maxwell based on empirical results and mathematical reasoning. They can briefly be expressed in their differential form [2] when applied to time-harmonic field quantities

$$\nabla \times \mathbf{E} = -\mathbf{M}_i - j\omega\mathbf{B} \tag{2.17}$$

$$\nabla \times \mathbf{H} = \mathbf{J}_i + \mathbf{J}_c + j\omega\mathbf{D} = \mathbf{J}_{ic} + j\omega\mathbf{D} = \mathbf{J}_{ic} + \mathbf{J}_d \tag{2.18}$$

$$\nabla \cdot \mathbf{D} = q_{ev} \tag{2.19}$$

$$\nabla \cdot \mathbf{B} = q_{mv} \tag{2.20}$$

where

$\mathbf{E}$ electric field intensity (V/m),

$\mathbf{H}$ magnetic field intensity (A/m),

$\mathbf{D}$ electric flux density (C/m^2),

$\mathbf{B}$ magnetic flux density (Wb/m^2),

$\mathbf{J}_i$ impressed (source) electric current density (A/m^2),

$\mathbf{J}_c$ conduction electric current density (A/m^2),

$\mathbf{J}_d$ displacement electric current density (A/m^2),

$\mathbf{J}_{ic} = \mathbf{J}_i + \mathbf{J}_c$,

$\mathbf{M}_i$ impressed (source) magnetic current density (V/m^2),

$\mathbf{M}_d$ displacement magnetic current density (V/m^2),

q_{ev} electric volume charge density (C/m^3) and

q_{mv} magnetic volume charge density (Wb/m^3).

It is implied that all the field quantities above exhibit both space and time dependency. Throughout this thesis, the time harmonic variation is assumed to be $\exp(j\omega t)$ where j, ω and t represent $\sqrt{-1}$, angular frequency and time, respectively.

2.4.2 Continuity equation

In addition to the above Maxwell's equations, there is another equation, yet not an independent relation, that expresses dependence between variations of the electric current density $\mathbf{J}_{ic}$ and the electric charge density q_{ev}.

$$\nabla \cdot \mathbf{J}_{ic} = -j\omega q_{ev} \tag{2.21}$$

Likewise, the magnetic current density $\mathbf{M}_i$ and the magnetic charge density q_{mv} are governed by :

$$\nabla \cdot \mathbf{M}_i = -j\omega q_{mv} \tag{2.22}$$

2.4.3 Potentials

It is obvious that one can characterize the electromagnetic propagation completely in three dimensional space using the six time-dependent components of electric and magnetic fields. For example, in rectangular coordinate system, they can be chosen as three electric field components E_x, E_y and E_z, and three magnetic field components H_x, H_y and H_z. These scalar components are not independent, but are linked by Maxwell's equations (2.17) - (2.20). It is shown in [4] that in a source-free region, as few as two independent quantities, suffice to determine the fields entirely. These quantities are often called the potentials. For a stratified medium parallel to the xy-plane, E_z and H_z are often selected as these two potentials. This is perhaps the most straightforward and apparently the simplest choice, since it avoids the introduction of any new quantities. However, for a planar stratified medium, spatial Green's functions associated with these two quantities possess the singularities of order three, i.e. $O(|\mathbf{r} - \mathbf{r}'|^{-3})$. This is an obvious disadvantage in applying integral equation techniques because such singularities make the numerical integration algorithm very unstable unless they are handled with caution. This calls for an introduction of other more convenient quantities.

Vector potentials A and F

In source-free space, both the magnetic flux density $\mathbf{B}$ and the electric flux density $\mathbf{D}$ are solenoidal, that is $\nabla \cdot \mathbf{B} = 0$ and $\nabla \cdot \mathbf{D} = 0$ respectively. Therefore it is possible to introduce two vector potentials $\mathbf{A}$ and $\mathbf{F}$, which satisfy the Helmholtz equations [2]

$$(\nabla^2 + k^2)\mathbf{A} = -\mu \mathbf{J} \tag{2.23}$$

$$(\nabla^2 + k^2)\mathbf{F} = -\varepsilon \mathbf{M} \tag{2.24}$$

$\mathbf{A}$ and $\mathbf{F}$ are called magnetic vector potential and electric vector potential, respectively. $k = \omega\sqrt{\mu\varepsilon}$ and ∇^2 denotes the Laplacian operator. Consequently, the field components can be expressed as [2]

$$j\omega\mu\varepsilon\,\mathbf{E} = k^2\mathbf{A} + \nabla(\nabla \cdot \mathbf{A}) - j\omega\mu\,\nabla \times \mathbf{F} \tag{2.25}$$

$$j\omega\mu\varepsilon\,\mathbf{H} = k^2\mathbf{F} + \nabla(\nabla \cdot \mathbf{F}) + j\omega\varepsilon\,\nabla \times \mathbf{A} \tag{2.26}$$

Scalar potential V

In addition, another quantity known as the scalar potential V is defined. It is related to magnetic vector potential $\mathbf{A}$ by the Lorentz's gauge [5]

$$j\omega\mu\varepsilon V + \nabla \cdot \mathbf{A} = \mathbf{0} \tag{2.27}$$

Therefore in the absence of an electric vector potential **F,** (2.25) can be written as

$$\mathbf{E} = -j\omega\mathbf{A} - \nabla V \tag{2.28}$$

2.4.4 Integral equation method

The objective of the integral equation (IE) method is to set up an integral equation, where the unknown induced current density on the surface of a scatterer is a part of the integrand. Then, the technique known as the method of moments (MoM) is often used to solve this equation for the unknown current density.

There are many forms of integral equations. Two of the most popular for time-harmonic electromagnetic problems are the electric field integral equation (EFIE) and the magnetic field integral equation (MFIE). The EFIE enforces the boundary condition on the tangential electric field whereas the MFIE enforces the boundary condition on the tangential magnetic field. Since the field propagation in stratified media is best handled by EFIE, we shall only elaborate on it.

2.4.5 Electric field integral equation

The electric field integral equation (EFIE) is based on the boundary condition that the total tangential electric field on a perfectly electric conducting (PEC) surface is zero. This can be expressed as

$$\begin{array}{lclcll} E_t^{total} & = & E_t^i + E_t^s & = & 0 & on\ S \\ E_t^i & = & -E_t^s & & & on\ S \end{array} \tag{2.29}$$

where

S represents the PEC surface,

subscript t denotes the tangential fields and

superscripts $total$, i and s indicate the total fields, the incident fields and the scattered fields, respectively.

Depending on the context, incident fields E_t^i can either be a wave incident on an antenna (receiving mode) or a wave explicitly fed to an antenna (transmitting mode). The scattered field E_t^s is generated by the current induced on the PEC surface of the antenna.

2.4.6 Mixed potential formulation

Although equation (2.28) expresses the electric field in terms of **A** and V potentials, it does not present any practical convenience since the same degree of singularity, i.e. $O(|\mathbf{r}-\mathbf{r}'|^{-3})$, still exists in the electric field components. A different formulation introduced in [6] removes some of these higher order singularities, however. Accordingly, for a PEC submerged in a stratified medium, **A** and V in (2.28) can be expressed in the equivalent forms as follows.

$$\mathbf{A}(\mathbf{r}) = \int_S \bar{G}_{\mathbf{A}}(\mathbf{r},\mathbf{r}')\ \mathbf{J}(\mathbf{r}')\ ds' \tag{2.30}$$

$$V = \int_S G_q(\mathbf{r},\mathbf{r}')\ q(\mathbf{r}')\ ds' \tag{2.31}$$

Here,

$$\mathbf{J}(\mathbf{r}') = J_x(\mathbf{r}')\ \hat{x} + J_y(\mathbf{r}')\ \hat{y} + J_z(\mathbf{r}')\ \hat{z} \tag{2.32}$$

$\bar{G}_{\mathbf{A}}(\mathbf{r},\mathbf{r}')$ is the dyadic Green's function for the vector potential **A,**

$G_q(\mathbf{r},\mathbf{r}')$ is the scalar Green's function for the scalar potential V,

$\mathbf{J}(\mathbf{r}')$ is the surface current density,

$q(\mathbf{r}')$ is the surface charge density and

S refers to the PEC surface of the scatterer.

Substituting (2.30) and (2.31) in (2.28) and applying the continuity equation (2.21), lead to

$$\mathbf{E}(\mathbf{r}) = -j\omega \int_S \bar{G}_{\mathbf{A}}(\mathbf{r},\mathbf{r}')\ \mathbf{J}(\mathbf{r}')\ ds' + \frac{\nabla}{j\omega}\int_S G_q(\mathbf{r},\mathbf{r}')\ \nabla\cdot\mathbf{J}(\mathbf{r}')\ ds' \tag{2.33}$$

In the absence of magnetic currents, an electric dipole perpendicular to the dielectric layers is associated with one component of **A** perpendicular to the layers [7]. Meanwhile, a dipole parallel to the dielectric layers needs a perpendicular component and a parallel component to the dielectric layers [7]. Hence, if we assume a stratified medium parallel to the xy plane, $\bar{G}_{\mathbf{A}}(\mathbf{r},\mathbf{r}')$ can be expressed in matrix form.

$$\bar{G}_{\mathbf{A}}(\mathbf{r},\mathbf{r}') = \begin{bmatrix} G^A_{xx}(\mathbf{r},\mathbf{r}') & 0 & 0 \\ 0 & G^A_{yy}(\mathbf{r},\mathbf{r}') & 0 \\ G^A_{zx}(\mathbf{r},\mathbf{r}') & G^A_{zy}(\mathbf{r},\mathbf{r}') & G^A_{zz}(\mathbf{r},\mathbf{r}') \end{bmatrix} \tag{2.34}$$

If the PEC surface S is a planar structure parallel to the xy plane, $J_z(\mathbf{r}') = 0$ and the corresponding Green's function components G^A_{zx}, G^A_{zy} and G^A_{zz} are no longer interesting. Thus the components $E_x(\mathbf{r})$ and $E_y(\mathbf{r})$ of $\mathbf{E}(\mathbf{r})$ can be written as

$$E_x(\mathbf{r}) = -j\omega G^A_{xx}(\mathbf{r}, \mathbf{r}') * J_x + \frac{1}{j\omega}\frac{\partial}{\partial x}(G_q(\mathbf{r}, \mathbf{r}') * \nabla \cdot \mathbf{J}(\mathbf{r}')) \tag{2.35}$$

$$E_y(\mathbf{r}) = -j\omega G^A_{yy}(\mathbf{r}, \mathbf{r}') * J_y + \frac{1}{j\omega}\frac{\partial}{\partial y}(G_q(\mathbf{r}, \mathbf{r}') * \nabla \cdot \mathbf{J}(\mathbf{r}')) \tag{2.36}$$

where $*$ denotes the convolution operation

$$A * B = \int\limits_S A(\mathbf{r}, \mathbf{r}')B(\mathbf{r}')\, ds' \tag{2.37}$$

In rectangular coordinate system, this representation can be expanded to

$$A * B = \iint\limits_S A(x - x', y - y', z, z')B(x', y', z')\, dx'dy' \tag{2.38}$$

Now, it is apparent that the operation $*$ denotes the well-known form of 2D convolution with respect to the x and y coordinates. In brief, the equations (2.35) and (2.36) express the electric field components E_x and E_y in terms of vector and scalar Green's functions and the induced current density. This formulation is thus known as the mixed potential formulation. The Green's functions associated with these two potentials posses singularity of order one, $O(|\mathbf{r} - \mathbf{r}'|^{-1})$. They are therefore better suited for numerical computation than the Green's functions having singularities of third order, $O(|\mathbf{r} - \mathbf{r}'|^{-3})$ [8]. For example in a homogeneous medium, the magnetic vector potential produced by an electric current element is parallel to it [9], i.e.

$$\mathbf{A} = A_a \hat{a}$$

and

$$G^A_a = \frac{\mu}{4\pi}\frac{\exp(-jkr)}{r} \tag{2.39}$$

where

a denotes either x or y direction,

μ is the permeability in homogeneous space and

r is the distance between the source point and the field point.

Likewise, the scalar potential produced by an elementary charge in homogeneous medium can be written as

$$G_q = \frac{\mu}{4\pi j\omega\epsilon}\frac{\exp(-jkr)}{r} \tag{2.40}$$

Here ϵ is the permittivity in homogeneous space

2.5 Field Propagation in Stratified Media

Although the spectral Green's functions for a stratified medium are possible to determine exactly in closed forms, the spatial Green's functions are not. Therefore, in general the spatial Green's functions are calculated point-wise, starting from the corresponding spectral Green's functions and applying the inverse 2D Fourier transformation (2.13). This numerical transformation is time consuming and memory intensive due to the numerical evaluation of 2D integrals. In some literature, a compromise between the accuracy and the computer resources has been made using some carefully selected interpolation method. In such methods, the interpolation is performed based on a few prior determined spatial Green's function values. Hence, the software based on such methods presumes that the selected interpolation method would perform equally well for every stratified structure with no intervene by the user. In chapter 3, we shall take a different approach when determining the spatial Green's functions from the corresponding spectral Green's functions. In order to evaluate the accuracy of this approximated Green's functions calculated there, the spatial Green's functions are first evaluated precisely applying the inverse Fourier transformation to the corresponding spectral Green's functions. This is done point-wise at the cost of time and computer resources. Nevertheless, in order to keep the calculation time reasonably low a few efficient techniques have been applied.

2.6 Unified Transmission Line Theory for Spectral Green's Functions

The derivation of spectral Green's functions of multilayer media is analytical but tedious, giving rise to many lengthy expressions of the spectral function for various combinations of source and field locations in the multilayers. Hence this operation is considered as programmer-time intensive. An effective, uniform and methodical technique introduced in [7] is followed here to determine the spectral Green's functions of a planar stratified medium. It eases the analytical derivation and the software implementation of Green's functions of a stratified medium significantly.

When a general multilayer medium containing both magnetic and electric sources is located in the rectangular coordinate system, there are as many as ten different types of Green's functions associated with three types of potentials [7]. Nevertheless, in this dissertation we are concerned with only the electric surface currents parallel to the dielectric interfaces. Therefore the number of unknown Green's functions are limited to six, i.e. four vector potential Green's functions (e.g. G^A_{xx}, G^A_{zx}, G^A_{yy} and G^A_{zy}) and two scalar potential Green's functions (e.g. G^q_{xx} and G^q_{yy}). Since x and y are orthogonal to each other in practice, the expressions for G^A_{xx}, G^A_{zx} and G^q_{xx} resemble the corresponding expressions for G^A_{yy}, G^A_{zy} and G^q_{yy}. Hence, G^A_{yy}, G^A_{zy} and G^q_{yy} can be derived from G^A_{xx}, G^A_{zx} and G^q_{xx} by a simple coordinate transformation. It effectively reduces the necessary number of elementary Green's functions to three. We shall now employ the above mentioned method to determine these functions. The method basically expresses the wave propagation in each individual layer of the multilayer structure and then exploits the transmission line analogy of the wave propagation in the stratified layers when transformed to the spectral

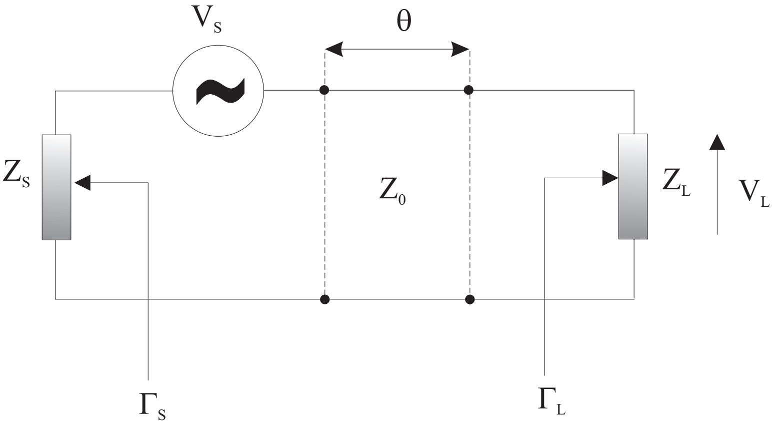

Fig. 2.1: *Simple one section transmission line*

domain. In the sequel, we shall summarize the basic relations used in this formulation.

For a simple one-section transmission line model shown in Fig. 2.1, it can be shown that the voltage transfer function T at the load is given by the following relationships [7]:

$$\begin{aligned} T &= \frac{V_L}{\frac{V_S}{2}} = (1-\Gamma_S)(1+\Gamma_L)\,\frac{e^{-j\theta}}{1-\Gamma_S\Gamma_L e^{-2j\theta}} && (2.41)\\ &= (1-\Gamma_S)(1+\Gamma_L)\,\frac{1}{\begin{bmatrix}1\\-\Gamma_S\end{bmatrix}^T\begin{bmatrix}e^{j\theta} & 0\\ 0 & e^{-j\theta}\end{bmatrix}\begin{bmatrix}1\\ \Gamma_L\end{bmatrix}}\\ &= (1-\Gamma_S)(1+\Gamma_L)\,\frac{1}{\begin{bmatrix}1\\-\Gamma_S\end{bmatrix}^T A\begin{bmatrix}1\\ \Gamma_L\end{bmatrix}}\\ &= (1-\Gamma_S)(1+\Gamma_L)\,\frac{1}{P} && (2.42)\end{aligned}$$

where

V_L denotes the voltage drop over the load Z_L,

V_S denotes the source voltage,

Γ_S denotes the reflection coefficient due to the source impedance Z_S and is defined by

$$\Gamma_S = \frac{Z_S - Z_0}{Z_S + Z_0} \qquad (2.43)$$

Here, Z_0 is the characteristic impedance of the transmission line.

Γ_L denotes the reflection coefficient due to the load Z_L and is defined by

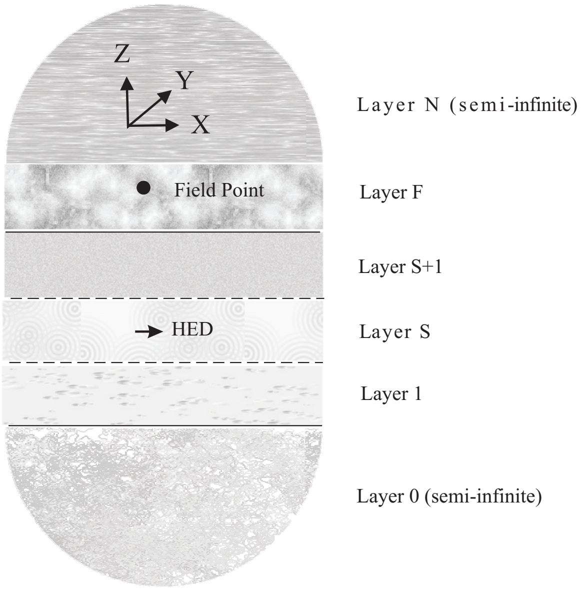

Fig. 2.2: *Stratified medium with an infinitesimal horizontal electric dipole (HED)*

$$\Gamma_L = \frac{Z_L - Z_0}{Z_L + Z_0} \tag{2.44}$$

θ denotes the progress in the phase front along the transmission line.

$$P = \frac{1 - \Gamma_S \Gamma_L e^{-2j\theta}}{e^{-j\theta}} = \left[\begin{array}{c} 1 \\ -\Gamma_S \end{array} \right]^T A \left[\begin{array}{c} 1 \\ \Gamma_L \end{array} \right] \tag{2.45}$$

$$A = \left[\begin{array}{cc} e^{j\theta} & 0 \\ 0 & e^{-j\theta} \end{array} \right] \tag{2.46}$$

A general stratified medium excited by a HED is illustrated in Fig. 2.2. Based on the well-known transmission line analogy of the wave propagation in stratified media in the spectral domain, we can suggest the cascaded transmission line shown in Fig. 2.3 for this structure. Then applying the transfer function (2.41) to each section of this cascaded line and eliminating the common load/source between each adjoint line section, the transfer function V_L for the complete stratified medium can be found [7].

$$\begin{aligned} V_L &= V(Z_F) = \frac{V_S}{2}\, a_S\, (1 - \Gamma_S)(1 + \Gamma_L)\, a_L\, \frac{1}{P} \qquad (2.47) \\ &= \frac{V_S}{2}\, \frac{a_S \left[\begin{array}{cc} 1 & -\Gamma_S \end{array} \right] \left[\begin{array}{cc} 1 & 1 \end{array} \right]^T \left[\begin{array}{cc} 1 & 1 \end{array} \right] \left[\begin{array}{cc} 1 & \Gamma_L \end{array} \right]^T a_L}{P} \end{aligned}$$

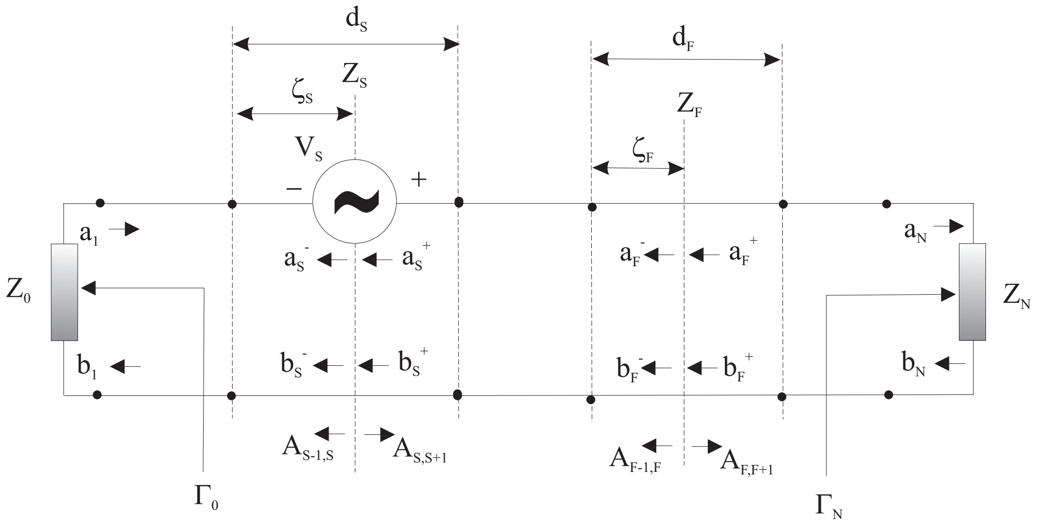

Fig. 2.3: *Cascaded sections of transmission line*

where

$$P = \begin{bmatrix} 1 \\ -\Gamma_0 \end{bmatrix}^T A_1 A_{12}\ A_2 A_{23}\ \ldots\ A_{S-} A_{S+}\ \ldots\ A_{F-} A_{F+}\ \ldots\ A_{(N-1)} A_{(N-1)\ N}\ A_N \begin{bmatrix} 1 \\ \Gamma_N \end{bmatrix} \tag{2.48}$$

$$a_S \begin{bmatrix} 1 & -\Gamma_S \end{bmatrix} = \begin{bmatrix} 1 & -\Gamma_0 \end{bmatrix} A_1 A_{12}\ A_2 A_{23}\ \ldots\ A_{S-} \tag{2.49}$$

$$\begin{bmatrix} 1 & \Gamma_L \end{bmatrix}^T a_L = A_{F+}\ \ldots\ A_{(N-1)} A_{(N-1)\ N}\ A_N \begin{bmatrix} 1 \\ \Gamma_N \end{bmatrix} \tag{2.50}$$

$$A_n = \begin{bmatrix} e^{j\theta_n} & 0 \\ 0 & e^{-j\theta_n} \end{bmatrix} \tag{2.51}$$

with

$\theta_n = k_{zn} d_n$	d_n is the thickness of the n$^{\text{th}}$ layer
$k_{zn}^2 = k_n^2 - k_\rho^2$	k_n is the propagation constant of the n$^{\text{th}}$ medium
$k_\rho^2 = k_x^2 + k_y^2$	k_ρ, k_x and k_y are radial, x- and y-directed spectral-domain variables, respectively

(2.52)

$$A_{n\ (n+1)} = \frac{1}{\gamma_{n\ (n+1)} + 1} \begin{bmatrix} 1 & \gamma_{n\ (n+1)} \\ \gamma_{n\ (n+1)} & 1 \end{bmatrix} \tag{2.53}$$

$$\gamma_{n\ (n+1)} = \frac{Z_{n+1} - Z_n}{Z_{n+1} - Z_n} \tag{2.54}$$

The transmission matrices $A_S^{\pm}$ and $A_F^{\pm}$ are defined as in (2.46) with θ replaced by $\theta_i^+ = k_{zi}(d_i - \zeta_i)$ and $\theta_i^- = k_{zi}\zeta_i$. Here i denotes either S (stands for source) or F (stands for field) points and ζ_i are the distances of source and field points from the immediately left (lower) interface and d_i are the thicknesses of the layers in which the source and field points are located. Moreover, Z_0 and Z_N are the wave impedances of the lower and upper unbounded layers, respectively. Their corresponding reflection coefficients are denoted by Γ_0 and Γ_N and are defined as in Fig. 2.3. As given in (2.46) and (2.53), the evaluation of all submatrices $A_{n\,(n+1)}$ and A_n is rather simple and straightforward. It should also be noted that the denominator P in (2.42) is independent of the source and field locations. This in turn means that the zeros of P, i.e. the surface wave singularities, are not affected by the source and field locations. The independence of P on source and field locations saves the computation time when evaluating the same Green's function for various source and field locations for given multilayer media. In addition, by isolating the dependency of source and field locations (denoted by ζ_i) in only a few matrices, the analytical differentiation of the above expressions with respective to ζ_i, an operation which is often encountered when applying Green's functions for field calculations, becomes very convenient.

Following the definitions given in (2.47) - (2.54), a more general voltage transfer function valid for multilayer media can be expressed as

$$T = \frac{V_L}{\frac{V_S}{2}} = \frac{a_S \begin{bmatrix} 1 & -\Gamma_S \end{bmatrix} \begin{bmatrix} 1 & \Gamma_L \end{bmatrix}^T a_L}{P} \tag{2.55}$$

2.6.1 Electric sources in multilayer media

An electric point source placed at the position vector $\mathbf{r}_S$ and pointing in the direction $\hat{u}$ is often denoted by

$$\mathbf{J} = \delta(\mathbf{r} - \mathbf{r}_S)\, \hat{u} \tag{2.56}$$

where $\delta(\mathbf{r})$ is the Dirac delta function.

If this electric source radiates into an infinite homogenous space, characterized by the permittivity ε_S and permeability μ_S, the corresponding vector potential $\mathbf{A}_S$ is given by [7]

$$\mathbf{A}_S\left(\mathbf{r}, \mathbf{r}_S\right) = \frac{\mu_S}{4\pi} \frac{\exp(-jk_S\left|\mathbf{r} - \mathbf{r}_S\right|)}{\left|\mathbf{r} - \mathbf{r}_S\right|}\, \hat{u} \tag{2.57}$$

where

$k_s^2 = \omega^2 \mu_S \varepsilon_S$ and

$|\mathbf{x}|$ denotes the magnitude of the vector $\mathbf{x}$.

In terms of plane-wave spectrum, (2.57) can also be expressed as [7]

$$\mathbf{A}_S\left(\mathbf{r},\mathbf{r}_S\right) = \hat{u}\,\frac{1}{4\pi^2}\int_{-\infty}^{+\infty}\int_{-\infty}^{+\infty}\tilde{A}_S(z_F,z_S,k_\rho)\exp(-jk_\rho\rho)d_2k_\rho \tag{2.58}$$

where

$\mathbf{r}_S$ and $\mathbf{r}$ denote the position vectors of the source- and field locations, respectively

$\mathbf{r}_S = x_S\;\hat{x} + y_S\;\hat{y} + z_S\;\hat{z}$

$\mathbf{r} = x_F\;\hat{x} + y_F\;\hat{y} + z_F\;\hat{z}$

$\rho\;\hat{\rho} = (x_F - x_S)\;\hat{x}+\;(y_F - y_S)\;\hat{y}$

$k_\rho\;\hat{\rho} = k_x\;\hat{x} + k_y\;\hat{y}$

d_2k_ρ denotes the two-dimensional differential quantity in k_ρ and

$$\tilde{A}_S(z_F,z_S,k_\rho) = \frac{\mu_S}{2jk_{zS}}\exp(-jk_{zS}\left|z_F - z_S\right|) \tag{2.59}$$

Here $k_{zS} = \sqrt{k_S^2 - k_\rho^2}$ where the square root is evaluated such that $Imag(k_{zS}) \leq 0$

Separating (2.59) into the source spectral amplitude $\tilde{A}_{S0}$ and the spectral transfer function T_{S0} between the source and the observation point we can write

$$\tilde{A}_S(z_F,z_S,k_\rho) = \tilde{A}_{S0}T_{S0}(z_F,z_S,k_\rho) \tag{2.60}$$

where

$$\tilde{A}_{S0} = \frac{\mu_S}{2jk_{zS}} \tag{2.61}$$

$$T_{S0}(z_F,z_S,k_\rho) = \exp(-jk_{zS}\left|z_F - z_S\right|) \tag{2.62}$$

In a multilayer medium the magnetic vector potential $\mathbf{A}$ due to an electric current element, that is of unit intensity and parallel to the dielectric interfaces, comprises two components. For example, a x-directed current element parallel to xy plane (Fig. 2.8) contributes to A_{xx} and A_{zx} components only. Meanwhile, an electric current element perpendicular to the dielectric interfaces has one component, i.e. a z-directed current element in the same medium contributes to A_{zz} component only. In addition, in a source-free region, the fields in a stratified medium can be conveniently decomposed into TE (Transverse Electric) and TM (Transverse Magnetic) components. Their propagation in the spectral domain is analogous with the wave propagation in a transmission line in the space domain. Therefore when the plane wave spectrum representation is used for each component of the potentials, their propagation in the spectral domain can be modelled by a cascade of transmission lines. Thus, expressing the field generated in the source layer in terms of a plane-wave spectrum and comparing their propagation in spectral domain with the spatial wave propagation in a cascaded transmission line, one can determine the field components at any location of interest. Here we are primarily concerned with the electric current sources parallel to the dielectric interfaces, which is considered next.

2.6.2 Horizontal electric dipole

Let us assume that current density of the horizontal source is given by (2.56) after replacing unit vector $\hat{u}$ by $\hat{x}$. It is also assumed that the dielectric interfaces are parallel to the xy plane. Then the expressions for vector potential components $\tilde{A}_{xx}$ and $\tilde{A}_{zx}$ and scalar potential $\tilde{\phi}_x^q$ in spectral domain can be derived. As shown in [7], TE waves lead to the following expression for $\tilde{A}_{xx}$

$$\tilde{A}_{xx}(z_F, z_S, k_\rho) = \tilde{A}_{S0} T_{TE}(z_F, z_S, k_\rho) \tag{2.63}$$

where

$$T_{TE}(z_F, z_S, k_\rho) = \frac{\tilde{E}_x(z_F)}{\tilde{E}_{x0}} = \frac{V(z_F)}{Z_s I_s/2} \tag{2.64}$$

Here, $\tilde{E}_x(z_F)$ and $\tilde{E}_{x0}$ denote the spectral amplitudes of the x directed electric field intensity at the field point and at the source, respectively. $V(z_F)$ is the voltage defined at the field point of the corresponding transmission line model. Z_s is the wave impedance of the source layer and the current source I_s represents the source in the corresponding transmission line model.

Following the same approach which led to (2.55), but replacing the series-voltage source V_s by parallel-current source I_s and, the characteristic impedances Z_n in (2.54) by their TE equivalents given by

$$Z_n = \frac{\omega \mu_n}{k_{zn}} \tag{2.65}$$

$T_{TE}(z_F, z_S, k_\rho)$ can be easily found. It will be in the form of

$$T_{TE}(z_F, z_S, k_\rho) = \frac{a_S \begin{bmatrix} 1 & \Gamma_S \end{bmatrix} \begin{bmatrix} 1 & \Gamma_L \end{bmatrix}^T a_L}{P} \tag{2.66}$$

Since both TE and TM waves contribute to $\tilde{A}_{zx}$ it can be expressed as

$$\tilde{A}_{zx}(z_F, z_S, k_\rho) = -\frac{k_x}{k_\rho^2} \tilde{A}_{S0} \left(\frac{\mu_F}{\mu_S} k_{zS} T_{TM}(z_F, z_S, k_\rho) - j \frac{\partial T_{TE}(z_F, z_S, k_\rho)}{\partial \zeta_F} \right) \tag{2.67}$$

Now, $T_{TM}(z_F, z_S, k_\rho)$ is given by (2.55) when the impedances Z_n are replaced by :

$$Z_n = \frac{k_{zn}}{\omega \varepsilon_n} \tag{2.68}$$

In addition, the scalar potential $\tilde{\phi}_x^q$ can be written as

$$\tilde{\phi}_x^q = \frac{\tilde{A}_{S0}}{\varepsilon_F \mu_S k_\rho^2} \left(\frac{\mu_S k_F^2}{\mu_F} T_{TE}(z_F, z_S, k_\rho) - j k_{zS} \frac{\partial T_{TM}(z_F, z_S, k_\rho)}{\partial \zeta_F} \right) \tag{2.69}$$

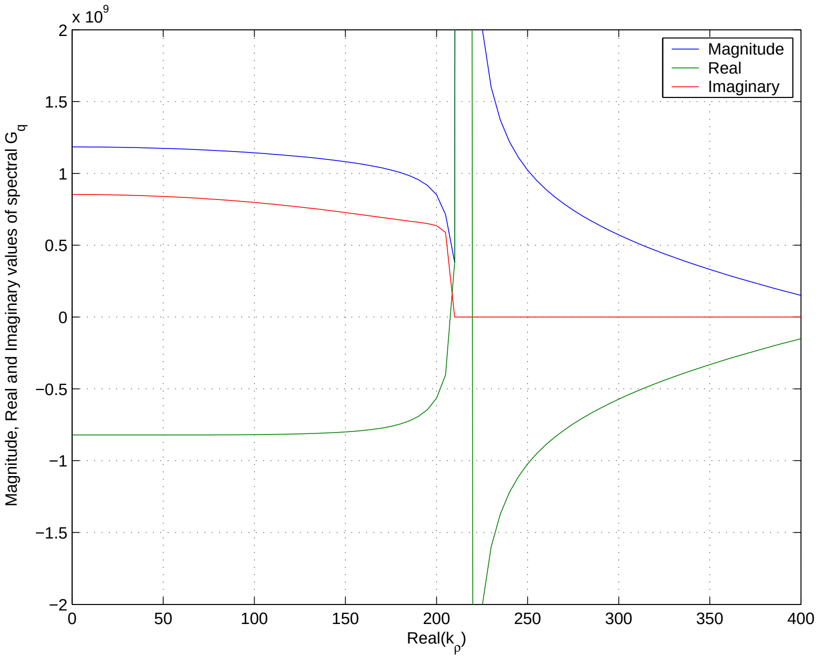

Fig. 2.4: *Magnitude, real and imaginary parts of the spectral scalar Green's function of a thin grounded dielectric layer*

2.7 Characteristics of Spectral Green's Functions for a Stratified Medium

The properties of the spectral Green's function for stratified media are dominated very much by its singular points rather than zero points. Two types of singular points exist: poles and branch points. The branch points are usually attributed to radiation into unbounded layers whereas the poles are attributed to surface wave propagation. Because of these singular points, one should be very cautious when dealing with spectral Green's functions.

In order to emphasize this point, the scalar Green's function in spectral domain for a grounded dielectric layer is shown in Fig. 2.4 - 2.7. The dielectric constant and the thickness of the dielectric layer are chosen as 12.6 and 1 mm. The frequency is set to 10 GHz. The source is located at the dielectric to air interface. The fields are also calculated at the source. Due to the branch point and the associated branch cut, the imaginary part of the selected Green's function shows a discontinuity, whereas the real part is continuous. Figures 2.6 and 2.7 clearly exhibit the behavior of a branch point at $k_\rho = k_0 = 209.58$. This branch point is closely followed by a surface-wave pole as illustrated by Fig. 2.4 and 2.5. At this surface wave pole, the magnitude of the Green's function approaches infinity.

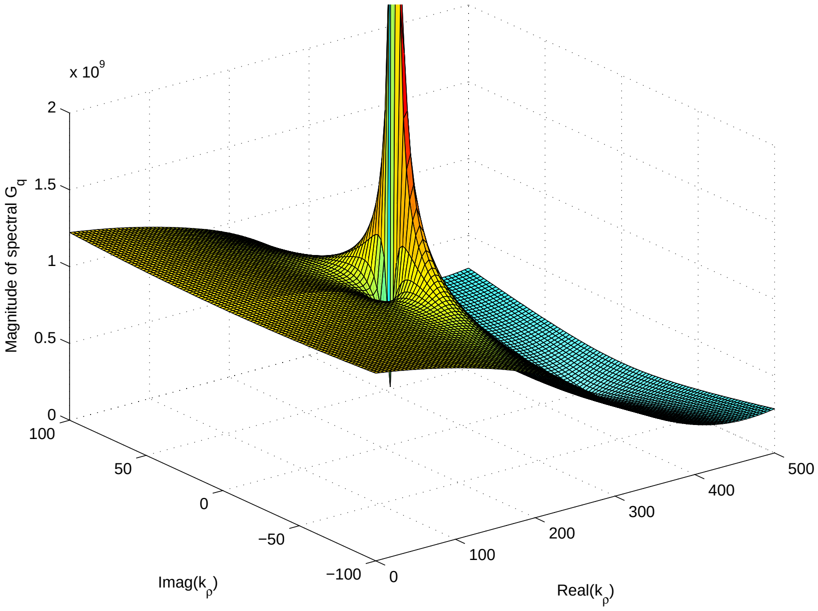

Fig. 2.5: *Magnitude of the spectral scalar Green's function of a thin grounded dielectric layer*

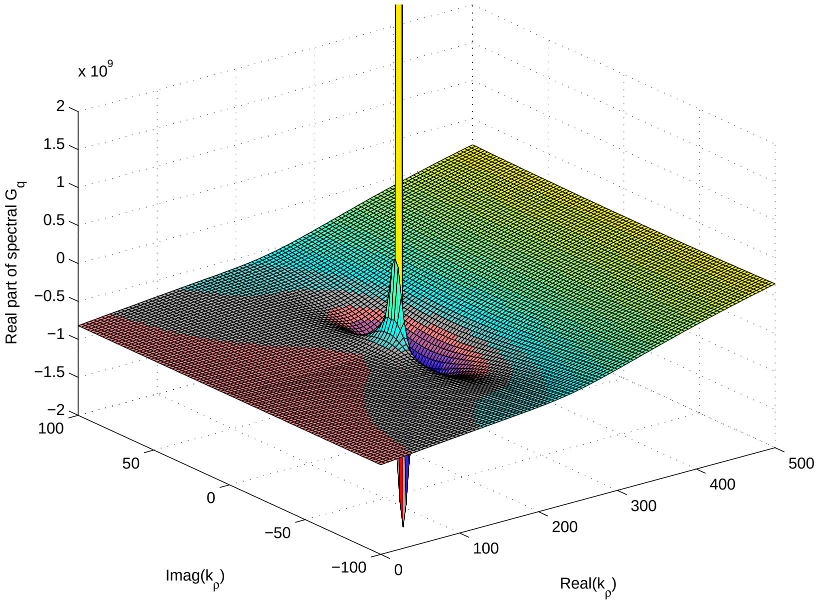

Fig. 2.6: *Real part of the spectral scalar Green's function of a thin grounded dielectric layer*

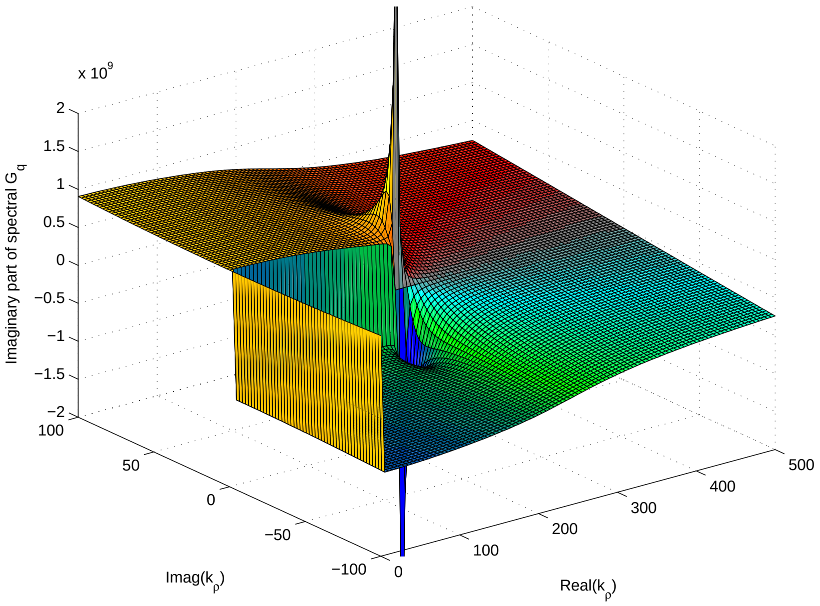

Fig. 2.7: *Imaginary part of the spectral scalar Green's function of a thin grounded dielectric layer*

2.8 Numerical Evaluation of Spatial Green's Functions

The transformation (2.13) converts spectral Green's function into its spatial counterpart in rectangular coordinate system. Following the approach presented in [10] this transformation can be written in cylindrical coordinate system

$$\psi_n(\rho) = \frac{1}{2} \sum_n \int_{\infty e^{-j\pi}}^{+\infty} \Psi_n(k_\rho)\; H_n^{(2)}(k_\rho \rho)\; k_\rho dk_\rho \tag{2.70}$$

where

the integration limit $\infty e^{-j\pi}$ denotes that the infinity is approached from the third quadrant in the complex plane, below the branch cut and along the negative real axis (SIP in Fig. 2.9),

$H_n^{(2)}(x)$ is the Hankel function of the second kind and n'th order,

k_ρ is the propagation constant along the radial direction $\hat{\rho}$ and

$\psi_n(\rho)$ is defined exploiting the inherent periodicity present in $\psi(\rho, \phi)$ with respect to ϕ (Fig. 2.8). It can be expressed as a Fourier series in ϕ domain,

$$\psi(\rho, \phi) = \sum_n \psi_n(\rho, \phi) = \sum_n \psi_n(\rho) e^{jn\phi} \tag{2.71}$$

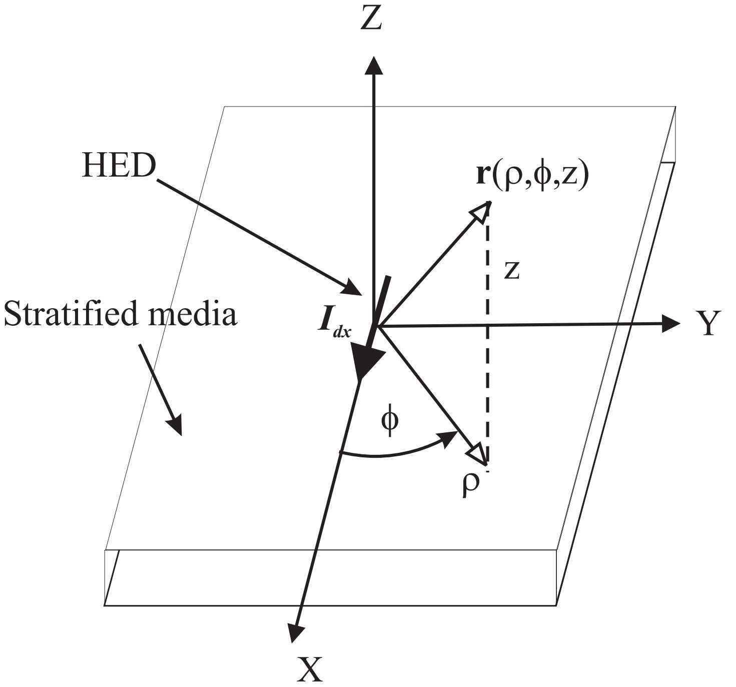

Fig. 2.8: *A HED on a stratified medium*

$\Psi_n(k_\rho)$ denotes the spectral counterpart of $\psi_n(\rho)$.

2.8.1 Sommerfeld integrals

A typical Sommerfeld integral (SI) is denoted by [11]

$$\psi_0(\rho) = \frac{1}{2} \int\limits_{SIP} \Psi_0(k_\rho)\ H_0^{(2)}(k_\rho \rho)\ k_\rho dk_\rho \tag{2.72}$$

where the path SIP (Sommerfeld Integration Path) is as shown in Fig. 2.9. The same integral can be acquired by substituting $n = 0$ in (2.70). The resulting $\psi_0(\rho)$ component is equivalent to $\psi_0(\rho, \phi)$ in (2.71) and is obviously independent of ϕ. Such an independency is typical for spectral vector and scalar Green's functions of an infinitesimal HED placed in a stratified medium [12]. Nevertheless, the resulting electric field components always depend on ϕ.

The integral (2.72) can alternatively be expressed in terms of Bessel function of zeroth order, J_0 [10]

$$\psi_0(\rho) = \int\limits_{SIP/2} \Psi_0(k_\rho)\ J_0(k_\rho \rho)\ k_\rho dk_\rho \tag{2.73}$$

The path SIP/2 is shown in Fig. 2.10. This form is often preferred in evaluating spatial Green's functions numerically, due to its shorter range of integration.

2.8.2 Numerical evaluation of Sommerfeld integrals

Although the application of asymptotic techniques, such as the method of steepest descent path (SDP), are widely used in literature in evaluating Sommerfeld type integral, it is the direct numerical integration of such integrals that offers the best accuracy and insight. However, the numerical evaluation of SI is inherently cumbersome due to the presence of branch points, branch cuts and number of complex poles found in the vicinity of the Sommerfeld integration path (SIP) illustrated in Fig. 2.9. The selection of a more convenient path attracted the attention of many authors in the past [10] [3] [13]. The trick is to traverse a path further away from the singular points (e.g. Fig. 2.11) such that the resulting integrand along the newly selected path is well-behaved (Fig. 2.13). If this path deforming process agrees with the Cauchy's theory of contour integration [14], the computed value is equal to the value along the original SIP. A typical behavior of $\Psi_0(k_\rho)$ in (2.73) along SIP and modified SIP is shown in Fig. 2.13.

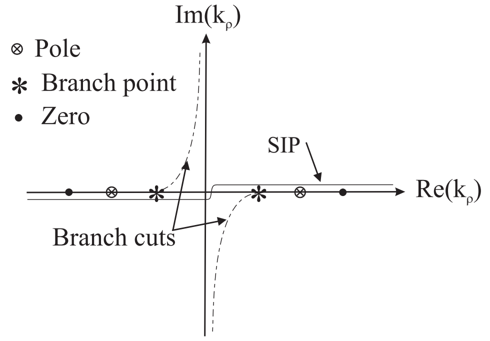

Fig. 2.9: *Sommerfeld integration path (SIP), branch cuts, branch points, zeros and poles of a typical spectral Green's function of a stratified medium*

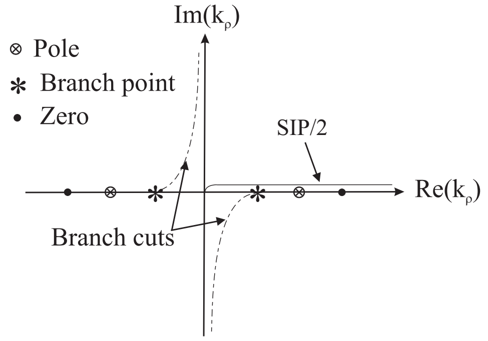

Fig. 2.10: *Modified Sommerfeld integration path (denoted as SIP/2) applied with Bessel function of zeroth order*

In addition to the ill-behavior manifested nearby the singular points, a typical spectral Green's function decays slowly with increasing k_ρ. Moreover, the resulting integrand is highly oscillatory due to the presence of Bessel type functions. Hence, for large k_ρ the integral can be considered as a summation of negative and positive contributions. All these factors make the integral (2.73) either slowly convergent or, in some extreme cases, divergent.

2.8.3 Methods for accelerating the numerical evaluations

Although the selection of a new convenient path eliminates the difficulties encountered near the branch points and poles, it does not affect the convergent rate of the oscillatory part. Therefore other techniques that accelerate the convergence of this part of the

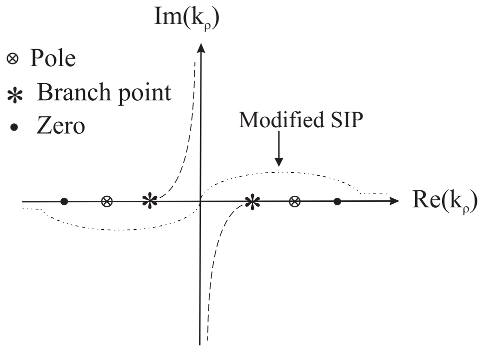

Fig. 2.11: *Modifying the Sommerfeld integration path (SIP) in order to mitigate the ill-behavior of Green's function near the singular points*

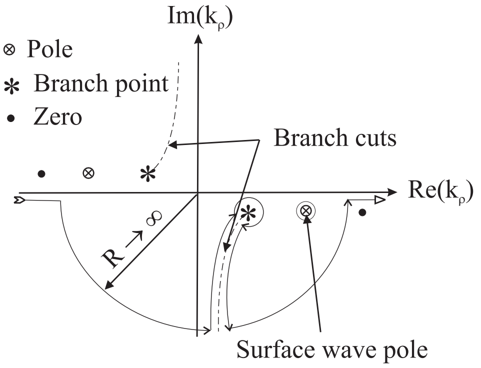

Fig. 2.12: *Modifying the Sommerfeld integration path (SIP) in order to separate the contributions into surface and space waves*

integral have to be applied. An overview of different methods is given in [15], [16], [17], and [18]. In our evaluation of spatial Green's functions, a technique known as epsilon ($\epsilon-$) algorithm is employed because it can be easily formulated and implemented in software. Moreover, the resulting rate of convergence is adequate for our purpose. The $\epsilon-$algorithm was presented in [19] as an alternative way to evaluate the original Shank's transformation [20].

In order to evaluate $\psi_0(\rho)$ in (2.73), let us first separate the original integral into two; $\psi_0^1(\rho)$ and $\psi_0^2(\rho)$, as shown in (2.74)-(2.76). The integral $\psi_0^1(\rho)$ represents the part of $\psi_0(\rho)$, on which the branch points and poles of $\Psi_0(k_\rho)$ have a dominant effect. On the other hand, $\psi_0^2(\rho)$ corresponds to the part, which is highly oscillatory and slowly decaying.

$$\psi_0(\rho) = \int\limits_{SIP/2} \Psi_0(k_\rho)\; J_0(k_\rho\rho)\; k_\rho dk_\rho \tag{2.74}$$

$$= \int_0^{\infty} \Psi_0(k_\rho)\; J_0(k_\rho\rho)\; k_\rho dk_\rho$$

$$= \int_0^{a} \Psi_0(k_\rho)\; J_0(k_\rho\rho)\; k_\rho dk_\rho + \int_a^{\infty} \Psi_0(k_\rho)\; J_0(k_\rho\rho)\; k_\rho dk_\rho \tag{2.75}$$

$$= \psi_0^1(\rho) + \psi_0^2(\rho) \tag{2.76}$$

The integration paths (and the parameter a) are selected following the same considerations given in chapter 3. $\psi_0^1(\rho)$ can now be parameterized and evaluated using the efficient numerical integration algorithms suggested in chapter 5.

However due to its oscillatory and slow-damping nature, the evaluation of $\psi_0^2(\rho)$ needs a rather different approach. $\psi_0^2(\rho)$ is first expressed as a sum of many partial integrals defined over each half cycle (period) of the integrand. The corresponding limits of integration are easily determined by the zeros of the Bessel function J_0. These zeros are either

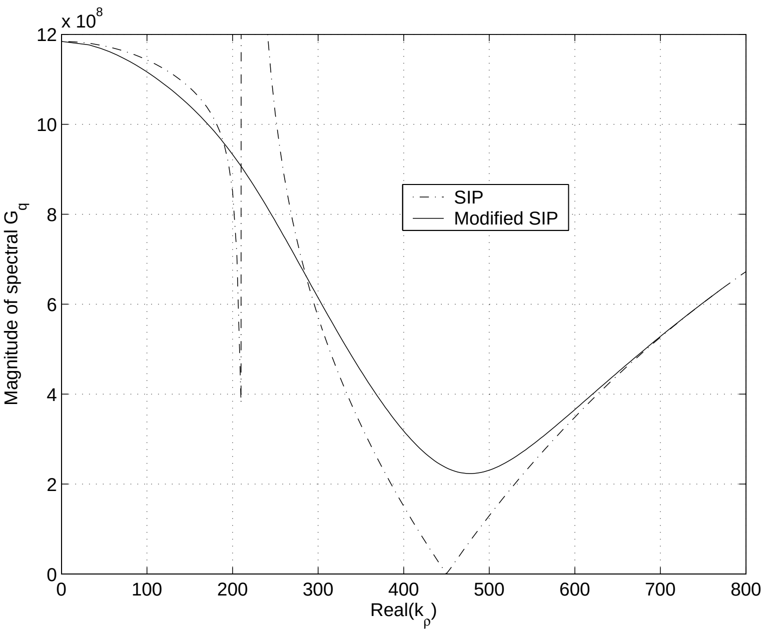

Fig. 2.13: *The value of a typical Green's function along the original SIP and the suggested modified SIP as given in Fig. 2.11*

available in tabular form [21] or determined accurately using zero-finding algorithms. We adapt a combination of both methods. The tabulated values are used whenever their accuracy is adequate, which is the case for lower order zeros. When the accuracy is critical, as required by higher order zeros, a numerical zero-finding algorithm [22] is employed. Now, $\psi_0^2(\rho)$ can be expressed as

$$\begin{aligned} \psi_0^2(\rho) &= \sum_{n=0}^{\infty} \int_{a+p_n}^{a+p_{n+1}} \Psi_0(k_\rho)\ J_0(k_\rho \rho)\ k_\rho dk_\rho \qquad (2.77) \\ &= \sum_{n=0}^{\infty} I_n \end{aligned}$$

where

p_n denotes the n'th zero of $J_0(k_\rho \rho)$ and p_0 is set to zero thereby including the contributions over the region $[a, p_1]$ and

I_n represents the subintegrals resulted from integrating in between two adjoint zeros.

All the subintegrals I_n are now added together applying ϵ-algorithm [19]. Since the ϵ-algorithm significantly improves the convergence of the summation given in (2.77), the number of I_n terms to be calculated numerically are reduced significantly. This means that the application of ϵ-algorithm to determine $\psi_0^2(\rho)$ reduces the computational time dramatically and eases memory requirements.

2.8.4 Surface and space wave components

When the spatial Green's functions are found applying either (2.72) or (2.73), the total field produced by a more general source can be calculated. Such fields generally comprise two distinct wave components: a space wave component and a surface wave component. The space wave component propagates away from the source in all directions contributing to the far-field radiation whereas the surface wave component propagates along the dielectric-to-dielectric interface.

In order to demonstrate the effect of these two wave components on the spatial Green's function, we shall calculate, for example, the spatial scalar Green's functions of a dielectric layer over an ideal ground plane. We assumed that a HED is located on the dielectric-to-air interface. The relative dielectric coefficient ε_r of the dielectric material is 12.6 and the operational frequency is 10 GHz. The spatial scalar Green's function at the location of the source is evaluated. Figure 2.14 shows the magnitude of this spatial scalar Green's function as a function of $k_0\rho$, when the dielectric layer is 1mm-thick. The same quantity for a 3mm-thick dielectric layer is given in Fig. 2.15. Comparing these two figures, it is obvious that spatial scalar Green's function of the 1mm-thick substrate decays rapidly away from the source whereas the spatial scalar Green's function of the 3mm-thick substrate shows an oscillatory behavior away from the source. Such an oscillatory behavior is very typical for spatial Green's functions with a dominant surface wave component. For the sake of completeness we illustrate the corresponding phase values for both instances in Fig. 2.16 and 2.17 as well.

Note that if the lateral distance between two sources situated side by side in a stratified medium is large enough, the mutual coupling between them is dominated by the contribution from surface waves whereas the space wave contributes significantly less. On the other hand, if they are aligned on a vertical plane and the vertical separation between them are large enough, the space wave would contribute more to the mutual coupling because the surface waves decay exponentially away from the dielectric-to-dielectric interfaces [23].

By deforming the SIP of the Sommerfeld integral in the particular way shown in Fig. 2.12, the contributions from space waves and surface waves can be determined separately. According to the Cauchy's theory of contour integration, this deformed path captures some singular points. It is shown in [23] that these singular points directly contribute to the surface waves while the rest of the integration path contributes to the space wave. In particular, the integration path around the branch cut contributes significantly to the radiated far fields.

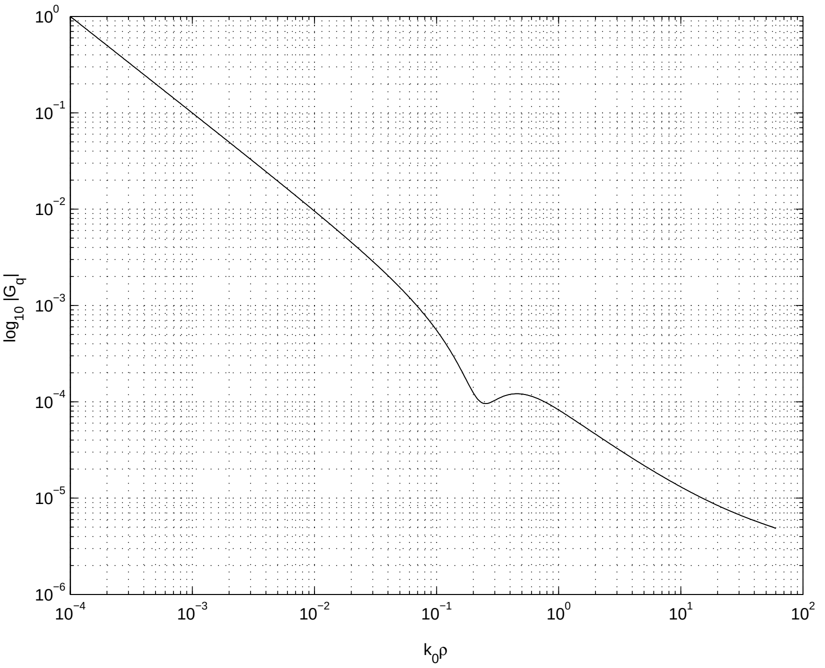

Fig. 2.14: *Magnitude of the space domain scalar Green's function of a thin (1 mm thick) grounded dielectric layer*

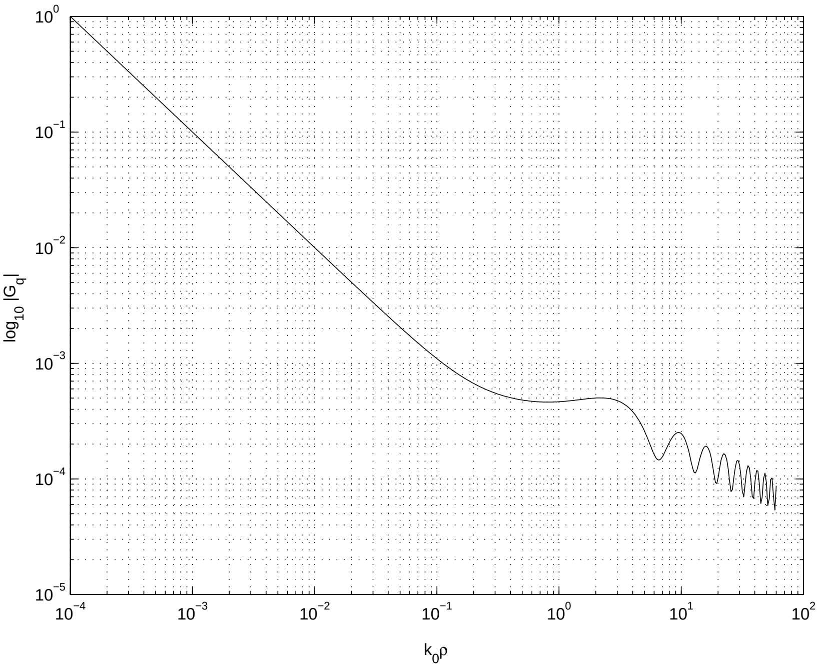

Fig. 2.15: *Magnitude of the space domain scalar Green's function of a thick (3 mm thick) grounded dielectric layer*

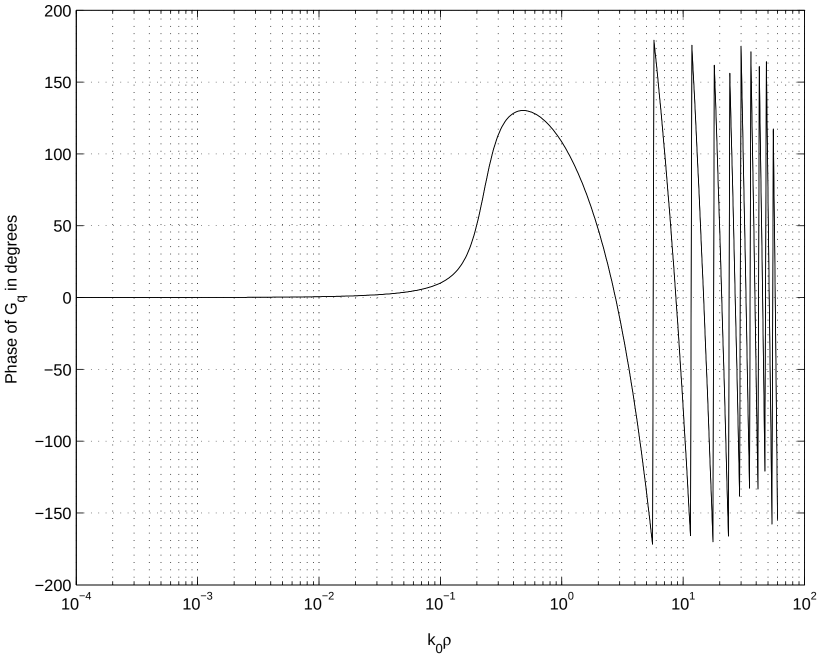

Fig. 2.16: *Phase angle of the space domain scalar Green's function of a thin (1 mm thick) grounded dielectric layer*

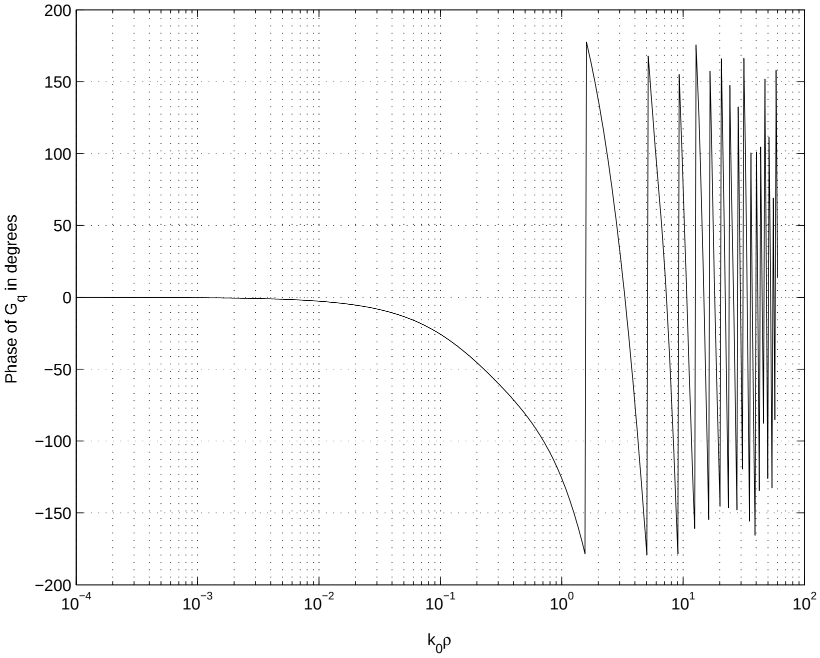

Fig. 2.17: *Phase angle of the space domain scalar Green's function of a thick (3 mm thick) grounded dielectric layer*

Chapter 3

Discrete Complex Image Method

3.1 Introduction

The use of various image principles in electromagnetic field calculations has been popular since the introduction of the famous Maxwell's equations. These methods do not only save much of the calculation effort but also provide an intuitive explanation of the results. Until recently, the images have been real and are located in the real space [24][25][26]. Following the introduction of images in complex space to represent reflected fields of a vertical magnetic dipole (VMD) in the presence of a lossy half space, I. S. Lindell extended the image theories into the complex space [27]. In [27], the reflected fields from a VMD over a lossy dielectric were represented by a continuous complex line source located in complex space. Although it was analytically proved that this image led to an accurate result, their continuous nature still made them difficult to apply in numerical calculations.

The discretization of this continuous complex image was later accomplished by D. G. Fang et al. [28]. They introduced an alternative method for approximating the space domain Green's functions (GFs) of a thick dielectric substrate. It is well known that even though the spectral domain GFs of a stratified media can be found in closed form, there is no general way to find a closed form expression for its space domain counterpart. The only way to find a value of a space domain Green's function is to perform the (Inverse) Hankel transformation numerically, in other words, to evaluate Sommerfeld integral (SI) numerically. The evaluation of Sommerfeld integrals in this context is time consuming and numerically unstable due to the presence of branch points, branch cuts and poles in spectral GFs and the slowly-decaying-oscillatory nature of the integrand (chapter 2). However, the innovative method in [28], which was later known as the discrete complex image method (DCIM) led to well-approximated closed form expressions for space domain GFs.

The method basically expresses the spectral domain GF as a sum of complex exponential terms and afterwards uses the Sommerfeld identity for transforming them into the corresponding space domain GF. The originally proposed method is a three-step-process, which is a combination of both analytical and numerical methods. It uses Prony's method for extracting exponential terms in spectral GFs. Later, M. I. Aksun et al. made the DCIM more robust by introducing it as a pure numerical method [29]. The powerful generalized pencil-of-function (GPOF) method, which is based on singular value decomposition (SVD), was applied for extracting exponential terms. The method has shown to perform very well in near- and intermediate regions where the existence of surface waves hardly affects the results.

In this chapter, we introduce a practical implementation of the DCIM. We begin with the version published [29]. The problems encountered during the implementation and the solutions applied, are discussed. In order to reduce the numerical instabilities and to achieve the best performance, we suggest several minor modifications of the GPOF algorithm. We shall also discuss the limitations of the present version of DCIM and the ways to alleviate them.

3.2 Discrete Complex Image Method

3.2.1 Original approach

Although it was Fang et al. who introduced the discrete complex images for stratified media [28], it was indeed Y. L. Chow et al. who presented them as a methodical way of approximating spatial (space domain) Green's functions with sufficient accuracy [30]. Therefore, we consider the method introduced by Y. L. Chow et al. as the original method which laid the foundation for the robust method introduced later by A. I. Aksun.

The original method represents the spatial Green's function in terms of three sets of complex images [30];

- a set of images that dominate in the near-field region and correspond to quasi-static waves
- a set of images that dominate in the far-field region and represent the contribution from surface waves
- a set of images that dominate in the intermediate region and represent the contribution from leaky waves

It is obvious that each component is dominant in rather mutually exclusive areas. They together lead to an adequate representation of spatial GF over the entire domain of the radial distance. In a nutshell, this method can be illustrated by the block diagram in Fig. 3.1.

3.2.2 Robust approach

In order to eliminate shortcomings such as less robustness and difficulty in automating etc. found in the original approach, a robust DCIM was introduced [29]. We shall now

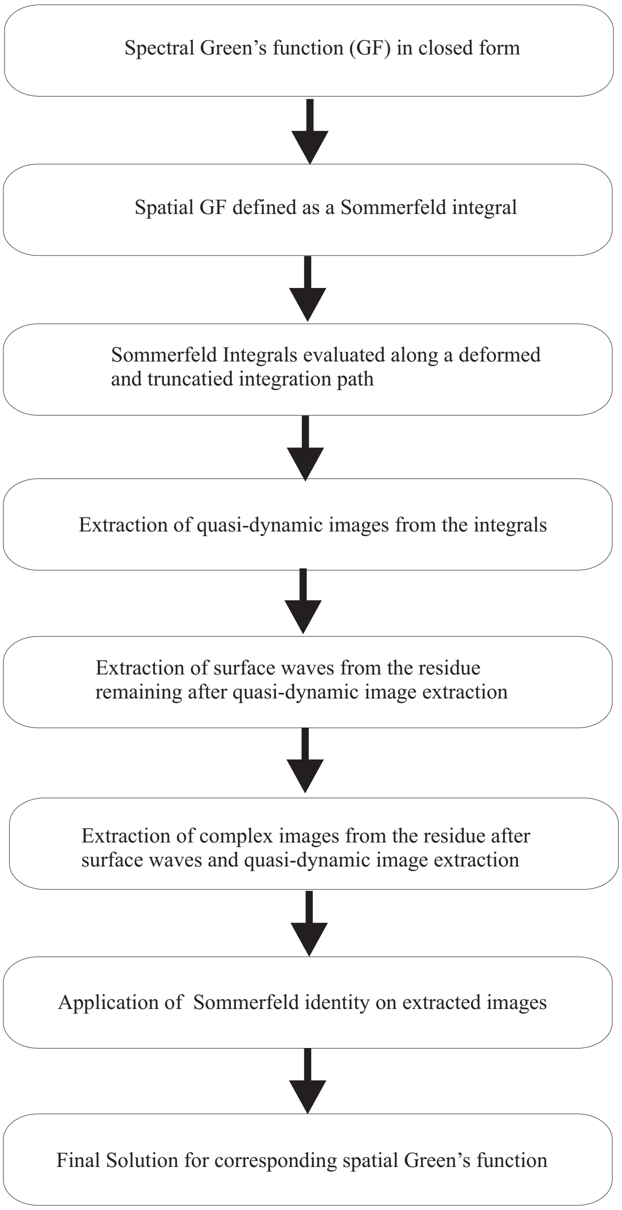
Spectral Green's function (GF) in closed form
Spatial GF defined as a Sommerfeld integral
Sommerfeld Integrals evaluated along a deformed and truncatied integration path
Extraction of quasi-dynamic images from the integrals
Extraction of surface waves from the residue remaining after quasi-dynamic image extraction
Extraction of complex images from the residue after surface waves and quasi-dynamic image extraction
Application of Sommerfeld identity on extracted images
Final Solution for corresponding spatial Green's function

Fig. 3.1: *The block diagram showing the major steps in original [30] discrete complex image method*

present this method, and all future occurrences of DCIM will refer to this method. The basic distinction of this version of DCIM is that it does not explicitly handle either the quasi-static images or the surface wave poles. Instead, they are partially taken care of by the same uniform method of extracting complex images. Nevertheless, the extraction of images are still divided into different phases. Although the surface waves can not be fully represented by complex images due to their $1/\sqrt{r}$ radial decay versus the $1/r$ radial decay of complex images, this method still gives satisfactory results in near and moderately far regions.

We shall divide the implementation of this method into two major steps.

Step one In this step the slowly varying part of the spectral Green's function is approximated by a sum of complex images. It is comparable with the extraction of quasi-static images mentioned in the original method. Therefore these images are dominant in the near field region of the corresponding spatial Green's function.

Step two Extraction of complex images in the second steps is carried out to approximate the residue of the spectral Green's function, remained after the extraction of complex images in step one. Thus, the rapidly varying components of the spectral Green's function are represented by the images found in step two. Their contribution to the spatial Green's function is especially significant in the intermediate- and moderately-far-field regions.

In the following, we shall go into details of the algorithm.

Sommerfeld integral with a deformed integration path

In contrast to the single deformed integration path used in the original method, the integration path now comprises two distinct contours. Continuing the discussion on Sommerfeld integral started in chapter 2 these contours in complex k_{zs}, $C^1_{k_{zs}}$ and $C^2_{k_{zs}}$, are chosen as in Fig. 3.2. The complex domain k_{zs} is defined as $k_{zs} = \sqrt{k_s^2 - k_\rho^2}$ where the square root is evaluated such that $Imag(k_{zs}) \leq 0$. k_s denotes the propagation constant in the source layer. The same figure denotes the original Sommerfeld integral path in complex k_{zs} as C^{SIP}. Meanwhile Fig. 3.3 maps the contours $C^1_{k_{zs}}$ and $C^2_{k_{zs}}$ to the contours $C^1_{k_\rho}$ and $C^2_{k_\rho}$ in complex k_ρ plane, respectively. Comparing this figure with the typical behavior of the spectral GF illustrated in Fig. 2.4 and Fig. 2.13, it is obvious that $C^1_{k_\rho}$ and $C^2_{k_\rho}$ traverse the static and dynamic parts of the spectral GF, respectively. The parametric representations of contours $C^1_{k_{zs}}$ and $C^2_{k_{zs}}$ is straight forward and given as

$$\begin{array}{llll} C^1_{k_{zs}}: & k_{z_i} = & -jk_s\,(T_2 + t) & 0 \leq t \leq T_1 \\ C^2_{k_{zs}}: & k_{z_i} = & k_s\left[-jt + \left(1 - \frac{t}{T_2}\right)\right] & 0 \leq t \leq T_2 \end{array} \tag{3.1}$$

Here, k_s is the propagation constant in the source layer and t defines the parametric domain. The value of T_1 is chosen to ensure the behavior of spectral GF for large k_ρ is captured whereas the parameter T_2 decides how accurate the path $C^2_{k_\rho}$ captures the dynamic behavior of the spectral GF. Therefore, T_2 has to be chosen such that it is

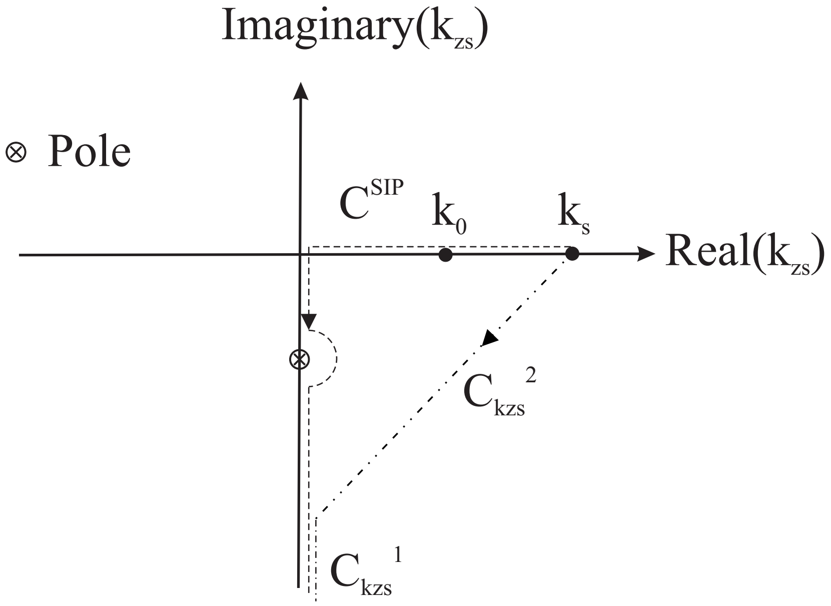
Imaginary(k_{zs})
⊗ Pole
C^{SIP}
k_0
k_s
Real(k_{zs})
C_{kzs}^2
C_{kzs}^1

Fig. 3.2: *The integration contours $C^1_{k_{zs}}$ and $C^2_{k_{zs}}$ on the complex k_{zs} plane*

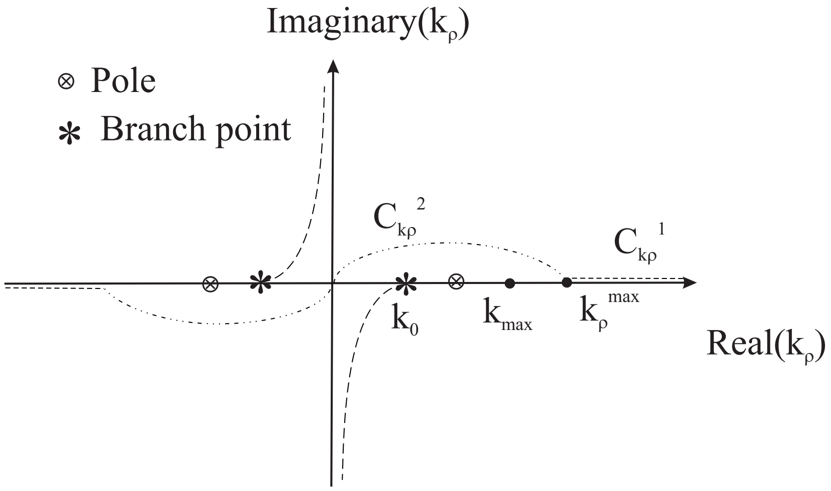
Imaginary(k_ρ)
⊗ Pole
∗ Branch point
$C_{k\rho}^2$
$C_{k\rho}^1$
k_0
k_{max}
k_ρ^{max}
Real(k_ρ)

Fig. 3.3: *The integration contours $C^1_{k\rho}$ and $C^2_{k\rho}$ on the complex k_ρ plane*

small enough to capture the significant characteristics of the GF accurately. At the same time, it should be large enough to acquire numerically well-behaved spectral GF over $C^2_{k_\rho}$. So the selection of the parameter T_2 is based on the judicious compromise. It can be shown that when T_2 is selected as the square root of the maximum dielectric constant of the stratified media, it will lead to satisfactory results [29]. This selection is quite logical because it is well known that all the poles of a spectral GF of a lossless stratified structure are confined to the region of $[k_0\ ,\ \sqrt{\varepsilon_{\max}}k_0]$ in k_ρ domain; where $\varepsilon_{\max}$ is the maximum dielectric constant of the media and k_0 is the propagation constant in free space [5]. Therefore by selecting T_2 as the square root of $\varepsilon_{\max}$, all the potential spikes along the integration path due to the nearby poles are satisfactorily smoothed out. This selection also sets the value of $k_\rho^{\max}$, specified in Fig. 3.3, to $k_s\sqrt{1+\varepsilon_{\max}}$. The other contour segment $C^1_{k_\rho}$ is a part of the original Sommerfeld integration path (Fig. 3.2). Here the parameter T_1 has to be selected in such way that the spectral GF should be well stabilized at the end of the path $C^1_{k_\rho}$.

Let us assume that the original spectral GF is denoted by $\tilde{G}(k_{zs})$. In order to facilitate the application of Sommerfeld identity later in the procedure, we both divide and multiply $\tilde{G}(k_{zs})$ with $2jk_{zs}$, then define the normalized spectral GF, $\tilde{G}_n(k_{zs})$ as follows [31].

$$\begin{aligned}\tilde{G}(k_{zs}) &= \frac{2jk_{zs}}{2jk_{zs}}\tilde{G}(k_{zs}) = \frac{1}{2jk_{zs}}(2jk_{zs}\tilde{G}(k_{zs})) \\ &= \frac{1}{2jk_{zs}}\tilde{G}_n(k_{zs}) \end{aligned} \tag{3.2}$$

where $k_{zs}^2 = k_s^2 - k_\rho^2$.

Extraction of first group of complex images: step one

In order to extract the first group of complex images which dominate in the near field region, we have to approximate $\tilde{G}_n(k_{zs})$ with some finite number of real or complex exponential terms. Their amplitudes can in general be complex. Both the Prony's method (PM) and the generalized pencil-of-function (GPOF) method are widely applied in the literature to accomplish this task. They both equally require the spectral data to be discrete. Therefore we have to convert the continuous and generally complex spectral GF values into a discrete complex data sequence without any significant loss of accuracy. Typically the spectral GF over the path $C^1_{k_\rho}$ is not rapidly varying. For example a typical variation of spectral GF over $C^1_{k_\rho}$ can be shown as in Fig. 3.6. Therefore, it is not necessary to have samples which are tightly close to each other in order to represent the full dynamics of the spectral GF over this region. It is also understood that the number of samples depends on the value selected for the parameter T_1 defining the path segment $C^1_{k_\rho}$. The smaller T_1 is, the fewer the required number of samples are.

Following the discretization process, either the PM or the GPOF can be used to extract the complex exponential functions. We shall later in this chapter discuss these two methods. The extraction of exponential terms in t-domain leads to the following approximation for the normalized spectral GF over path $C^1_{k_\rho}$,

$$\tilde{G}^1_{n_{approx}}(k_\rho) = \sum_{l=1}^{N_1} a^t_l \exp(b^t_l t) \tag{3.3}$$

Here the superscript 1 of $\tilde{G}^1_{n_{approx}}(k_\rho)$ denotes that the approximation is only valid in the region defined by parameter $t \in [0, T_1]$. The superscript t over a and b denotes that a and b are constants defined in t-domain. a^t_l and b^t_l are easily extracted using either Prony's method or GPOF method. N_1 is the number of images found. These images are often referred to as quasi-static images.

When these exponential terms are transformed back to k_{zs}-domain, following a similar notation as above [29],

$$\tilde{G}^1_{n_{approx}}(k_{zs}) = \sum_{l=1}^{N_1} a^{k_{zs}}_l \exp(b^{k_{zs}}_l k_{zs}) \tag{3.4}$$

where

$$b^{k_{zs}}_l = -\frac{b^t_l}{jk_s} \tag{3.5}$$

$$a^{k_{zs}}_l = a^t_l \exp(jk_s b^{k_{zs}}_l T_2) \tag{3.6}$$

Extraction of second group of complex images: step two

Since the first approximation is only based on the spectral GF evaluated over the contour $C^1_{k_\rho}$, it may not in general give the correct values when extrapolated into the region defined by the contour $C^2_{k_\rho}$. In order to approximate the correct spectral GF over $C^2_{k_\rho}$, we should include more complex exponential terms, which approximate the residue over $C^2_{k_\rho}$. The residue over $C^2_{k_\rho}$ is the difference between the spectral GF over $C^2_{k_\rho}$ and the approximated spectral GF over $C^1_{k_\rho}$ extended to $C^2_{k_\rho}$. Hence, the residue $\tilde{G}^r_n(k_\rho)$ can be defined as

$$\tilde{G}^r_n(k_\rho) = \tilde{G}_n(k_\rho) - \tilde{G}^{1^{extended}}_{n_{approx}}(k_\rho) \tag{3.7}$$

where $\tilde{G}^{1^{extended}}_{n_{approx}}(k_\rho)$ represents the extrapolated $\tilde{G}^1_{n_{approx}}(k_\rho)$ into the region $C^2_{k_\rho}$.

Now the residue $\tilde{G}^r_n(k_\rho)$ can also be expressed in complex exponential terms as we did in step one. Here, in order to take care of rapid variations of spectral GF over $C^2_{k_\rho}$, due to its proximity to branch points and complex poles, the sampling frequency has to be chosen considerably higher than that of step one. In other words, samples have to be close enough to represent the complete dynamic of the spectral GF over $C^2_{k_\rho}$. Upon the extraction of complex exponential terms, we can approximate the residue $\tilde{G}^r_n(k_\rho)$ in the t-domain as

$$\tilde{G}^r_{n_{approx}}(k_\rho) = \sum_{l=1}^{N_2} c^t_l \exp(d^t_l t) \tag{3.8}$$

Finally the residue in the k_{zs}-domain can be expressed as [32]

$$\tilde{G}^{r}_{n_{approx}}(k_{zs}) = \sum_{l=1}^{N_2} c_l^{k_{zs}} \exp(d_l^{k_{zs}} k_{zs}) \tag{3.9}$$

where

$$d_l^{k_{zs}} = -\frac{d_l^t T_2}{k_s(1+jT_2)} \tag{3.10}$$

$$c_l^{k_{zs}} = c_l^t \exp(-k_s d_l^{k_{zs}}) \tag{3.11}$$

Final Solution

Now, if we collect all the complex exponentials terms found in both steps, it will be a good approximation to $\tilde{G}_n(k_{zs})$ over both $C^1_{k_\rho}$ and $C^2_{k_\rho}$. Hence, an alternative expression for $\tilde{G}_n(k_{zs})$ would be

$$\begin{aligned}\tilde{G}_n(k_{zs}) &\simeq \tilde{G}^{r}_{n_{approx}}(k_{zs}) + \tilde{G}^{1}_{n_{approx}}(k_{zs}) \\ &= \sum_{l=1}^{N_2} c_l^{k_{zs}} \exp(d_l^{k_{zs}} k_{zs}) + \sum_{l=1}^{N_1} a_l^{k_{zs}} \exp(b_l^{k_{zs}} k_{zs}) \end{aligned} \tag{3.12}$$

In addition, the relationship between the spatial GF and the spectral GF in the k_ρ-domain can be written as

$$G(z,\rho) = \frac{1}{2}\int_{SIP} H_0^2(k_\rho \rho)\tilde{G}(k_\rho) k_\rho dk_\rho \tag{3.13}$$

where

$\tilde{G}(k_\rho)$ is the spectral Green's function,

$G(z,\rho)$ is the corresponding spatial Green's function,

$H_0^2(k_\rho \rho)$ is the Hankel function of second kind and zeroth order and

$\int_{SIP}$ denotes that the integration is performed along the Sommerfeld integration path (SIP).

Finally, substituting (3.12) for $\tilde{G}_n(k_\rho)$ in (3.2) and noting the relations $k_\rho^2 = k_s^2 - k_{zs}^2$, an alternative expression for $\tilde{G}(k_\rho)$ is found.

$$\tilde{G}(k_\rho) = \frac{1}{2jk_{zs}}\left(\sum_{l=1}^{N_2} c_l^{k_{zs}} \exp(d_l^{k_{zs}} k_{zs}) + \sum_{l=1}^{N_1} a_l^{k_{zs}} \exp(b_l^{k_{zs}} k_{zs})\right) \tag{3.14}$$

Then setting this expression into (3.13) leads to

$$G(z,\rho) = \frac{1}{2}\int_{SIP} H_0^2(k_\rho \rho)\frac{1}{2jk_{zs}}\left(\sum_{l=1}^{N_2} c_l^{k_{zs}} \exp(d_l^{k_{zs}} k_{zs}) + \sum_{l=1}^{N_1} a_l^{k_{zs}} \exp(b_l^{k_{zs}} k_{zs})\right) k_\rho dk_\rho \tag{3.15}$$

Interchanging the integration and summation operators,

$$\begin{aligned} G(z,\rho) &= c_l^{k_{zs}} \sum_{l=1}^{N_2} \frac{1}{2} \int_{SIP} H_0^2(k_\rho \rho) \frac{\exp(d_l^{k_{zs}} k_{zs})}{2jk_{zs}} k_\rho dk_\rho \\ &+ a_l^{k_{zs}} \sum_{l=1}^{N_1} \frac{1}{2} \int_{SIP} H_0^2(k_\rho \rho) \frac{\exp(b_l^{k_{zs}} k_{zs})}{2jk_{zs}} k_\rho dk_\rho \end{aligned} \tag{3.16}$$

Now we compare each term at the right hand side of (3.16) with the Sommerfeld identity (SI) given as [11]

$$\frac{\exp(-jkr)}{r} = \int_{SIP} H_0^2(k_\rho \rho) \frac{\exp(-jk_z |z|)}{2jk_z} k_\rho dk_\rho \tag{3.17}$$

where

k is the propagation constant in the media,

k_z is the z-directed component of k,

k_ρ is the radial component of k,

$r = \sqrt{\rho^2 + z^2}$ where ρ and z are spatial cylindrical coordinates,

$H_0^2(k_\rho \rho)$ is the zeroth-order Hankel function of the second kind and

SIP is the Sommerfeld integration path defined in chapter 2.

Applying the Sommerfeld identity term wise, the final expression for the spatial GF can be written in the following closed form:

$$G(z,\rho) = \sum_{l=1}^{N_2} c_l^{k_{zs}} \frac{\exp(-jk_s r_l^d)}{2r_l^d} + \sum_{l=1}^{N_1} a_l^{k_{zs}} \frac{\exp(-jk_s r_l^b)}{2r_l^b} \tag{3.18}$$

where

k_s is the propagation constant in the source medium,

$r_l^d = \sqrt{\rho^2 + (jd_l^{k_{zs}})^2}$ and

$r_l^b = \sqrt{\rho^2 + (jb_l^{k_{zs}})^2}$.

3.2.3 Methods for extracting exponential functions

3.2.4 Prony's method

Prony's method is a technique which models a set of discrete data as a linear combination of exponential functions. In other words it tries to fit a deterministic exponential model to the given data.

If we assume that the given discrete data $x(n)$ can be approximated by a sum of complex exponentials $\hat{x}(n)$

$$\hat{x}(n) = \sum_{k=1}^{p} h_k z_k^{n-1} \quad \text{for } n = 1, 2, .., N \tag{3.19}$$

where

$h_k = A_k \exp(j\theta_k)$,

$z_k = \exp[(\alpha_k + j2\pi f_k)T]$,

A_k is the amplitude of the complex exponential,

θ_k is the initial phase,

f_k is the frequency of the exponential function,

α_k is damping factor,

T is the sampling interval and

p is the number of exponential functions.

The error due to the approximation is

$$\epsilon(n) = |x(n) - \hat{x}(n)| = \left| x(n) - \sum_{k=1}^{p} h_k z_k^{n-1} \right| \tag{3.20}$$

The corresponding mean square error is then expressed as

$$\rho_\epsilon = \sum_{n=1}^{N} |\epsilon(n)|^2 \tag{3.21}$$

The straightforward method to find the least square estimator (LSE) for $\hat{x}$ is to minimize ρ_ϵ with respect to all the parameters; A_k, θ_k, α_k and f_k. This is a difficult nonlinear problem even when the value of p is known. Gaspard Riche, Baron de Prony introduced a method to eliminate this multidimensional nonlinear minimization by including the nonlinearity of the exponential model in a polynomial factoring [33]. For this purpose, reasonably fast algorithms are available. The Prony's method was first introduced to fit a given data sequence exactly. It implies that the number of data samples is equal to the number of unknown parameters. This constraint was later removed. In the sequel, we shall briefly present the original Prony's approach and the main features of its successors.

Original Prony's Method

Since $2p$ complex samples $x(1)$,$x(2)$, ..., $x(2p)$ are required to fit the $2p$ complex parameters of the exponential model exactly, we write (3.19) as

$$x(n) = \sum_{k=1}^{p} h_k z_k^{n-1} \quad \text{for } n = 1, 2, 3, ..., p \tag{3.22}$$

Here, $\hat{x}(n)$ has already been replaced by $x(n)$ because exactly $2p$ complex samples of $x(n)$ are used to fit an exact exponential model to the $2p$ complex parameters of h_k and z_k. The equation (3.22) can be expressed in matrix form.

$$ZH = X \tag{3.23}$$

where

$$Z = \begin{bmatrix} z_1^0 & z_2^0 & \cdots & z_p^0 \\ z_1^1 & z_2^1 & \cdots & z_p^1 \\ \vdots & \vdots & & \vdots \\ z_1^{p-1} & z_2^{p-1} & \vdots & z_p^{p-1} \end{bmatrix} \tag{3.24}$$

$$H = \begin{bmatrix} h_1 \\ h_2 \\ \vdots \\ h_p \end{bmatrix} \tag{3.25}$$

$$X = \begin{bmatrix} x(1) \\ x(2) \\ \vdots \\ x(p) \end{bmatrix} \tag{3.26}$$

The matrix Z has a Vandermonde structure [34]. Prony suggested an ingenious method to find the matrix Z separately. After Z is calculated, the resulting set of linear equations are solved for the unknown vector H.

The key to the separation is to recognize that (3.22) is the solution to some homogeneous linear constant-coefficient difference equation. In order to find this difference equation, we proceed as follows. Let us define the polynomial $\phi(z)$ having roots z_k for $k = 1, 2, 3, ..., p$.

$$\phi(z) = \prod_{k=1}^{p} (z - z_k) \tag{3.27}$$

Expanding (3.27) into a power series

$$\phi(z) = \sum_{m=0}^{p} a(m) z^{p-m} \tag{3.28}$$

where $a(m)$ are in general complex constants and $a(0)$ is normalized to one, i.e. $a(0) = 1$. After some elementary operations it can be shown [35] that

$$\sum_{m=0}^{p} a(m) x(n-m) = \sum_{i=1}^{p} h_i z_i^{n-p-1} \sum_{m=0}^{p} a(m) z_i^{p-m} = 0 \tag{3.29}$$

Now it is obvious that (3.29) is the linear difference equation whose homogeneous solution is given by (3.27). Moreover the polynomial (3.28) is the characteristic equation associated with this linear difference equation [35].

Evaluating (3.29) for $n = (p+1), \ldots, 2p$ and expressing the results in matrix form

$$\begin{bmatrix} x(p) & x(p-1) & \cdots & x(1) \\ x(p+1) & x(p) & \cdots & x(2) \\ \vdots & \vdots & & \vdots \\ x(2p-1) & x(2p-2) & \vdots & x(p) \end{bmatrix} \begin{bmatrix} a(1) \\ a(2) \\ \vdots \\ a(p) \end{bmatrix} = \begin{bmatrix} x(p+1) \\ x(p+2) \\ \vdots \\ x(2p) \end{bmatrix} \tag{3.30}$$

Using the above formulations, we can now summarize Prony's original method as follows:

Step one Polynomial coefficients $a(m)$ are found solving (3.30).

Step two Roots z_k of the polynomial (3.28) are found.

Step three These roots are used to complete the matrix Z in (3.23) and then vector H is found solving (3.23).

We have now presented the basic Prony's method. It was later modified to include more data samples. This corresponds to the overdetermined case and is known as the least square Prony's method (LSPM). In addition to LSPM, other improved versions like total least square Prony's method and SVD (Singular Value Decomposition) Prony's method [36] are commonly used in signal processing applications.

3.2.5 Generalized pencil-of-functions method

The GPOF method is relatively new even if its roots go back to the pencil-of-functions (POF) approach [37], which is a remote successor of Prony's method. The GPOF is more computationally efficient and is presented as an one-step-procedure in extracting the complex exponentials as opposed to the POF method, which is a two-step procedure [38].

Assume that a discrete data sequence $x(n)$ is expressed as

$$x(n) = \sum_{k=1}^{M} b_k \exp(s_k \delta t n) \quad \text{for } n = 0, 1, \ldots, N-1 \tag{3.31}$$

where

M is the number of exponential function used to approximate data samples $x(n)$,

b_k are the complex amplitudes,

s_k are the complex poles and

δt is the sampling interval.

Introducing $z_k = \exp(s_k \delta t)$, (3.31) can be written

$$x(n) = \sum_{k=1}^{M} b_k \, z_k^n \tag{3.32}$$

We also introduce the following set of data vectors

$$\mathbf{y}_i = [x(i), x(i+1), \dots, x(i+N-L-1)]^T \quad \text{for } i = 0, 1, ..., L \tag{3.33}$$

Here the superscript T denotes the transpose of a matrix or a vector and L is chosen to be $M \leq L \leq N - M$. In terms of the above defined vectors $\mathbf{y}_i$, the following submatrices are built:

$$\begin{array}{rcl} Y_1 & = & [\mathbf{y}_0, \mathbf{y}_1, \dots, \mathbf{y}_{L-1}] \\ Y_2 & = & [\mathbf{y}_1, \mathbf{y}_2, \dots, \mathbf{y}_L] \end{array} \tag{3.34}$$

They can alternatively be expressed in the matrix form

$$\begin{array}{rcl} Y_1 & = & Z_1 B Z_2 \\ Y_2 & = & Z_1 B Z_0 Z_2 \end{array} \tag{3.35}$$

where

$$Z_1 = \begin{bmatrix} 1 & 1 & \cdots & 1 \\ z_1 & z_2 & \cdots & z_M \\ \vdots & \vdots & & \vdots \\ z_1^{N-L-1} & z_2^{N-L-1} & \vdots & z_M^{N-L-1} \end{bmatrix} \tag{3.36}$$

$$Z_2 = \begin{bmatrix} 1 & z_1 & \cdots & z_1^{L-1} \\ 1 & z_2 & \cdots & z_2^{L-1} \\ \vdots & \vdots & & \vdots \\ 1 & z_M & \vdots & z_M^{L-1} \end{bmatrix} \tag{3.37}$$

$$Z_0 = \begin{bmatrix} z_1 & 0 & \cdots & 0 \\ 0 & z_2 & \cdots & 0 \\ \vdots & \vdots & & \vdots \\ 0 & 0 & \vdots & z_M \end{bmatrix} = diag[z_1, z_2, \dots, z_M] \tag{3.38}$$

$$B = \begin{bmatrix} b_1 & 0 & \cdots & 0 \\ 0 & b_2 & \cdots & 0 \\ \vdots & \vdots & & \vdots \\ 0 & 0 & \vdots & b_M \end{bmatrix} = diag[b_1, b_2, \dots, b_M] \tag{3.39}$$

Now consider the matrix pencil $Y_2 - zY_1$ expressed as

$$Y_2 - zY_1 = [Z_1][B][Z_0 - zI][Z_2] \tag{3.40}$$

For an arbitrary z, the rank of $Y_2 - zY_1$ will be M, i.e. the number of exponential functions, provided that $M \leq L \leq N-M$. However, if $z = z_k$, for $k = 1, 2, ..., M$ the k th row of $[Z_0 - zI]$ is zero and the rank of this matrix is $M-1$. Namely, if $M \leq L \leq N-M$, $z = z_k$ is a rank-reducing number of $Y_2 - zY_1$. Hence, the parameters z_k may be seen as the generalized eigenvalues of the matrix pair Y_2 and Y_1. Equivalently the problem of solving for z_k can be cast as an ordinary eigenvalue problem

$$Y_1^+ Y_2 - zI = 0 \tag{3.41}$$

where Y_1^+ is the Moore-Penrose pseudoinverse of Y_1 and is defined as [36]

$$Y_1^+ = (Y_1^H Y_1)^{-1} Y_1^H \tag{3.42}$$

Here, the superscripts -1, $+$ and H denote the standard matrix inverse, pseudoinverse and complex conjugate (Hermitian) transpose, respectively. We have also assumed that $(Y_1^H Y_1)^{-1}$ exists.

In the case of noiseless data samples $x(n)$, the rank of matrix Y_1 can with no loss of generality be assumed to be M. Using the singular value decomposition (SVD) of Y_1

$$Y_1 = UDV^H \tag{3.43}$$

where

$U = [u_1, , u_M]$ is an unitary matrix whose columns are eigenvectors of $Y_1 Y_1^H$,

$D = [\sigma_1, , \sigma_M]$ is a diagonal matrix whose diagonal elements are singular values (i.e. the square roots of the nonzero eigenvalues) of both $Y_1 Y_1^H$ and $Y_1^H Y_1$ and

$V = [v_1, , v_M]$ is an unitary matrix whose columns are eigenvectors of $Y_1^H Y_1$.

Then, the pseudoinverse of Y_1 defined in (3.42) can alternatively be expressed as

$$Y_1^+ = VD^{-1}U^H \tag{3.44}$$

Although it is correct to assume that the number of non-zero singular values of Y_1 is equal to M in the case of noiseless data samples, for a general data set the number of non-zero singular values is in fact equal to the minimum of the dimensions of Y_1, i.e. the minimum of $N-L$ and L. Let us denote this value by P. Then the corresponding diagonal matrix D would be P *by* P in dimension. When the samples are noiseless, M diagonal elements of D will be non-zero and the rest of $P-M$ elements will be zero. However, in the case of noisy data, either due to inherent inaccuracies in the given data values or the round-off errors generated during digitization procedure, all the P singular values may be non-zero. Nevertheless, out of these P singular values only M elements will be significant. As an attempt to separate the data from the noise, we shall only use those significant singular values corresponding to noiseless data. Then Y_1^+ given in (3.44) can in practice be considered as the truncated pseudoinverse defined based on the most significant singular values and corresponding singular vectors in V and U respectively.

Then following the relationship between the eigenvectors and eigenvalues, we can write

$$Y_1^+ Y_2 \rho_k = z_k \rho_k \tag{3.45}$$

where

z_k is the eigenvalues of $Y_1^+ Y_2$ and

ρ_k is the corresponding eigenvectors $Y_1^+ Y_2$.

The significant eigenvalues z_k for $k = 1, 2, ..., M$ can be acquired with the help of a well-known algorithm like QZ algorithm [39]. Once z_k are known, their corresponding amplitudes b_k in (3.31) are found by solving (3.46) in the least square sense for b_k.

$$ZB_0 = X_0 \tag{3.46}$$

where

$$Z = \begin{bmatrix} 1 & 1 & \cdots & 1 \\ z_1 & z_2 & \cdots & z_M \\ \vdots & \vdots & & \vdots \\ z_1^{N-1} & z_2^{N-1} & \vdots & z_M^{N-1} \end{bmatrix} \tag{3.47}$$

$$B_0 = \begin{bmatrix} b_1 \\ b_2 \\ \vdots \\ b_M \end{bmatrix} \tag{3.48}$$

$$X_0 = \begin{bmatrix} x(0) \\ x(1) \\ \vdots \\ x(N-1) \end{bmatrix} \tag{3.49}$$

One can now express the least square solution of (3.46) in terms of the pseudoinverse of matrix Z, Z^+.

$$B_0 = Z^+ X_0 = (Z^H Z)^{-1} Z^H X_0 \tag{3.50}$$

This completes the introduction of the GPOF method for extracting complex exponential terms from a given discrete data sequence. One should notice that this method resembles the other eigenvalue based methods like the ESPRIT algorithm popular in signal processing applications [36].

3.2.6 Prony's method vs GPOF method

The major drawback of the original PM is its sensitivity to additive noise. The presence of additive noise degrades the performance of the original PM significantly. Even though this weakness is somewhat improved in the descenders of the original PM, their performance is still poorer than the alternative methods like GPOF.

In addition, the original PM can not take care of the dynamic nature of GFs due to the limited number of data samples allowed. However, the least square PM is able to supply the required dynamic range using all the data samples available. One other limitation of

PM is that it assumes that the number of exponential functions are known in advance. This is not realistic in practice. Moreover, it is difficult to introduce some systematic procedure into PM such that the number of exponential functions can be selected logically, especially in the presence of noise [40].

The GPOF method is less restrictive than some versions of PM because it does not require that all system poles are either stable or nonstable. Moreover, the GPOF is computationally more efficient because it does not solve an L th degree polynomial [38]. After all, the most distinguished feature of the GPOF method is that it introduces a methodical way of combating noise.

3.3 On the Implementation of DCIM

We have implemented the robust version of DCIM for transforming the spectral GF into the spatial GF. We have followed the above mentioned approach with some self-explanatory modifications. These modifications are necessary to eliminate the numerical instabilities and to secure an efficient implementation.

Although the number of exponential functions is determined on the basis of the most significant singular values of the data matrices as explained in section 3.2.5, in an approximating procedure filled with small numerical inaccuracies it is difficult to pick the significant singular values in a decisive manner due to small variations among the singular values. Therefore, we select the largest singular values such that the relative error of the approximated spectral GF, compared with the original spectral GF, is less than a pre-defined threshold. This method improves the stability of algorithms by avoiding the insignificant singular values.

3.4 Exact vs Approximated Spatial Green's Functions

We shall now compare the spatial GF obtained by DCIM and the exact spatial GF. The exact spatial GF is calculated following the methods presented in chapter 2. The scalar Green's function is calculated for a dielectric layer over an ideal ground plane (Fig. 4.1). The relative dielectric coefficient ε_r and the thickness of the dielectric material are 12.6 and 1 mm, respectively. The operating frequency is fixed at 10 GHz. Both the source point and the field point are assumed to be on the top surface of the dielectric layer.

The corresponding spectral GF, when evaluated along the integration path defined by (3.1), is shown in Fig. 3.4. Figures 3.5 and 3.6 illustrate the dynamic part and static part respectively. Following the quasi-static image extraction performed in step one, Fig. 3.7 compares the static part with the quasi-static image approximation. They are almost identical. Moreover, the corresponding image approximation performed on the residue remained after quasi-static image extraction, agrees well with the actual residue (Fig. 3.8).

Finally, Fig. 3.9 and 3.10 compare the exact spatial scalar Green's function with the respective quantities obtained by DCIM. The differences are virtually unnoticed. Other

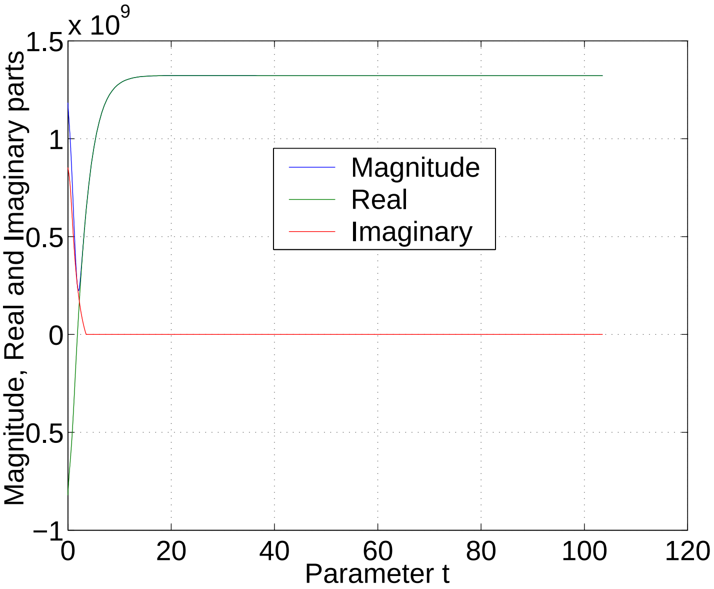

Fig. 3.4: *Spectral Green's function including both static part (over $C^1_{k_\rho}$) and dynamic part (over $C^2_{k_\rho}$)*

structures are also examined to confirm the accuracy of DCIM in approximating GFs. In general a very good agreement is observed. Therefore we can safely replace the exact spatial GF by the current approximated spatial GF without compromising the accuracy.

3.5 Comments on Numerical Stability and Convergence

If the guidelines mentioned above are followed the method can be implemented in software with good numerical stability and convergence. Therefore DCIM gives the spatial GF which is in good agreement with the corresponding so-called exact GF obtained by means of numerical integrations and other convergence-accelerated methods. It is also noticed that this agreement is restricted mainly to the near- and intermediate regions. The far-field results may be somewhat unstable, especially when the far-fields are dominated by the surface waves. The deviations of approximated spatial far-field are prominent when the source is situated in a bounded layer and the observation point is in an unbounded layer. In the original version of the robust DCIM [29], stratified media are handled by approximating the spectral GFs with exponential terms, which are functions of the electrical parameters of the source layer. In [31], it is shown that a better convergence is obtained if this approximation is done in terms of unbounded media parameters. Doing so, one can avoid the introduction of new branch cuts into the existing spectral GF. Otherwise, the introduction of new branch cuts may complicate the extraction of exponential terms in the subsequent stages.

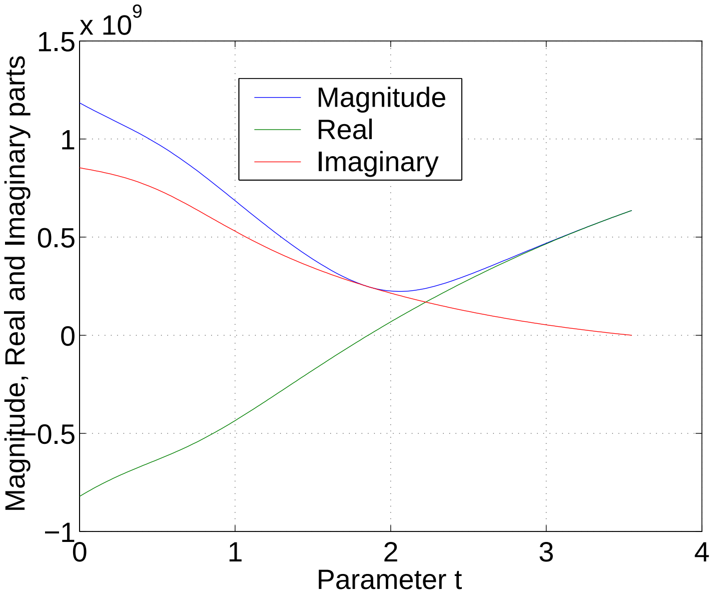

Fig. 3.5: *Spectral Green's function closer to branch point and surface wave pole, dynamic part (over $C^2_{k_\rho}$)*

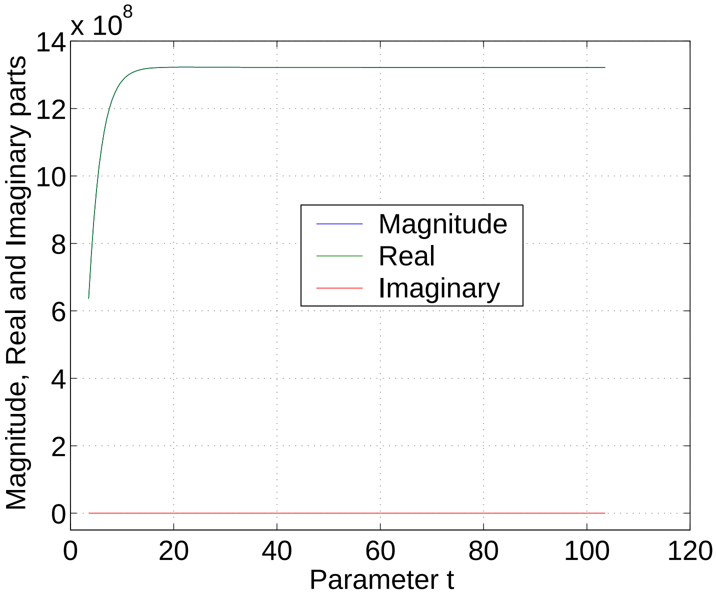

Fig. 3.6: *Spectral Green's function away from branch cut and surface wave pole, static part (over $C^1_{k_\rho}$)*

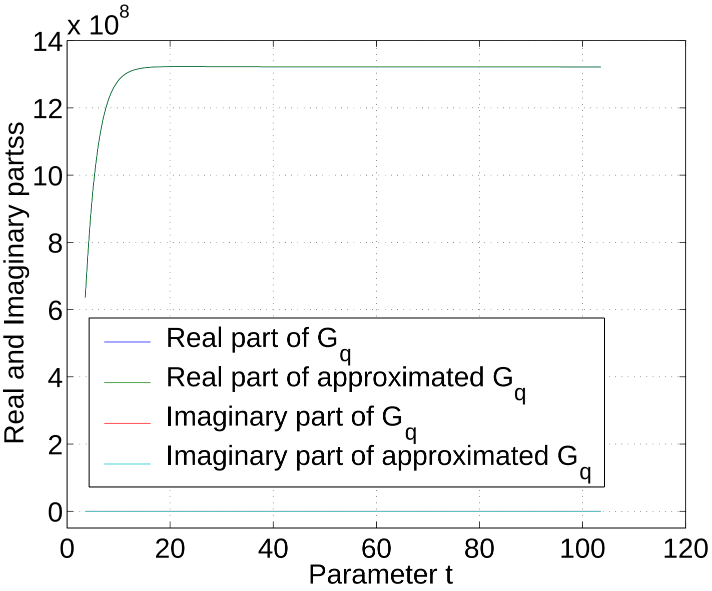

Fig. 3.7: *Static part of the spectral Green's function compared with its approximation (quasi-static approximation)*

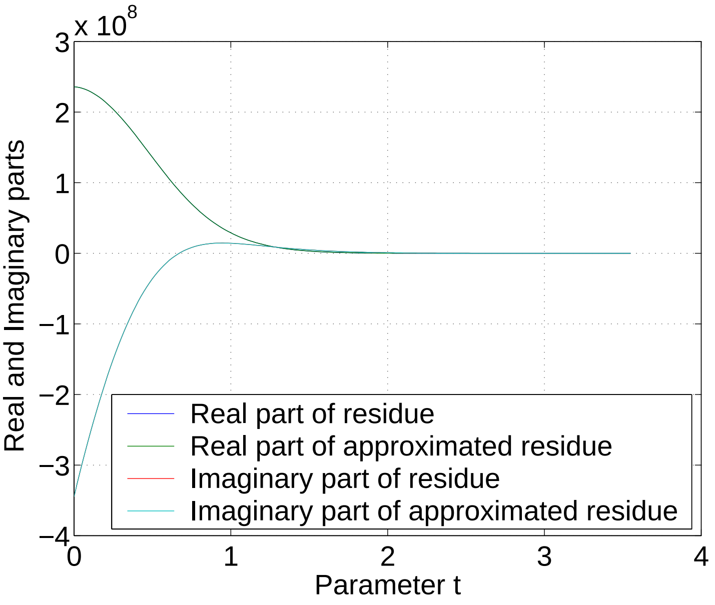

Fig. 3.8: *Residue of the dynamic part of the spectral Green's function compared with its approximation*

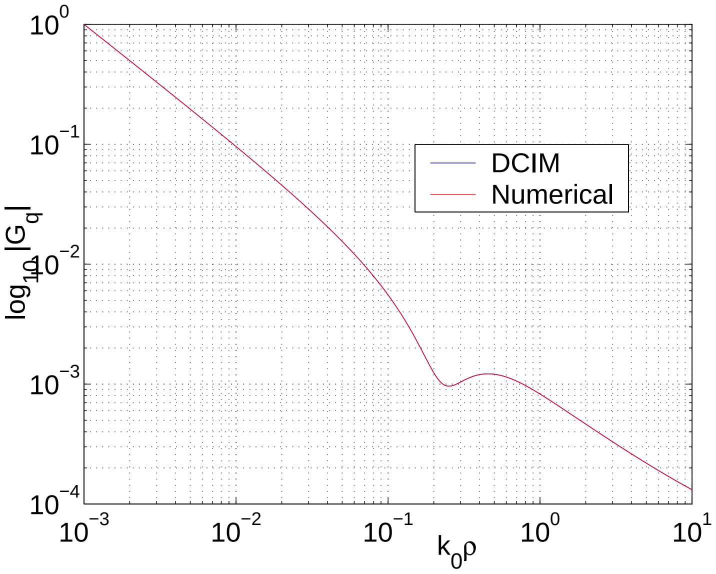

Fig. 3.9: *Magnitude of the spatial scalar Green's function*

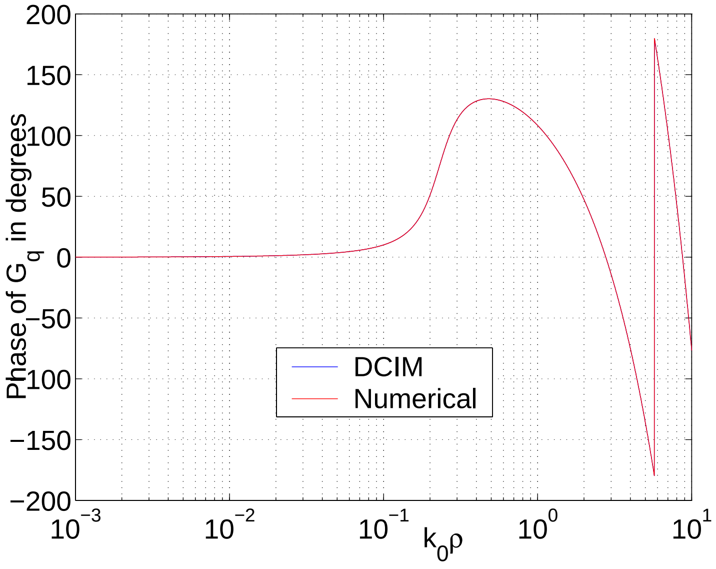

Fig. 3.10: *Phase of the spatial scalar Green's function*

3.6 Advantages and Limitations of Robust-DCIM

The present version of DCIM eliminates the cumbersome trade-off between the parameters and the sampling frequency in the original DCIM. Instead, two different sampling frequencies that match the dynamic behavior of the spectral GFs are now selected. Nevertheless, the number of parameters to be chosen have increased compared to the basic approach. But they are to be determined once, based on the geometries and the electrical constants. The same parameters are then applied to find the different components of the dyadic GF.

Chapter 4

Method of Moments

4.1 Introduction

Due to the revolutionary advances in digital computers, more and more emphasis is given to accurate numerical solutions of electromagnetic problems. Thereby, engineers are able to avoid rather mathematically complex analytical approaches. Even though the numerical approach does not in general give the exact solution, extremely fast and high capacity computers have been able to solve the corresponding numerical formulation with such an accuracy that the inherent approximate nature of the numerical solutions has been faded away. In some context, these solutions have already been referred to as the exact solution due to the fact that the analytical, in other word the truly exact solution either does not exist in closed form or is too tedious to be evaluated.

Therefore the need arises to reformulate the functional equations, which naturally result from integral equations, into a numerically convenient form. The technique called method of moments (MoM) has been effective in this process [41]. The application of MoM to functional equations results in a matrix equation, which can be solved by applying known methods of matrix inversion. In this chapter, we shall present MoM for solving electromagnetic problems encountered in planar stratified media.

4.2 General Formulation

Let us assume the relationship

$$\mathcal{L}y = f \tag{4.1}$$

where

$\mathcal{L}$ is the known linear operator,

f is the known excitation function and

y is the unknown response function.

Then, the method of moments (MoM) would be a viable, or probably the most numerically efficient, way of determining y. In electromagnetic propagation, the linear operator $\mathcal{L}$ often represents an integrodifferential operator. MoM begins with expanding the function y as a linear combination of N terms y_n.

$$y = \sum_{n=1}^{N} a_n y_n \tag{4.2}$$

where

a_n are unknown constants to be determined and

y_n are user-selected functions, which are often referred to as *basis* or *expansion* functions. Their domains are the same as that of y.

For a finite N and a general y the equality given in (4.2) is not always true, and in fact it can only be considered as an approximation. However for large N, (4.2) can be considered as an equality. Now, substituting (4.2) into (4.1) and exploiting the linearity of the operator $\mathcal{L}$, one obtains

$$\sum_{n=1}^{N} a_n \mathcal{L} y_n = f \tag{4.3}$$

It is now obvious that the selection of y_n should be done in such a way that each $\mathcal{L}y_n$ term can be evaluated conveniently, preferably in closed form. Since (4.3) represents a relationship consisting of N unknowns, solving it requires N linearly independent equations. This can be accomplished by evaluating and weighting (4.3) at N distinct points or regions. Such an operation implicitly imposes the given boundary condition as a weighted average. To perform this operation easily, an inner product operator $\langle w, g\rangle$ between two arbitrary functions w and g is defined. By definition it satisfies the following axioms.

$$\begin{array}{ccccc} \langle w, g\rangle & = & \langle g, w\rangle^* & & \\ \langle w_1 + w_2, g\rangle & = & \langle w_1, g\rangle + \langle w_2, g\rangle & & \\ \langle aw, g\rangle & = & a\ \langle w, g\rangle & & \\ \langle g, g\rangle & > & 0 & if & g \neq 0 \\ \langle g, g\rangle & = & 0 & if & g = 0 \end{array} \tag{4.4}$$

Here a is a scalar and the superscript * indicates complex conjugation.

For example, a common inner product operator can be defined as

$$\langle w, g\rangle = \iint_S w^* \cdot g \, ds \tag{4.5}$$

where

w is called a *testing* (*weighting*) function

g is the function being tested (or weighted) and

S denotes the domain of the functions w and g.

Defining a set of N testing functions $\{w_m\} = w_1, w_2, ..., w_N$ in the domain of the operator $\mathcal{L}$ and exploiting the properties (4.4), the relationship (4.3) can be weighted to give.

$$\textstyle\sum_{n=1}^{N} a_n \langle w_m, \mathcal{L}y_n \rangle = \langle w_m, f \rangle \qquad m = 1, 2, ..., N \tag{4.6}$$

This can be expressed in matrix form

$$[\mathcal{L}_{mn}]\,[a_n] = [f_m] \tag{4.7}$$

where

$$[a_n] = \begin{bmatrix} a_1 \\ a_2 \\ \vdots \\ a_N \end{bmatrix} \tag{4.8}$$

$$[f_m] = \begin{bmatrix} f_1 \\ f_2 \\ \vdots \\ f_N \end{bmatrix} = \begin{bmatrix} \langle w_1, f \rangle \\ \langle w_2, f \rangle \\ \vdots \\ \langle w_N, f \rangle \end{bmatrix} \tag{4.9}$$

$$[\mathcal{L}_{mn}] = \begin{bmatrix} \langle w_1, \mathcal{L}y_1 \rangle & \langle w_1, \mathcal{L}y_2 \rangle & \cdots & \cdots & \langle w_1, \mathcal{L}y_N \rangle \\ \langle w_2, \mathcal{L}y_1 \rangle & \langle w_2, \mathcal{L}y_2 \rangle & \cdots & \cdots & \langle w_2, \mathcal{L}y_N \rangle \\ \vdots & \vdots & & & \vdots \\ \vdots & \vdots & & & \vdots \\ \langle w_N, \mathcal{L}y_1 \rangle & \langle w_N, \mathcal{L}y_2 \rangle & \cdots & \cdots & \langle w_N, \mathcal{L}y_N \rangle \end{bmatrix} \tag{4.10}$$

The equation (4.7) can now be solved by matrix inversion.

$$[a_n] = [\mathcal{L}_{mn}]^{-1}\,[f_m] \tag{4.11}$$

4.3 Basis and Testing Functions

The basis and testing functions are divided into two general classes:

1. Entire domain functions that exist over the entire domain of y
2. Subdomain functions, which, as implied by the name, are non-zero only within a part of the domain of y

4.3.1 Entire domain functions

The main advantage of entire domain basis functions occurs in problems whose unknown function y can be assumed a priori known distribution. Then the entire domain functions may render an acceptable representation of the unknown y using far fewer terms in the expansion of (4.2) than using subdomain functions. However, since the number of functions (or modes) are finite, entire domain functions are usually not capable of modeling either arbitrary or complicated unknowns.

4.3.2 Subdomain functions

The distinct advantage of subdomain functions over entire domain functions is that they may be used without any prior knowledge of the nature of the unknown function y. When defining a set of subdomain functions, they can be selected as either uniform or non-uniform, collinear or non-collinear, overlapping or non-overlapping, limited only by the resulting complexity [42].

4.3.3 Galerkin's method

In general, the basis functions and the testing functions are selected in such a way that the resulting equations (4.6) are linearly independent and, at the same time the computational complexity associated with the inner product evaluations is minimized. One particular choice of these functions may let both basis and testing functions be the same, that is, $w_m = y_n$. This special procedure is known as *Galerkin's method.* The prevalent usage of Galerkin's method in direct MoM can be attributed to its numerical advantages. When Galerkin's method is combined with inner product, real-valued basis functions preserve both reciprocity and conservation of energy [43]. In addition, since in this method both basis and testing functions are defined over the same domain, it is possible to either exchange the integral signs, to integrate by parts or to manipulate the integrals as they are. Such techniques are often used to reduce the degree of singularity of the resulting integrands [43].

4.4 Application of MoM to Stratified Media

The mixed potential integral equations in chapter 2 provide the desired linear relationship for determining induced current densities on an arbitrary metalization submerged in a stratified medium (Fig. 4.1). This sort of formulation is very common in analyzing antennas consisting of microstrip lines and microstrip patches on multi layer dielectric structures. Since the Green's function formulations can be done in either space or spectral domain, the corresponding MoM formulation can also be either in space or spectral domain. We shall now have a closer look on space domain MoM.

4.4.1 Space domain method of moments

Based on the mixed potential integral formulation described in subsection 2.4.6 the electric field can be expressed in terms of vector potential $G_{\mathbf{A}}$ and scalar potential G_q.

$$E_x = -j\omega G^A_{xx} * J_x + \frac{1}{j\omega}\frac{\partial}{\partial x}(G_q * \nabla \cdot J) \tag{4.12}$$

$$E_y = -j\omega G^A_{yy} * J_y + \frac{1}{j\omega}\frac{\partial}{\partial y}(G_q * \nabla \cdot J) \tag{4.13}$$

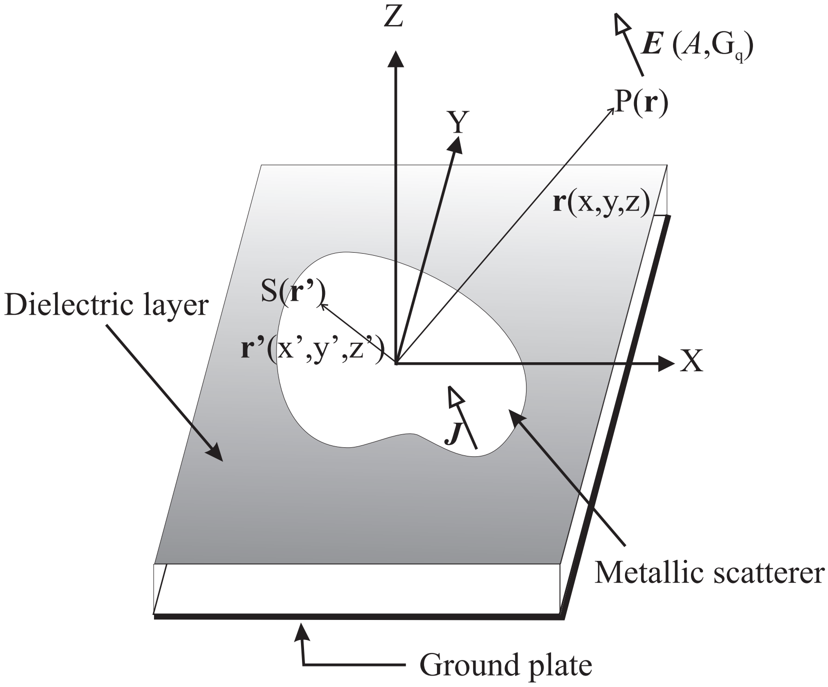

Fig. 4.1: *Simple planar metallic structure on a grounded substrate*

where * denotes linear convolution. G_{aa}^{A} represents the a-directed vector potential due to an a-directed electric dipole of unit dipole moment, while G_q represents the scalar potential produced by a unit point charge associated with a horizontal electric dipole (HED).

We express the surface current density on the patch as a linear combination of x- and y-directed sub-domain functions. Rectangular rooftop functions, as shown in Fig. 4.2, are selected following the theoretical and practical considerations given in section 4.4.2. Therefore, x- and y-directed induced surface current densities can be expressed as

$$J_x(x,y) = \sum_n \sum_m I_x^{nm} J_x^{nm}(x,y) \tag{4.14}$$

$$J_y(x,y) = \sum_n \sum_m I_y^{nm} J_y^{nm}(x,y) \tag{4.15}$$

where $J_x^{nm}(x,y)$ and $J_y^{nm}(x,y)$ are the rooftops in x and y directions, respectively. I_x^{nm} and I_y^{nm} are all unknown coefficients that have to be determined. After substituting (4.14) and (4.15) into (4.12) and (4.13), and imposing the boundary conditions on the perfectly conducting planar scatterer where the total tangential electrical field vanishes, Galerkin's procedure leads to the matrix equation

$$ZI = V \tag{4.16}$$

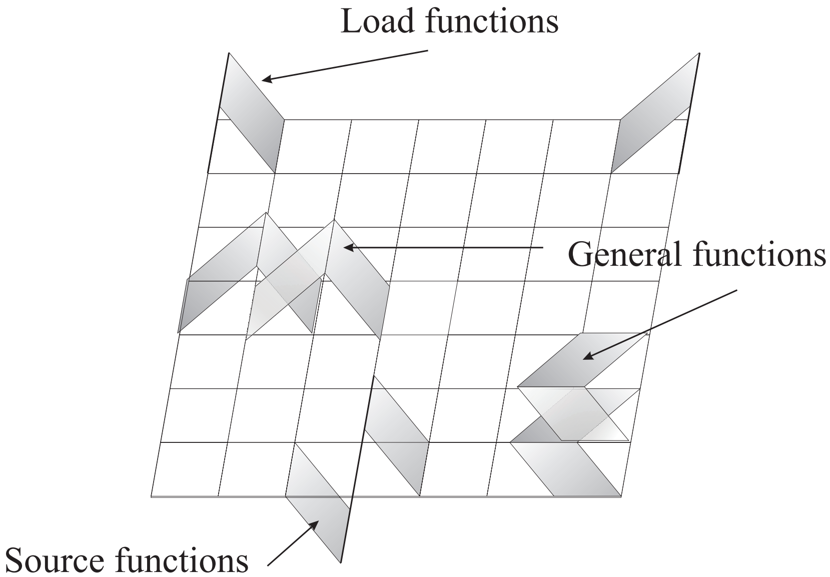

Fig. 4.2: *Basis functions representing the current densities within a metallic plate, at the source and at the load*

$$\begin{bmatrix} Z_{xx}^{n\,m,n'\,m'} & Z_{xy}^{n\,m,n'\,m'} \\ Z_{yx}^{n\,m,n'\,m'} & Z_{yy}^{n\,m,n'\,m'} \end{bmatrix} \begin{bmatrix} I_x^{n'\,m'} \\ I_y^{n'\,m'} \end{bmatrix} = \begin{bmatrix} V_x^{n\,m} \\ V_y^{n\,m} \end{bmatrix} \tag{4.17}$$

where

$$\begin{aligned} Z_{aa}^{p\,q,\,p'q'} &= \left\langle J_a^{p\,q}, G_{aa}^{A} * J_a^{p'\,q'} \right\rangle \\ &\quad -\frac{1}{\omega^2}\left\langle \frac{\partial}{\partial a} J_a^{p\,q}, G_q * \frac{\partial}{\partial a} J_a^{p'\,q'} \right\rangle \end{aligned} \tag{4.18}$$

$$Z_{ab}^{p\,q,\,p'q'} = -\frac{1}{\omega^2}\left\langle \frac{\partial}{\partial a} J_a^{p\,q}, G_q * \frac{\partial}{\partial b} J_b^{p'\,q'} \right\rangle \tag{4.19}$$

$Z_{ab}^{p\,q,p'\,q'}$ denotes the mutual impedance coefficient between the (p, q) th testing function and the (p', q') th basis function,

$*$ denotes the linear convolution defined in (2.38) in chapter 2,

$\langle\rangle$ is the inner product defined in (4.5),

a and b stand for either x or y,

$V_a^{p\,q}$ is the weighted excitation which is an external incident electric field and

$J_a^{p\,q}$ and $J_a^{p'\,q'}$ denote testing and basis functions, respectively.

4.4.2 Admissible class of basis and testing functions for MoM

In [44], [45] and [46], it has been concluded that the classes of functions from which the basis and testing functions are chosen must satisfy the following criteria :

- In the direction of the current, the sum of the order of the differentiability of the basis and testing functions must be equal to or greater than one
- In the orthogonal direction of the current, any piecewise continuous functions or functions with singularities of the order of less than one are admissible.

In addition, it is sometimes essential to use piecewise continuous basis functions with finite discontinuities in the direction of the differentiation, for the geometries that have junction or load connections in the domain of interest (Figure 4.2). If these piecewise continuous basis functions represent the currents at the load or the source terminals, which are on the same plane as the microstrip geometry under study, the impulse functions generated by the differentiation should not be included in the calculations, because the divergence of these current densities in (4.12) and (4.13) must be finite at these junctions. This is due to the continuity of the current at the junctions, which is equivalent to saying that discontinuity of the current in one direction must be equal to the negative of the discontinuity either in the same direction or in another direction. It is relatively easy to treat the discontinuous basis functions in the spatial domain MoM because the contribution of the surface charge density ($\nabla \cdot J$) can be isolated as given in (4.12) and (4.13).

4.4.3 Simplifying the elements in Z

In (4.18) and (4.19), we have already transferred the differential operator up to the testing functions. Following the approach taken in [47], we interchange the convolution operator and the inner product operator in each term of (4.18) and (4.19). After some algebraic manipulations, the first term in (4.18), for example, can be expressed in the form of

$$\left\langle J_a^{p\,q}, G_{aa}^A * J_a^{p'\,q'} \right\rangle = \iint du\,dv\; G_{aa}^A(u,v)\; J_a^{p\,q} \otimes J_a^{p'\,q'} \tag{4.20}$$

where

$f \otimes g$ denotes the cross-correlation function between the functions f and g. We define the 2D cross-correlation as follows :

$$f(u,v) \otimes g(u,v) = \iint dt\,ds\; f(t,s)\; g^*(t-u, s-v) \tag{4.21}$$

Here, g^* denotes the complex conjugate of g.

Since the basis and testing functions are analytical functions, their cross-correlation functions can in general be expressed as piecewise continuous functions. Hence the four-fold integral in (4.20) can be reduced to two-fold integral.

Figure 4.3 shows for example a resulting cross-correlation $J_x^{p\,q} \otimes J_x^{p\,q}$ when both basis and testing functions are assumed to be rectangular rooftop functions. There are certain

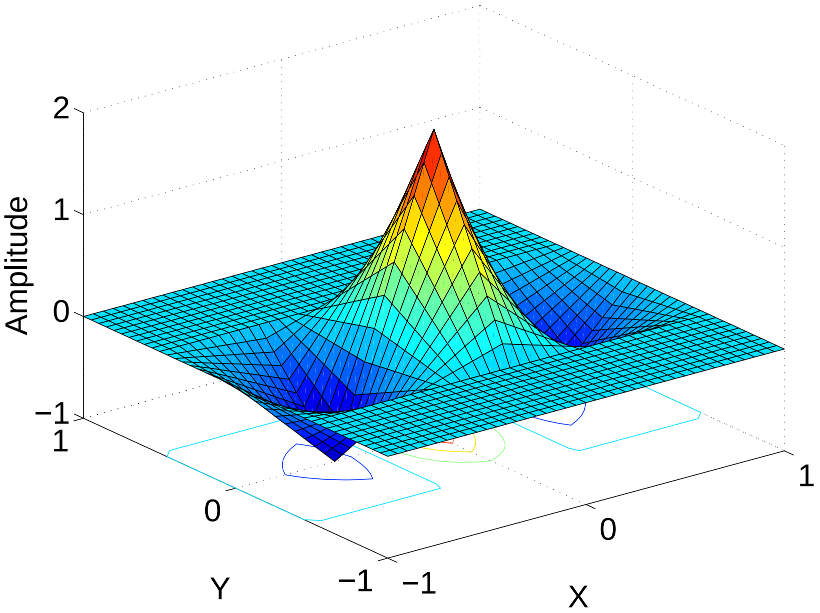

Fig. 4.3: *Example of a piecewise continuous cross-correlation function when both basis and testing functions are rooftop functions*

symmetries that exist within and among these cross-correlation terms. Moreover, they are separable in both x and y directions. All these properties of the cross-correlation terms can be exploited to reduce the computational complexity involved in calculating the impedance matrix Z.

Now, if we assume that the Green's functions $G^A_{aa}(u,v)$ are expressed as a sum of exponential terms (Section 3.2.2), it is apparent that each $Z^{p\,q,\,p'q'}_{ab}$ can be found by evaluating few two-dimensional generalized exponential integrals (2D-GEI) of the form

$$I = \iint\limits_{\Delta S} \frac{\exp(-jkr)}{r} f(x',y')dx'dy' \tag{4.22}$$

where

$$r = \sqrt{x'^2 + y'^2 + \alpha^2} \tag{4.23}$$

with α denoting a complex image and

$f(x',y')$ is a separable cross-correlation function in x' and y' coordinates, that is,

$$f(x',y') = g(x')h(y') \tag{4.24}$$

where $g(x')$ and $h(y')$ are polynomials in x' and y' respectively.

The numerical method introduced in section 5.2 evaluates these 2D-GEI efficiently.

4.4.4 Symmetries exist in impedance matrix Z

The space domain vector potential G_{aa}^{A} and scalar potential G_q are cylindrically symmetric (Section 2.8.1). Hence, when the planar structure is uniformly partitioned in both x- and y-directions, even with unequal partition length in x- and y-directions, the following implicit symmetries exist among the coefficients $Z_{ab}^{p\,q,\,p'q'}$ in (4.17) [48]. We can denote them as follows:

$$\begin{aligned} Z_{aa}^{p\,q,\,p'q'} &= Z_{aa}^{p'q',\,p\,q} \\ &= Z_{aa}^{p'q,\,p\,q'} \\ &= Z_{aa}^{p\,q',\,p'q} \end{aligned} \tag{4.25}$$

where a can be either x or y.

$$\begin{aligned} Z_{xy}^{p\,q,\,p'q'} &= -Z_{xy}^{p\,q',\,p'(q+1)} \\ &= -Z_{xy}^{(p'+1)\,q,\,p\,q'} \\ &= Z_{xy}^{(p'+1)\,q',\,p\,(q+1)} \end{aligned} \tag{4.26}$$

$$Z_{xy}^{p\,q,\,p'q'} = Z_{yx}^{p'\,q',\,p\,q} \tag{4.27}$$

In order to clarify how the above mentioned relationships are obtained, for example, let us start from (4.18) and obtain the relationship given in (4.25).

$$\begin{aligned} Z_{aa}^{p\,q,\,p'q'} &= Z_{aa}(p\,q,\,p'q') \\ &= \left\langle J_a^{p\,q}, G_{aa}^{A} * J_a^{p'\,q'} \right\rangle - \frac{1}{\omega^2} \left\langle \frac{\partial}{\partial a} J_a^{p\,q}, G_q * \frac{\partial}{\partial a} J_a^{p'\,q'} \right\rangle \\ &= \left\langle G_{aa}^{A}, J_a^{p\,q} \otimes J_a^{p'\,q'} \right\rangle - \frac{1}{\omega^2} \left\langle G_q, \frac{\partial}{\partial a} J_a^{p\,q} \otimes \frac{\partial}{\partial a} J_a^{p'\,q'} \right\rangle \\ &= \left\langle G_{aa}^{A}, J_{aa}(|p-p'|\,, |q-q'|) \right\rangle - \frac{1}{\omega^2}\ \left\langle G_q, J'_{aa}(|p-p'|\,, |q-q'|) \right\rangle \\ &= Z_{aa}^{p'q',\,p\,q} \end{aligned} \tag{4.28}$$

$J_{aa}(|p-p'|\,, |q-q'|)$ and $J'_{aa}(|p-p'|\,, |q-q'|)$ denote the cross-correlation functions $J_a^{p\,q} \otimes J_a^{p'\,q'}$ and $\frac{\partial}{\partial a} J_a^{p\,q} \otimes \frac{\partial}{\partial a} J_a^{p'\,q'}$ respectively. Here, $|x|$ reads the absolute value of x. Hence it is obvious that $Z_{aa}^{p\,q,\,p'q'}$ does not depend on the particular values of p, q, p' and q', but rather depends on the values of $|p-p'|$ and $|q-q'|$. Therefore, together with the fact that G_{aa}^{A} and G_q are cylindrically symmetric, the existence of four-fold symmetry represented by (4.25) is quite evident. Likewise, the rest of the symmetries can be proved analytically.

We can take advantage of these relationships to reduce the computational complexity in determining Z matrix in (4.16). Our implementation first calculates the essential

$Z_{aa}^{p\,q,\,p'q'}$ and $Z_{ab}^{p\,q,\,p'q'}$ forms only once, and the rest are found just mapping these coefficients according to (4.25) and (4.26). This will cut down the computational cost of matrix filling to less than one fifth of the original. In addition, when dynamic mapping is used rather than physically storing all the coefficients, one can even reduce the usage of the computer memory by the same factor.

Chapter 5

Numerical Evaluations in MoM

5.1 Introduction

In this chapter the numerical methods used in our implementation are discussed. First, we present some basics of numerical integration. Then the features of the particular numerical integration algorithm used are discussed without going into subtle mathematical details. We also introduce a novel approach of evaluating singular two-dimensional generalized exponential integrals (2D-GEI). This method was originally presented in [49] for evaluation of a simple 2D-GEI. It is now adapted to separable functions, which come up in space domain MoM based on subdomain basis and testing functions. Since the same integral reappears in other areas related to electromagnetic wave propagation, we shall discuss it in detail. Its performance is compared with the traditional approach in order to confirm its accuracy and efficiency. At last, the results are presented for a simple scatterer, a perfectly conducting square plate in free space.

5.2 Quadrature Integration

Numerical integration is essential to evaluate a definite integral, which has no analytical solution or whose analytical solution is too complex to be useful. The basic method of finding any given definite integral, either exactly or approximately, is called *numerical quadrature*. The method can be expressed mathematically as

$$\int_a^b f(x)\,dx \simeq \sum_{i=0}^{n} a_i\, f(x_i) \tag{5.1}$$

where

$\int_a^b f(x)\,dx$ is the definite integral to be evaluated,

a_i are constants and

$f(x_i)$ are functional evaluations of the given integrand $f(x)$ at some properly selected points x_i.

Equation (5.1) is a result of interpolating the given integral with some known and convenient functions whose integrations over the given limits are readily available [50]. These derived functional integrals are independent of the original integrand being evaluated and are collected as constants a_i. The part that depends on the original integrand is $f(x_i)$. The method of selecting x_i is dictated by the quadrature method used. Although equation (5.1) is supposed to be an approximation for a general function $f(x)$, depending on the quadrature method applied, it is capable of exact evaluation of some limited set of integrals. For example, the simple Newton-Cotes method which spaces the x_i equally in the interval $[a, b]$, is exact for all integrands consisting of polynomials up to degree n. Meanwhile a more powerful method, the Gaussian quadrature method, chooses points x_i such that the right hand side of (5.1) exactly evaluates integrals consisting of polynomials up to degree $2n+1$. In the following section, let us elaborate on the Gaussian quadrature method.

5.2.1 Gaussian quadrature integration

Gaussian quadrature chooses the points x_i in an optimal, rather than equally spaced, manner. The nodes x_i and coefficients a_i are all chosen to minimize the expected error obtained in performing the approximation (5.1) for an arbitrary function f. The best choice of these parameters is the one that produces the exact result for the largest possible class of polynomials. For an arbitrary f, there are total $2(n+1)$ parameters, both x_i and a_i. If the coefficients of a polynomial are considered as parameters, the class of polynomials of degree at most $2n+1$ also contains $2(n+1)$ parameters. Hence this is the largest class of polynomials for which it is possible to expect the formula to be exact in the given interval [50]. It can be shown [51] that the nodes x_i needed to produce exact results for any polynomial of degree less than $2n+1$, are the roots of the n th degree Legendre polynomial [51]. These roots are distinct, lie in the interval of $[-1, 1]$ and symmetric with respect to the origin. Upon choosing x_i, the a_i parameters can be easily determined. In fact both these x_i and a_i parameters are extensively tabulated for the predetermined interval $[-1, 1]$. They can easily be stored in the computer memory in advance and accessed on demand. In addition, a simple linear transformation is needed to map a general interval $[a, b]$ to the interval $[-1, 1]$.

5.2.2 Adaptive quadrature integration

Adaptive quadrature methods are intended to compute definite integrals by automatically taking into account the behavior of the integrand. Ideally, the user supplies only the integrand f, the interval $[a, b]$ and the accuracy desired for the integral $\int\limits_a^b f(x)\,dx$. The program then divides the interval into pieces of varying length so that numerical integration on the subintervals will produce results of acceptable precision. Therefore the final integration error is rather evenly distributed. Using the adaptive version of a particular quadrature method, one can save much of the unnecessary computation effort involved in integrating a function that contains both regions with large functional variation and regions with small functional variation.

5.2.3 Quadrature method in our implementation

The quadrature method we used, is a modified version of the adaptive Gaussian quadrature. It is modified to minimize the number of functional evaluations of $f(x_i)$. This particular numerical integration algorithm was introduced in [52] and [53], and later refined in [54]. It was applied to complex functions in [10]. The method starts with the basic Gaussian quadrature and then, augments more x_i points, which are chosen to evaluate the highest possible degree of polynomials rather than calculates a completely new set of x_i points as done in GQ. This is very important if the function f is complicated and its evaluation is time consuming. As a result, already calculated $f(x_i)$ are reused in the later iterations. However, this modification to the original GQ does not go unpunished. For a given number of points x_i, GQ would exactly evaluate a higher degree polynomial than the current method. Nevertheless, this modified version of GQ is believed to be the most effective method available for use in an automatic quadrature routine [54]. In the present implementation, an adaptive version of this quadrature method is applied.

5.3 Evaluating Two-Dimensional Generalized Exponential Integral

The rest of this chapter explores an innovative technique for evaluating a particular integral introduced in chapter 3. This integral is known as two-dimensional generalized-exponential integral (2D-GEI). It often appears in electromagnetic calculations. In the following we will generalize the efficient method introduced in [49] to evaluate this integral.

5.3.1 Theory

We define the 2D-GEI in Cartesian coordinates (Fig. 5.1) as:

$$I = \iint\limits_{\Delta S} \frac{\exp(-jkr)}{r} f(x', y')\, dx' dy' \tag{5.2}$$

where

$$r = \sqrt{x'^2 + y'^2 + a^2} \tag{5.3}$$

a is generally a complex constant and

$f(x', y')$ is a separable function in the x'- and y'- coordinates, that is,

$$f(x', y') = g(x')h(y') \tag{5.4}$$

where $g(x')$ and $h(y')$ are polynomials in x' and y' respectively.

It is obvious that when ΔS includes the origin, that is $x' = 0$ and $y' = 0$, and a is zero or almost zero, $1/r$ is either singular or nearly singular. When $1/r$ is far from being singular over ΔS, a simple numerical quadrature method can evaluate the integral accurately. But when $1/r$ is either singular or nearly singular, these methods are obviously not effective because they fail to achieve the required accuracy within a reasonable number of iterations. Therefore, an alternative method which effectively removes the singular behavior is to be applied. This can be achieved by transforming the integral (5.2) in Cartesian coordinates to polar coordinates and applying integrations by parts to evaluate the resulting integral [49]. We shall now present this method in detail.

Substituting (5.3) in (5.2)

$$I = \int_{x_1}^{x_2} \int_{y_1}^{y_2} f(x', y') \frac{\exp(-jk\sqrt{x'^2 + y'^2 + a^2})}{\sqrt{x'^2 + y'^2 + a^2})} dx'dy' \tag{5.5}$$

and setting

$$x' = \rho' \cos\theta' \tag{5.6}$$

$$y' = \rho' \sin\theta' \tag{5.7}$$

we get the polar equivalent of (5.2)

$$I = \int_0^{2\pi} \int_0^{\rho^c(\theta')} f(\rho'\cos\theta', \rho'\sin\theta') \frac{\exp(-jk\sqrt{\rho'^2 + a^2})}{\sqrt{\rho'^2 + a^2}} \rho' d\rho' d\theta' \tag{5.8}$$

Here x_1, x_2, y_1, y_2 and $\rho^c(\theta')$ are defined in Fig. 5.1. $\rho^c(\theta')$ is continuous over the entire θ' range and can be expressed as piecewise functions. According to Fig. 5.1,

$$\rho^c(\theta') = \begin{cases} y_2 \csc\theta' & for \quad \theta_1 \le \theta' < \theta_2 \\ x_1 \sec\theta' & for \quad \theta_2 \le \theta' < \theta_3 \\ y_1 \csc\theta' & for \quad \theta_3 \le \theta' < \theta_4 \\ x_2 \sec\theta' & for \quad (\theta_4 \le \theta' < 2\pi) \cup (0 \le \theta' < \theta_1) \end{cases} \tag{5.9}$$

The use of the identity

$$\frac{d}{d\rho'} \exp(-jk\sqrt{\rho'^2 + a^2}) = \frac{\exp(-jk\sqrt{\rho'^2 + a^2})}{\sqrt{\rho'^2 + a^2}} \rho'.(-jk) \tag{5.10}$$

then leads to

$$I = \frac{j}{k} \left[\int_0^{2\pi} \int_0^{\rho^c(\theta')} f'(\rho', \theta') \frac{d}{d\rho'} \exp(-jk\sqrt{\rho'^2 + a^2}) d\rho' d\theta' \right] \tag{5.11}$$

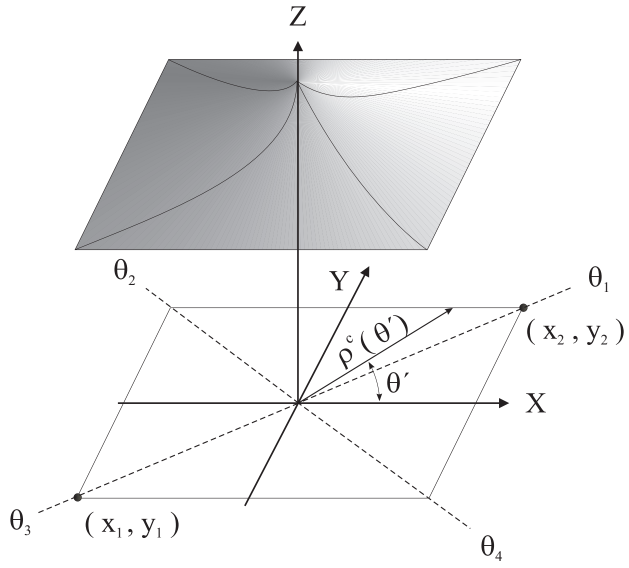

Fig. 5.1: *Two-dimensional generalized exponential integral defined over a rectangular region*

where, $f'(\rho',\theta') = f(\rho'\cos\theta', \rho'\sin\theta')$.

The integration by parts is generally expressed as [55]

$$\int u(x)\,\frac{dv(x)}{dx}\,dx = u(x)\,v(x) - \int v(x)\,\frac{du(x)}{dx}\,dx \tag{5.12}$$

When applied with respect to ρ', we obtain

$$\begin{aligned} I \;=\; & \underbrace{\int_0^{2\pi} \left(\left[\exp(-jk\sqrt{\rho'^2 + a^2}) f'(\rho',\theta') \right]_0^{\rho^c(\theta')} \right) d\theta'}_{I_1} \\ & \underbrace{- \int_0^{2\pi} \int_0^{\rho^c(\theta')} \exp(-jk\sqrt{\rho'^2 + a^2}) \frac{d}{d\rho'} f'(\rho',\theta') d\rho' d\theta'}_{I_2} \end{aligned} \tag{5.13}$$

From (5.13), it is obvious that the singularity found in (5.5) is no longer present. We shall now consider the subintegrals I_1 and I_2 separately.

$$I_1 = \int_0^{2\pi} \left[\exp(-jk\sqrt{\left(\rho^c(\theta')\right)^2 + a^2}) f'(\rho^c(\theta'),\theta') - \exp(-jka) f'(0,\theta') \right] d\theta' \tag{5.14}$$

I_1 is now in a numerically integrable form.

In order to find the derivative with respect to ρ' present in I_2, we shall apply the chain rule for multivariable functions [55] and exploit the separable nature of $f(x',y')$ given in (5.4).

$$I_2 = \int_0^{2\pi} \int_0^{\rho^c(\theta')} \exp(-jk\sqrt{\rho'^2 + a^2}) \left(\frac{dx'}{d\rho'} \frac{d}{dx'} + \frac{dy'}{d\rho'} \frac{d}{dy'} \right) f'(\rho', \theta')\, d\rho' d\theta' \tag{5.15}$$

$$\begin{aligned} I_2 \;&=\; \int_0^{2\pi} \int_0^{\rho^c(\theta')} \exp(-jk\sqrt{\rho'^2 + a^2}) \cos\theta' g'(\rho' \cos\theta')\, h(\rho' \sin\theta') d\rho' d\theta' && (5.16) \\ &+ \int_0^{2\pi} \int_0^{\rho^c(\theta')} \exp(-jk\sqrt{\rho'^2 + a^2}) \sin\theta' g(\rho' \cos\theta')\, h'(\rho' \sin\theta')\, d\rho' d\theta' && (5.17) \end{aligned}$$

Here $g'(x')$ and $h'(y')$ are derivatives with respect to x' and y', respectively. Although the functions $g(x')$ and $h(y')$ are continuous, neither $g'(x')$ nor $h'(y')$ are necessarily continuous over entire ΔS region. They are often piecewise continuous. Therefore ΔS has to be divided into piecewise continuous regions prior to the above process. These subintegrals are then evaluated numerically. Hence I_2 can be found by adding the individual contributions. This might give the impression that we have to evaluate more integrals than we originally started with. But a closer look will reveal that the division into smaller regions can be interpreted as a fixed numerical integration scheme, thereby not increasing the computation complexity proportionally but adding only a slight amount of computational overhead. Moreover, this division helps to increase the convergence of the adaptive integration quadrature. The numerical integration with respect to θ' in both I_1 and I_2 can be performed during one common cycle of program codes. This concludes the mathematical presentation of the evaluation of 2D-GEI. A comparison of the present approach and the conventional approach is now in order.

5.3.2 Accuracy and efficiency

The better accuracy of the present method for small a is already demonstrated in [49] and illustrated in Fig. 5.2. There, the function f is a simple triangular function in x-direction and 2D-GEI is evaluated for small values of a using a non-adaptive GQ method. In the inset of Fig. 5.2 the same integral is once again evaluated using more integration points (96x96 points vs 6x3 points) for the conventional method. The more computationally intensive result converges to the former result obtained by the present method with no additional increase in integration points. It is thus obvious that a higher accuracy can be attained by the present method for small values of a. Conventional quadrature methods in the Cartesian domain do not converge for very small a.

Figure 5.3 illustrates the efficiency of the present method. It shows that the number of floating point operations needed to acquire a particular accuracy when an adaptive quadrature method is applied, and $a = 0$. It is obvious that the number of floating point operations needed to acquire the same accuracy using the traditional adaptive method is

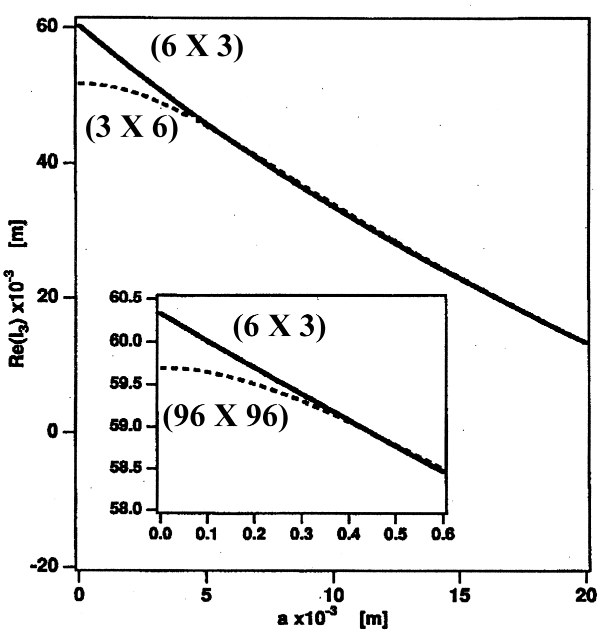

Fig. 5.2: *Accuracy of 2D-GEI evaluated for different value of the parameter a using the traditional method (dashed) and the present method (solid). The numbers within brackets represent the number of points used during the integration. [49]*

much higher than the present method. It is also noted that the traditional method fails to converge when higher accuracies, in other words lower relative errors, than those given in Fig. 5.3 are demanded. On the other hand, the proposed method produces converged results with the required accuracy.

5.3.3 Applications

We shall determine the current distribution of a square patch ($\lambda \times \lambda$) in free space in the presence of an incident plane wave as shown in Fig. 5.4. λ denotes the wavelength in free space. This simple structure is selected to keep other unnecessary details on DCIM (Discrete Complex Image Method) and MoM (Method of Moments) techniques to a minimum and demonstrate the current method merely as an independent technique. However, the full power of the suggested method can only be seen when combined with DCIM and MoM described in chapters 3 and 4, respectively.

We shall apply MPIE (Mixed Potential Integral Equation) formulation presented in section 2.4. The relevant magnetic vector- and scalar potential Green's functions in free space are given by [9]

$$A_x = \frac{\mu_0}{4\pi}\frac{\exp(-jkr)}{r}\hat{x} \tag{5.18}$$

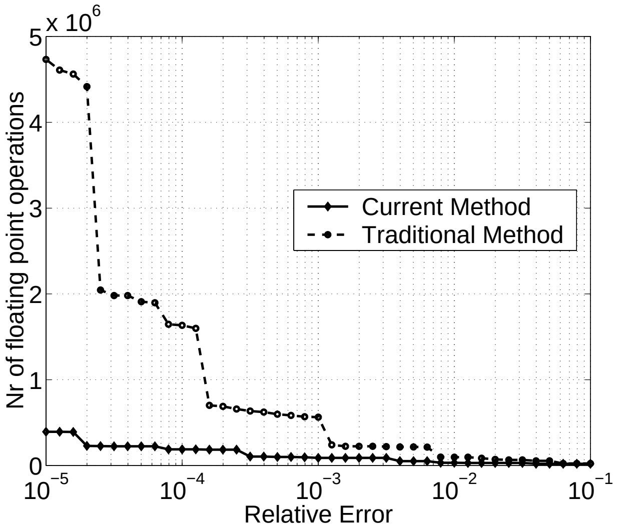

Fig. 5.3: *Comparing the efficiency of the traditional method and the present method when evaluating 2D-GEI ($a = 0$).*

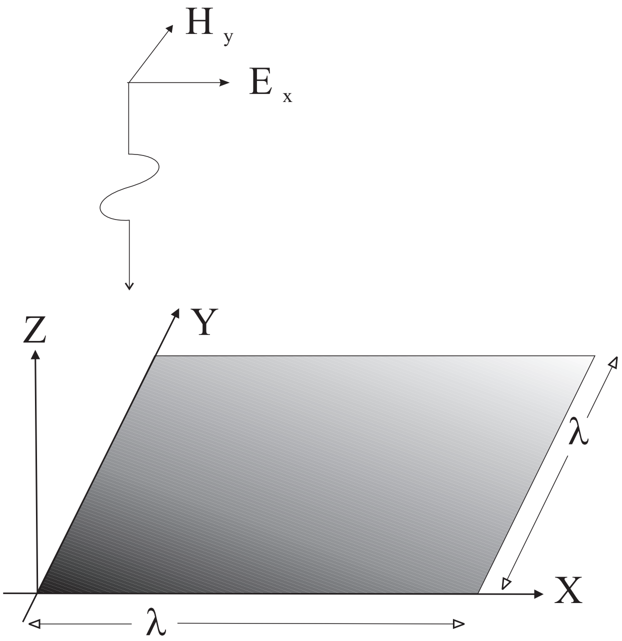

Fig. 5.4: *A perfectly conducing rectangular plate in free space in the presence of x-polarized plane wave.*

$$A_y = \frac{\mu_0}{4\pi}\frac{\exp(-jkr)}{r}\hat{y} \tag{5.19}$$

$$Q = \frac{\mu_0}{4\pi j\omega\epsilon_0}\frac{\exp(-jkr)}{r} \tag{5.20}$$

where

μ_0 and ϵ_0 are the permeability and permittivity of free space, respectively, and

r is the radial distance defined by $r = \sqrt{x^2 + y^2 + z^2}$ with x, y and z denoting Cartesian coordinates.

Applying the space domain MoM and proceeding as in chapter 4 lead to

$$ZI = V \tag{5.21}$$

where

Z is the mutual impedance coefficient matrix,

I is the current distribution vector and

V is the excitation vector.

Evaluating the singular numerical integrals using the present method, the elements in Z can be accurately determined. Solving (5.21), the induced surface current densities are found. We have illustrated the x-directed and y-directed induced surface current densities in Fig. 5.5 and 5.6 respectively. For comparison, the results for the same structure based on conventional quadrature methods [1] have also been reproduced in Fig. 5.7 and 5.8. A very good agreement is observed.

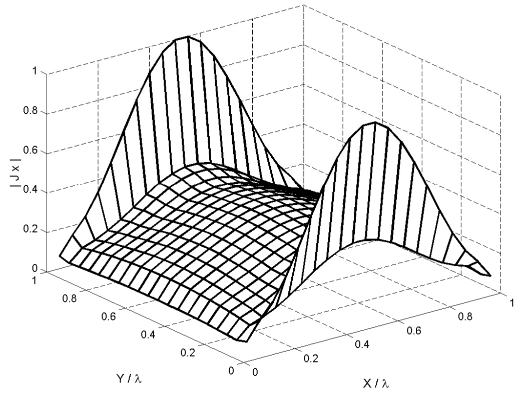

Fig. 5.5: *Normalized magnitude of the induced surface current density in x direction using the present method.*

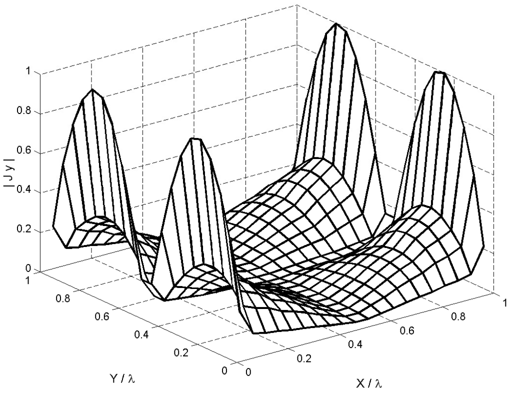

Fig. 5.6: *Normalized magnitude of the induced surface current density in y direction using the present method.*

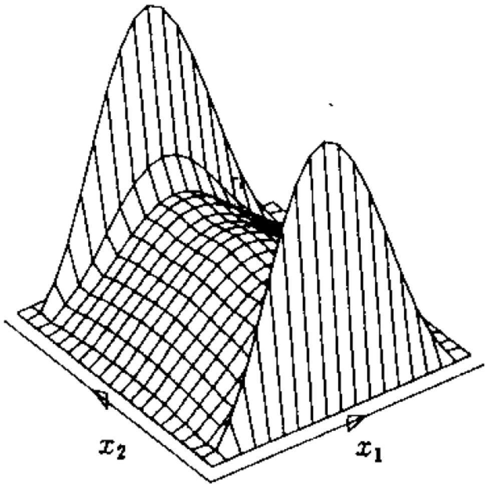

Fig. 5.7: *Normalized magnitude of the induced surface current density in x direction from [1].*

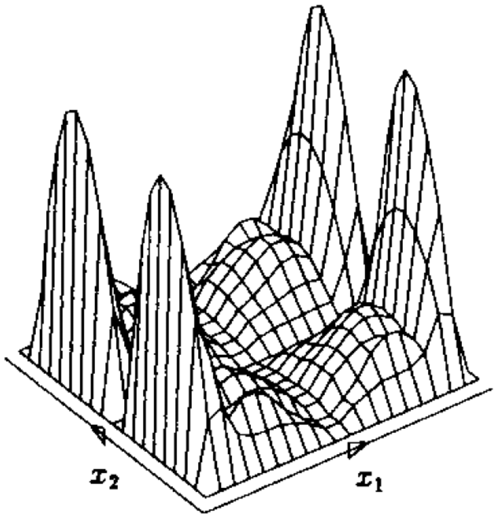

Fig. 5.8: *Normalized magnitude of the induced surface current density in y direction from [1].*

Chapter 6

Conjugate Gradient Fast Fourier Transform Method

6.1 Introduction

This chapter intends to introduce an efficient implementation of the conjugate gradient method (CGM) for computational electromagnetics. CGM is basically an iterative optimization procedure and is well suited for the treatment of operator equations. One such operator can be found in the system of linear equations already presented in chapter 4. It is also shown there that when expressed in matrix form, this system can be written as

$$[V] = [Z]\,[I] \tag{6.1}$$

where V and I are vectors and Z is a matrix. For such operator equations, CGM results in a properly converged solution in a finite number of iterations, if all computations are performed exactly [56]. However, due to the round-off errors introduced by the finite-length representation of digital computers, in practice convergence cannot be guaranteed in a finite number of steps. Nevertheless, CGM is considered as one of the fastest and most powerful methods for systems of linear equations characterized by ill-conditioned matrices.

The conjugate gradient method combined with fast Fourier transform exploits the linearity and space-invariant properties that are frequently found in many electromagnetic problems. Linearity implies that the superposition principle is applicable, i.e. the fields created by a complex source can be computed as the summation of the fields originated by each one of the elemental sources into which this source can be split. The space-invariant property suggests that the electromagnetic fields of each point source measured at an observation point depend only on the relative positions of the source point and the observation point. The systems with these two properties are called linear space invariant (LSI) systems.

According to chapter 4, the uniform discretization in MoM leads to a matrix equation of the form given by 6.1. The matrix Z is dense and has a Toeplitz (or block Toeplitz) structure. Often these matrices are ill-conditioned and the standard Gaussian elimination procedure [34] performs poorly. Nevertheless, it has been reported that such equation systems can be solved efficiently by using special technique developed ad hoc for matrices with a Toeplitz structure [57]. Greater advantages can be fetched by exploiting the LSI nature of the system. For example, the LSI property manifests in the space domain as a convolution, which can be calculated in the spectral domain using fast Fourier transform (FFT). Moreover, operations like derivatives that are cumbersome in the space domain, turn into simple algebraic operations in the spectral domain. Nevertheless, the complete transformation of a space domain problem into the spectral domain is very complicated because the boundary conditions often given in the spatial domain can not easily be expressed in the spectral domain [58].

6.2 Direct Methods vs Iterative Methods

The methods for solving a set of linear equation system are mainly divided into two classes; direct methods and iterative methods.

6.2.1 Direct methods

The two most popular direct methods used for solving a linear equation system are Cramer's rule and Gaussian elimination [34]. They proceed through a finite number of steps and produce a solution that would be exact were it not for round-off errors. Hence, the direct methods are really optimum in obtaining an exact solution, under the assumption that there are no truncation or round-off errors. However the advantage of obtaining a solution in a finite number of steps is overshadowed by the building up of truncation and round-off errors in direct methods. The effect of round off errors are more prominent for ill-conditioned large matrices and may lead to either inaccurate solutions or numerical instabilities.

6.2.2 Iterative methods

An iterative method is a self-correcting one. It repeats the corrections over and over, and produces a sequence of vectors that ideally converges to the solution. However, it may never reach the exact solution. The objective of the iterative methods is to get close to the exact solution faster than the direct methods. The computation is halted when an approximate solution is accurate enough, i.e. having achieved the specified accuracy or in the worst case, reached the preset maximum number of iterations. For large linear systems containing thousands of unknowns, iterative methods often have decisive advantages over direct methods. When the accuracy requirements are not stringent, a modest number of iterations will suffice to produce an acceptable solution. For sparse systems [34], iterative methods are often very efficient. Another advantage of iterative methods is that they are usually numerically stable and their round-off errors are limited only by the most recent stage of iteration [59]. Hence iterative methods are more suitable for large and ill-conditioned matrix inversions.

6.3 Basic Conjugate Gradient Method

6.3.1 Adjoint operator

The application of a CG scheme requires the adjoint operator defined with respect to a inner product operator, often denoted by $< >$. We define the adjoint operator L^A of the linear operator L based on the two arbitrary functions I_a and I_b.

$$< LI_a, I_b >=< I_a, L^A I_b > \tag{6.2}$$

Here, the inner product is defined as in chapter 4 over the 2D vector functions I_a and I_b [56]. The linear operator L is denoted by the following matrix multiplication.

$$V = LI \tag{6.3}$$

$$\begin{bmatrix} V_{ix} \\ V_{iy} \end{bmatrix} = \begin{bmatrix} Z_{xx} & Z_{xy} \\ Z_{yx} & Z_{yy} \end{bmatrix} \begin{bmatrix} I_x \\ I_y \end{bmatrix} \tag{6.4}$$

with V_{ix}, V_{iy}, I_x and I_y representing x- and y- directed excitations and current density coefficients, respectively. Z_{xx}, Z_{xy}, Z_{yx} and Z_{yy} are complex block matrices (chapter 4).

By imposing condition (6.2) on two arbitrary vectors I_a and I_b in the definition domain of the operator L, we can show that [58]

$$\begin{aligned} L^A &= (L^T)^* \\ &= L^H \end{aligned} \tag{6.5}$$

where L^T and L^H represent the transpose and Hermitian of the matrix L.

Assuming the block matrices in (6.4) are complex symmetric, which is the case when MoM is applied to uniformly discretized planar structure, L^A can be written as

$$L^A = \begin{bmatrix} Z^*_{xx} & Z^*_{yx} \\ Z^*_{xy} & Z^*_{yy} \end{bmatrix} \tag{6.6}$$

When $L = L^A$ the operator L is said to be self-adjoint and otherwise L is non self-adjoint. Hence, when the space domain MoM is applied to uniformly discretized planar stratified structures, the resulting operator L is non self-adjoint.

6.3.2 CGM algorithm

Using the following notations, we present one version of CGM as in the following algorithm.

The notation

I_n - Unknown vector

L - Linear operator in matrix form

V - Excitation vector

ε - Required accuracy

Input

L, V and ε

Initialization

I_0 is set to an arbitrary value. It is with no loss of generality set to zero.

$$\begin{aligned}
I_0 &= 0 \\
r_0 &= V - LI_0 \\
P_1 &= L^A r_0 \\
a_1 &= \frac{\left\|L^A r_0\right\|^2}{\left\|L^A P_1\right\|^2} \\
I_1 &= I_0 + a_1 P_1 \\
r_1 &= V - LI_1
\end{aligned} \tag{6.7}$$

Iteration

Algorithm proceeds until

$$\frac{\|V - LI\|}{\|V\|} < \varepsilon \tag{6.8}$$

where ε is the required accuracy.

Following operations are repeated until the above condition is met.

$$\begin{aligned}
r_{n,n-1} &= \frac{\left\|L^A r_{n-1}\right\|^2}{\left\|L^A r_{n-2}\right\|^2} \\
P_n &= L^A r_{n-1} + r_{n,n-1} P_{n-1} \\
a_n &= \frac{\left\|L^A r_{n-1}\right\|^2}{\left\|L^A P_n\right\|^2} \\
I_n &= I_{n-1} + a_n P_n \\
r_n &= r_{n-1} + a_n L P_n
\end{aligned} \tag{6.9}$$

Output

I_n and the ultimate value for $\frac{\|V-LI\|}{\|V\|}$, which is a measure of the quality of the solution I_n unless the operator L is extremely ill-conditioned.

6.4 Conjugate Gradient Method Combined with Fast Fourier Transform

6.4.1 Discrete Fourier transform

Definitions

The Discrete Fourier Transform (DFT) allows a discrete periodic function to be expanded in a series of complex exponentials.

One-dimensional discrete Fourier Transform (1D DFT) Let us consider a 1D discrete periodic function $x(n)$ of period N,

$$x(n) = x(n + mN) \quad \text{for} \quad \begin{array}{l} n = 0,\ 1,\ 2,\ ...,\ N-1 \\ m = 0,\ \pm 1,\ \pm 2,\ ... \end{array} \tag{6.10}$$

Then 1D DFT of $x(n)$, denoted as $X(k)$, is written as

$$X(k) = \sum_{n=0}^{N-1} x(n) \exp\left[-j2\pi \tfrac{kn}{N}\right] \quad \text{for} \quad k = 0,\ 1,\ 2,\ ...,\ N-1 \tag{6.11}$$

Given $X(k)$, the corresponding $x(n)$ is found using the one-dimensional inverse discrete Fourier transform (1D IDFT) expressed as

$$x(n) = \tfrac{1}{N} \sum_{k=0}^{N-1} X(k) \exp\left[j2\pi \tfrac{kn}{N}\right] \quad \text{for} \quad n = 0,\ 1,\ 2,\ ...,\ N-1 \tag{6.12}$$

Note that parameters n and k are just indices in time and spectral domain. The index k should not to be mixed up with the propagation constant introduced in chapters 2 and 3. Figures 6.1 and 6.2 show an example of a discrete sequence and its DFT, respectively.

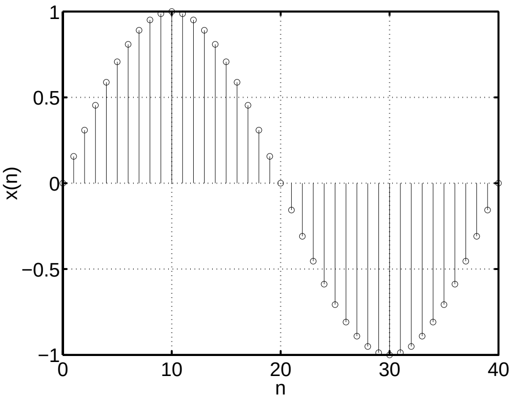

Fig. 6.1: *Discret function x(n)*

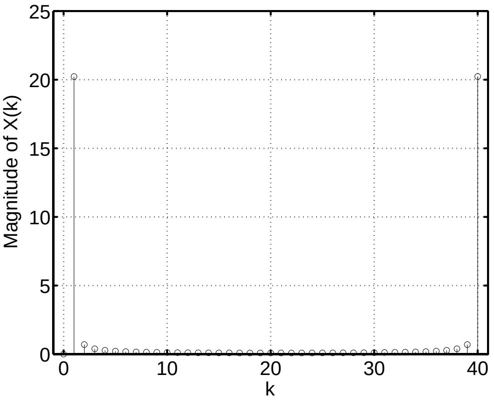

Fig. 6.2: *DFT of the discret x(n)*

Two-dimensional discrete Fourier Transform (2D DFT) Discrete periodic functions of more than one variable can also be expanded in terms of complex exponentials with the help of DFT. We shall limit our attention here to the two-dimensional case. A general 2D discrete periodic function of periods M and N can be expressed as

$$x(n,m) = x(n+pN, m+qM) \quad \text{for} \quad \begin{array}{l} n = 0,\ 1,\ 2,\ ...,\ N-1 \\ m = 0,\ 1,\ 2,\ ...,\ M-1 \\ p = 0,\ \pm 1,\ \pm 2,\ ... \\ q = 0,\ \pm 1,\ \pm 2,\ ... \end{array} \tag{6.13}$$

Then the 2D DFT of this $x(n,m)$, denoted by $X(k,l)$, is given as

$$X(k,l) = \sum_{n=0}^{N-1}\sum_{m=0}^{M-1} x(n,m)\exp\left[-j2\pi\tfrac{kn}{N} - j2\pi\tfrac{lm}{M}\right] \quad \text{for} \quad \begin{array}{l} k = 0,\ 1,\ 2,\ ...,\ N-1 \\ l = 0,\ 1,\ 2,\ ...,\ M-1 \end{array} \tag{6.14}$$

Given $X(k,l)$, the corresponding $x(n,m)$ is found using the two-dimensional inverse discrete Fourier transform (2D IDFT)

$$x(n,m) = \tfrac{1}{NM}\sum_{k=0}^{N-1}\sum_{l=0}^{M-1} X(k,l)\exp\left[j2\pi\tfrac{kn}{N} + j2\pi\tfrac{lm}{M}\right] \quad \text{for} \quad \begin{array}{l} n = 0,\ 1,\ 2,\ ...,\ N-1 \\ m = 0,\ 1,\ 2,\ ...,\ M-1 \end{array} \tag{6.15}$$

Properties of DFT

The most important properties of 1D-DFT and 2D-DFT are summarized in Table 6.1 and Table 6.2, respectively. In addition, both spatial and spectral sequences are implicitly periodic. That is in 1D

$$x(n+N) = x(n) \quad \text{for all} \quad n \tag{6.16}$$

$$X(k+N) = X(k) \quad \text{for all} \quad k \tag{6.17}$$

Here N is the period of the sequences $x(n)$ and $X(k)$. Equivalently in 2D,

$$x(n+N, m+M) = x(n,m) \quad \text{for all} \quad n \text{ and } m \tag{6.18}$$

$$X(k+N, l+M) = X(k,l) \quad \text{for all} \quad k \text{ and } l \tag{6.19}$$

N and M are the periods of the sequences $x(n,m)$ and $X(k,l)$. The circular shifting of a periodic sequence is obtained by linearly shifting the periodically extended version of the given sequence. In general the circular shift of the sequence may be represented as the index modulo N. Thus we may represent a circularly shifted sequence by an amount of n_0 as

$$\begin{aligned} x_{circularly\ shifted}(n) &= x((n-n_0) \bmod N) \\ &= x(n-n_0)_N \end{aligned} \tag{6.20}$$

Here, the operation $x \bmod y$ returns the signed remainder after the division $\frac{x}{y}$, i.e.

$$x \bmod y = \begin{cases} x - y \ \mathrm{floor}(\frac{x}{y}) & \text{if} \quad y \neq 0 \\ x & \text{if} \quad y = 0 \end{cases} \tag{6.21}$$

where the operation floor(x) rounds x to the nearest integer less than or equal to x.

Property	Spatial domain	Transformed (spectral) domain
Linearity	$\alpha x(n) + \beta y(n)$	$\alpha X(k) + \beta Y(k)$
Circular space shifting	$x(n-n_0)_N$	$X(k)\exp(-j2\pi\frac{kn_0}{N})$
Circular spectrum shifting	$x(n)\exp(j2\pi\frac{nk_0}{N})$	$X(k-k_0)_N$
Time reversal	$x(N-n)$	$X(N-k)$
Circular space convolution	$x(n) \circledcirc y(n)$	$X(k)Y(k)$
Multiplication	$x(n)y(n)$	$\frac{1}{N}X(k) \circledcirc Y(k)$
Complex-conjugate properties	$x^*(n)$	$X^*(N-k)$
Parseval's theorem	$\sum\limits_{n=0}^{N-1} x(n)y^*(n)$	$\frac{1}{N}\sum\limits_{k=0}^{N-1} X(k)Y^*(k)$

Table 6.1: *Properties of one-dimensional DFT*

Property	Spatial domain	Transformed (spectral) domain
Linearity	$\alpha x(n,m) + \beta y(n,m)$	$\alpha X(k,l) + \beta Y(k,l)$
Circular space shifting	$x(n-n_0, m-m_0)_{NM}$	$X(k.l)\exp[-j2\pi(\frac{kn_0}{N} + \frac{lm_0}{M})]$
Circular spectrum shifting	$x(n,m)\exp(j2\pi(\frac{nk_0}{N} + \frac{ml_0}{M}))$	$X(k-k_0, l-l_0)_{NM}$
Time reversal	$x(N-n, M-m)$	$X(N-k, M-l)$
Circular space convolution	$x(n,m) \circledcirc y(n,m)$	$X(k,l)Y(k,l)$
Multiplication	$x(n,m)y(n,m)$	$\frac{1}{NM}X(k,l) \circledcirc Y(k,l)$
Complex-conjugate properties	$x^*(n,m)$	$X^*(N-k, M-l)$
Parseval's theorem	$\sum\limits_{m=0}^{M-1}\sum\limits_{n=0}^{N-1} x(n,m)y^*(n,m)$	$\frac{1}{NM}\sum\limits_{l=0}^{M-1}\sum\limits_{k=0}^{N-1} X(k,l)Y^*(k,l)$

Table 6.2: *Properties of two-dimensional DFT*

6.4.2 More on convolution property of DFT

Definitions

1D Linear convolution

When $x(n)$ and $y(n)$ are discrete sequences, the linear convolution between them is another discrete sequence $z_{lin}(n)$ defined by

$$z_{lin}(n) = \sum_{p=-\infty}^{\infty} x(p)y(n-p) \tag{6.22}$$

Hence, the linear convolution is a composite operation of folding, shifting, multiplication and summation [60].

1D Circular (cyclic) convolution

When $x(n)$ and $y(n)$ are discrete periodic sequences of period N, the circular convolution between them is another discrete periodic sequence $z_{cir}(n)$ defined by

$$z_{cir}(n) = \sum_{p=0}^{N-1} x(p)y(n-p)_N \tag{6.23}$$

The circular convolution involves basically the same four steps as the linear convolution, i.e. folding, shifting, multiplying and summing. The basic difference between these two types of convolution is that, in circular convolution, the folding and shifting operations are performed in a circular fashion by computing the index of one of the sequences after modulo N operation, whereas in linear convolution there is no modulo N operation.

Likewise, the corresponding 2D linear and circular convolution can be expressed by

$$z_{lin}(n,m) = \sum_{p=-\infty}^{\infty} \sum_{q=-\infty}^{\infty} x(p,q)y(n-p,m-q) \tag{6.24}$$

and

$$z_{cir}(n,m) = \sum_{p=0}^{N-1} \sum_{q=0}^{M-1} x(p,q)y(n-p,m-q)_{NM} \tag{6.25}$$

Efficient computation of DFT : FFT algorithm

The direct computation of DFT following either (6.11) or (6.14) is basically inefficient since it does not exploit the symmetry and periodicity properties of the phase factor of the transformation. Consequently, computing N values of the 1D-DFT requires N^2 complex multiplications and $(N^2 - N)$ complex additions. Using the symmetry and periodicity properties of the phase factor, it is shown in [60] that the total number of complex

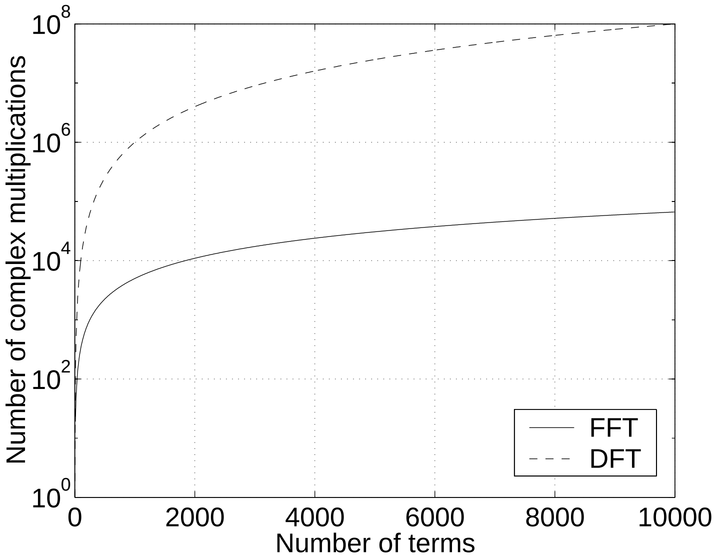

Fig. 6.3: *Number of complex multiplications needed by FFT and DFT as a function of number of terms N*

multiplications can be reduced to $(N/2)\log_2 N$. The number of complex additions is also reduced to $N\log_2 N$. Such computationally efficient algorithms are collectively known as fast Fourier transform (FFT) algorithms. Figures 6.3 and 6.4 show the number of multiplications and additions required by DFT and FFT (radix-2) as a function of N. Accordingly for larger N, the use of FFT to determine DFT will cut down the processing time significantly.

Linear convolution based on FFT

The efficient computation of DFT using FFT leads in turn to efficient computation of spatial circular convolution, since the spatial circular convolution of two periodic sequences when performed in spectral domain mainly involves computing DFT of the two sequences, multiplication of computed DFTs and then computing IDFT of the resulting product. Unfortunately, it is the linear convolution that is frequently encountered in practical applications, not the circular convolution. Therefore, attempts have been made to compute the linear convolution via circular convolution.

Following the definition (6.22) of linear convolution, the length $L_{z(n)_{lin}}$of the resulting sequence $z(n)$ is equal to $L_{x(n)}+L_{y(n)}-1$, where $L_{x(n)}$ and $L_{y(n)}$ are the lengths of finite sequences $x(n)$ and $y(n)$. On the other hand, the circular convolution between two periodic sequences of period N results in another sequence of period N. However, both these sequences resulted from linear and circular convolution can be made equal, if the period N of the circular convolution is selected as $L_{z(n)_{lin}}$, the length of the sequence resulted from linear convolution. This implies that both sequences used in circular convolution

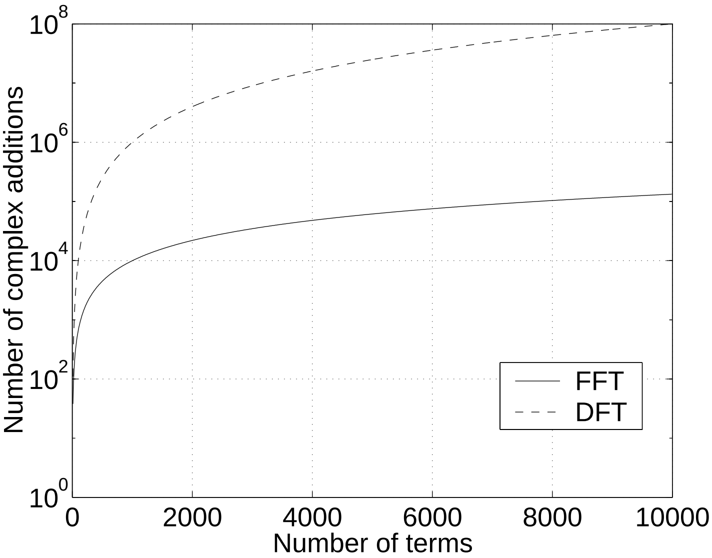

Fig. 6.4: *Number of complex additions needed by FFT and DFT as a function of number of terms N*

should be extended to the periodic sequences of length $L_{z(n)_{lin}}$ by adding additional zeros, a process known as zero-padding. These additional zeros avoid the aliasing effect due to the circular convolution and make the final result equivalent to the result from the corresponding linear convolution. Since the circular convolution is efficiently calculated using FFT, the use of circular convolution for calculating linear convolution now extends these efficiencies to linear convolution computations as well.

Although the previous discussion explained the scenario in one dimension, the same principles are equally valid for higher dimensions. Applying MoM to analyze stratified media frequently leads to matrix multiplications, which resemble 2D linear convolutions. Therefore, much of the mathematical complexity involved in these matrix multiplications can be reduced by exploiting FFT.

Performing Matrix multiplication based on FFT

The single matrix multiplication in (6.4) can be expanded to the following two matrix equations:

$$\begin{aligned} V_{ix} &= Z_{xx} \cdot I_x + Z_{xy} \cdot I_y \\ V_{iy} &= Z_{yx} \cdot I_x + Z_{yy} \cdot I_y \end{aligned} \tag{6.26}$$

When the number of discretization cells in x- and y directions are M and N, respectively I_x and I_y are vectors of length MN. Then the corresponding dimensions of each Z_{xx}, Z_{xy}, Z_{yx} and Z_{yy} would be MN by MN. In practice, each matrix multiplication in (6.26) resembles a two-dimensional linear convolution. For example, let us denote any one of these four multiplications as

$$V^{NM\times 1} = Z^{MN\times MN} \cdot I^{NM\times 1} \tag{6.27}$$

where

$$I = \begin{bmatrix} I_{(0,0)} \\ I_{(0,1)} \\ \vdots \\ I_{(0,N-1)} \\ I_{(1,0)} \\ I_{(1,1)} \\ \vdots \\ I_{(1,N-1)} \\ \vdots \\ \vdots \\ I_{(M-1,0)} \\ I_{(M-1,1)} \\ \vdots \\ I_{(M-1,N-1)} \end{bmatrix} \tag{6.28}$$

$$Z^T = \begin{bmatrix} Z_{(0,0)} & Z_{(0,1)} & Z_{(0,2)} & \cdots & Z_{(M-1,N-1)} \\ Z_{(0,-1)} & Z_{(0,0)} & Z_{(0,1)} & \cdots & Z_{(M-1,N-2)} \\ \vdots & \dots & \dots & \dots & \vdots \\ Z_{(0,1-N)} & Z_{(0,2-N)} & Z_{(0,3-N)} & \cdots & Z_{(M-1,0)} \\ Z_{(-1,0)} & Z_{(-1,1)} & Z_{(-1,2)} & \cdots & Z_{(M-2,N-1)} \\ Z_{(-1,-1)} & Z_{(-1,0)} & Z_{(-1,1)} & \cdots & Z_{(M-2,N-2)} \\ \vdots & \dots & \dots & \dots & \vdots \\ Z_{(-1,1-N)} & Z_{(-1,2-N)} & Z_{(-1,3-N)} & \cdots & Z_{(M-2,0)} \\ \vdots & \dots & \dots & \dots & \vdots \\ \vdots & \dots & \dots & \dots & \vdots \\ Z_{(1-M,0)} & Z_{(1-M,1)} & Z_{(1-M,2)} & \cdots & Z_{(0,N-1)} \\ Z_{(1-M,-1)} & Z_{(1-M,0)} & Z_{(1-M,1)} & \cdots & Z_{(0,N-2)} \\ \vdots & \dots & \dots & \dots & \vdots \\ Z_{(1-M,1-N)} & Z_{(1-M,2-N)} & Z_{(1-M,3-N)} & \cdots & Z_{(0,0)} \end{bmatrix} \tag{6.29}$$

$$V = \begin{bmatrix} V_{(0,0)} \\ V_{(0,1)} \\ \vdots \\ V_{(0,N-1)} \\ V_{(1,0)} \\ V_{(1,1)} \\ \vdots \\ V_{(1,N-1)} \\ \vdots \\ \vdots \\ V_{(M-1,0)} \\ V_{(M-1,1)} \\ \vdots \\ V_{(M-1,N-1)} \end{bmatrix} \tag{6.30}$$

It can also be expressed in as

$$V(n,m) = \sum_{p=0}^{M-1} \sum_{q=0}^{N-1} I(p,q) \cdot Z(n-p, m-q) \tag{6.31}$$

This is the same as 2D linear convolution between I and Z matrices, which can be expressed in matrix form

$$[V]_{folded}^{M\times N} = [Z_{compact}]^{(2M-1)\times(2N-1)} * [I]_{folded}^{M\times N} \tag{6.32}$$

where

$$V_{folded} = \begin{bmatrix} V_{(M-1,N-1)} & V_{(M-1,N-2)} & \cdots & V_{(M-1,0)} \\ V_{(M-2,N-1)} & V_{(M-2,N-2)} & \cdots & \vdots \\ \vdots & \vdots & \vdots & \vdots \\ V_{(0,N-1)} & V_{(0,N-2)} & \cdots & V_{(0,0)} \end{bmatrix} \tag{6.33}$$

$$Z_{compact} = \begin{bmatrix} Z_{(M-1,N-1)} & Z_{(M-1,N-2)} & \cdots & Z_{(M-1,1-N)} \\ Z_{(M-2,N-1)} & Z_{(M-2,N-2)} & \cdots & \vdots \\ \vdots & \vdots & \vdots & \vdots \\ Z_{(1-M,N-1)} & Z_{(1-M,N-2)} & \cdots & Z_{(1-M,1-N)} \end{bmatrix} \tag{6.34}$$

$$I_{folded} = \begin{bmatrix} I_{(M-1,N-1)} & I_{(M-1,N-2)} & \cdots & I_{(M-1,0)} \\ I_{(M-2,N-1)} & I_{(M-2,N-2)} & \cdots & \vdots \\ \vdots & \vdots & \vdots & \vdots \\ I_{(0,N-1)} & I_{(0,N-2)} & \cdots & I_{(0,0)} \end{bmatrix} \tag{6.35}$$

Despite both (6.27) and (6.32) result in the same 2D matrix $V(n, m)$, the later form is very compact, where the GF coefficient matrix only consists of $(2N - 1) \times (2M - 1)$ coefficients rather than $NM \times NM$ coefficients needed in the representation of (6.27). Thus the representation (6.32) eliminates much of the duplicating coefficients in matrix Z, with no loss of accuracy. To our knowledge, this is the first time this representation has been reported explicitly. It eliminates the use of unnecessarily larger matrices in a typical computer implementation and spare the much needed processor time and memory space. In addition this representation eases the software coding and allows the use of efficient codes, for example, codes written for matrix computations on parallel processors. Since the 2D linear convolution can be efficiently calculated by 2D-FFT as explained in section 6.4.2, the representation (6.32) with its compact 2D matrices is compatible with the rest of the implementation.

The basic CGM algorithm introduced in section 6.3 does contain several matrix multiplications. For large matrices these multiplications, unless they are handled efficiently, will waste much of the computer resources, both in terms of processing time and memory. However, these matrix multiplications can be performed efficiently by exploiting the LSI property inherent to matrices, which are results of space domain MoM with uniform discretization. Thus, using 2D-FFT, as illustrated above, one can make the CGM algorithm much faster and more efficient. The resulting algorithm, CGM combined with FFT, is called the conjugate gradient fast Fourier transform (CG-FFT).

6.4.3 Practical 2D CG-FFT implementation

We implement the CG-FFT algorithm based on (6.32). When applied to electromagnetic scattering and radiation problems, the compact versions of Z_{xx}, Z_{xy}, Z_{yx} and Z_{yy} contain all the necessary GF coefficients (GFCs) needed for the calculations. There are still some redundancies present among the coefficients of these matrices due to not yet exploited implicit symmetries. Hence, a further reduction of the size of these matrices is possible during a particular implementation. The final version of the implementation follows the CGM outlined in section 6.3.2. In addition, 2D FFT is used when performing all the matrix multiplications.

Another advantage of using the above mentioned representation now becomes obvious when analyzing large arbitrary planar structures. Since the discretization of large arbitrary structures requires the calculation of a large number of different GFCs, a systematic way to calculate them in advance would be difficult. Moreover, a minor modification to the structure may require the complete recalculation of all the matrices or, in a rather smart method, the calculation of only a few GFCs on the fly to make the necessary alterations to the previous GFC matrices. This may slow down certain functionalities like optimization of a complex planar structure with respect to a particular geometrical parameter. However, the representation in (6.32) assumes that matrix $Z_{compact}$ contains all possible GFCs which are needed for a selected discretization of the considered planar area, thus eliminating such problems. On the other hand, calculating the entire spectrum of GFCs in advance would be a drawback in a situation where the most of the calculated coefficients do not actively contribute to the solution, thus wasting expensive processing and memory resources. Therefore, the above formulation is recommended when the planar structure is complex and dense, thereby minimizing the calculation and storage of unnecessary GFCs.

6.4.4 Convergence and accuracy of 2D CG-FFT

Convergence of CG-FFT

The minimum number of iterations needed to solve (6.1) using CG algorithm has shown to be equal to the number of unknowns [56]. This limit is purely theoretical and assumes that all mathematical operations are carried out exactly. The finite accuracy offered by modern computers, though quite satisfactory for most practical purposes, does not guarantee full convergence of the CG algorithm within this minimum number of iterations. Therefore a practically implemented CGM may require more iterations than the theoretical minimum for a proper convergence. For a non-self adjoint operator, which is the case here, CGM guarantees a monotonic convergence. This means that the relative mean square error always decreases with the number of iterations. As a result, the exact point of convergence is not uniquely defined. Therefore the number of iterations needed also depends on the required accuracy of the final solution as well. It is stated in [61] and [62] that for most practical purposes the number of iterations needed in CG algorithm often lies between $N/4$ and $N/2$, where N is the number of unknowns. However, such limits are far from being universal since the number of iterations highly depends on the properties of the linear operator concerned. As the point of exact convergence is difficult to determine, the common practice is to impose the following criterion on the residual norm in order to keep track of the convergence. This criterion which is already applied in the CG algorithm in section 6.3.2, is expressed as

$$\frac{\|V - ZI\|}{\|V\|} < \varepsilon$$

Here, ε is a predetermined value, and the left hand side denotes the residual norm.

For example choosing $\varepsilon = 10^{-4}$, it is expected that a solution accurate to few decimals would be achieved. Nevertheless, this criterion does tend to fail when the linear operator, or the matrix representing the linear operator, is badly conditioned [63].

Let us demonstrate the convergence properties of CG-FFT, when applied to a simple electromagnetic scattering problem. Figure 5.4 shows that a plane wave is incident on a perfectly conducting square patch located in free space. The size of the patch is λ by λ where λ denotes the wave length in free space. The induced current densities on the patch are found by solving the linear equation system resulting from a space domain MoM formulation. The same structure is analyzed for different discretizations and the residual norm is found as a function of the number of iterations for each discretization. Figure 6.5, summarizes the convergence properties of the above algorithm for different discretizations.

It is obvious that CG-FFT for this particular structure converges monotonically and rapidly. Typical profiles of the x-directed and y-directed induced surface current densities J_x and J_y are shown in Fig. 6.6 and 6.7, respectively. The current densities along the

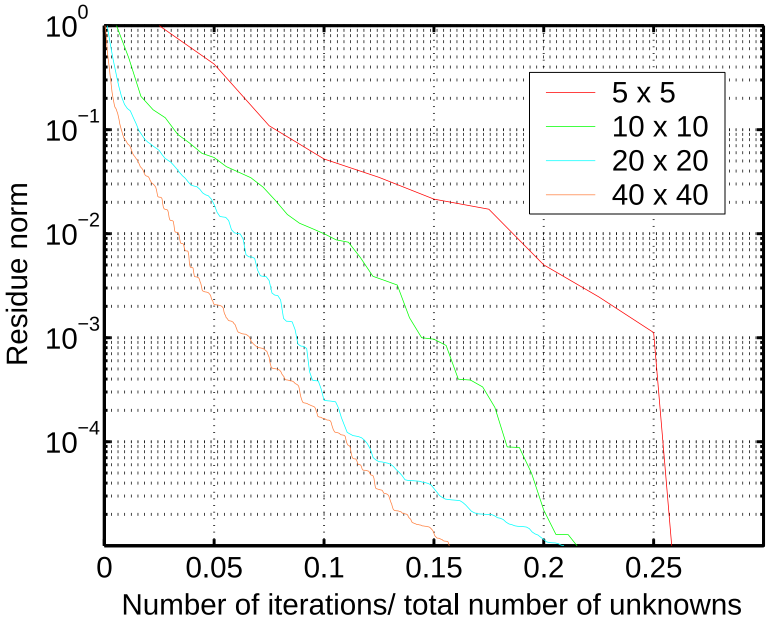

Fig. 6.5: *The monotonic decrease of residue norms as a function of the number of iterations. Different grades of discretizations such as 5 by 5, 10 by 10 , 20 by 20 and 40 by 40 are used*

lines $y = \lambda/2$ and $x = \lambda/2$ are shown in Fig. 6.8 and 6.9 respectively for different grades of discretizations.

Illustrating the accuracy of CG-FFT

In order to illustrate the accuracy of the implemented CG-FFT algorithm, we solve the same structure using the direct matrix inversion. The matrix inversion is performed using the routines available in *MATLAB 6.1*. The result is then compared with the previous results obtained by applying CG-FFT method. Figures 6.10 and 6.11 compare the x-directed surface current density along the lines $y = \lambda/2$ and $x = \lambda/2$ obtained by CG-FFT and direct matrix inversion. Both solutions are found for a 20 by 20 mesh. Almost a perfect agreement is noted.

It is also worth mentioning a last comment on convergence and accuracy of CG-FFT method. The proper convergence of CG-FFT to a particular solution does not necessarily mean that we have found the correct solution for the problem at hand because it is possible for a given linear operator and an excitation possess more than one possible solution. Such non uniqueness often results from the internal resonances generated within the structure [61].

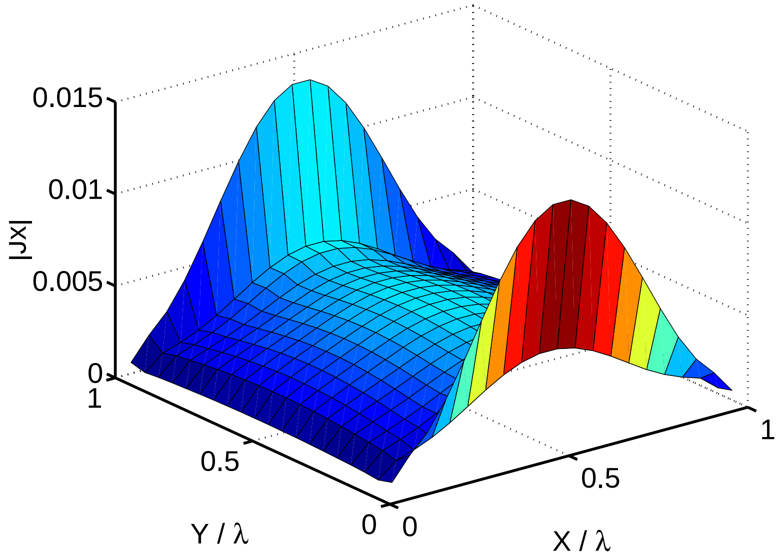

Fig. 6.6: *x-directed surface current density J_x for the discretization of 20 by 20*

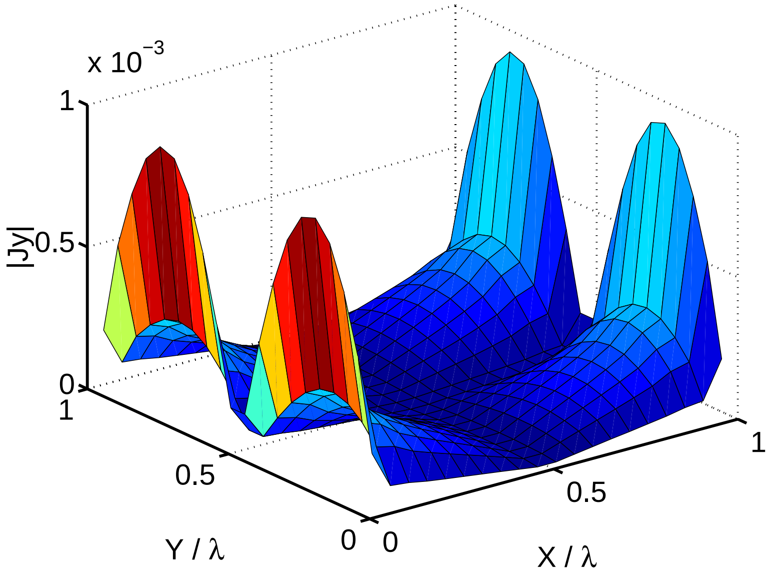

Fig. 6.7: *y-directed surface current density J_y for the discretization of 20 by 20*

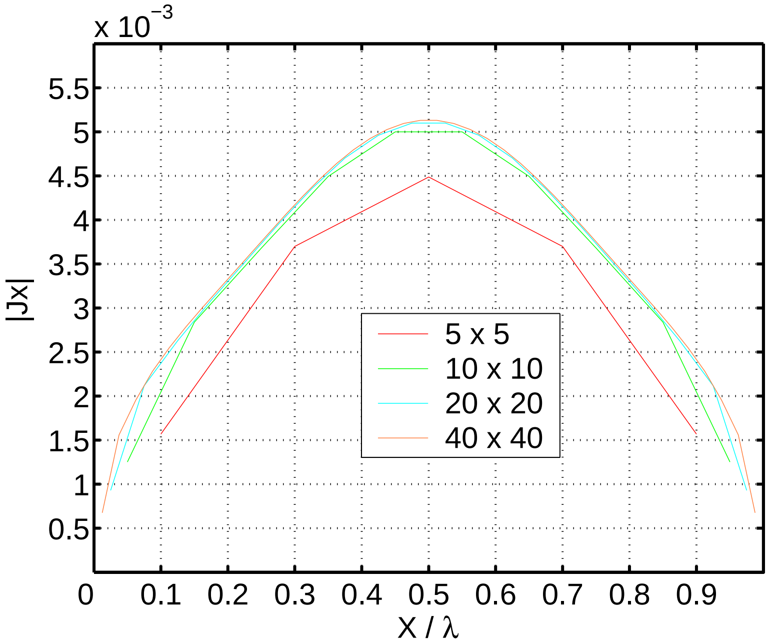

Fig. 6.8: *Converged x-directed surface current density J_x along the line $y = \lambda/2$ for different discretizations*

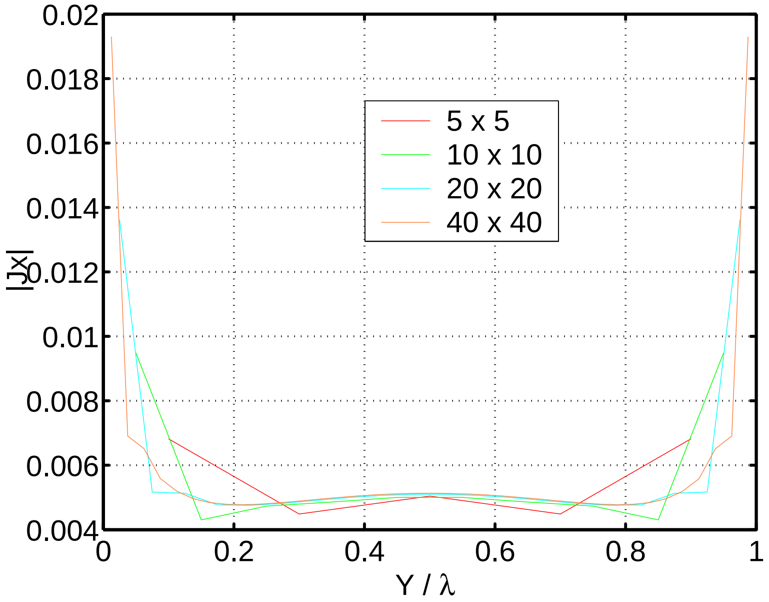

Fig. 6.9: *Converged x-directed current density J_x along the line $x = \lambda/2$ for different discretizations*

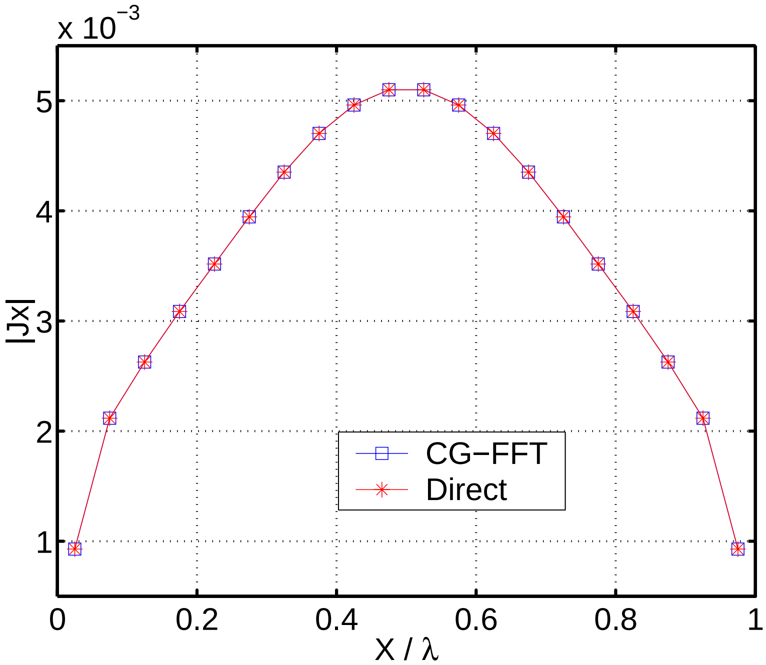

Fig. 6.10: *Comparison of x-directed surface current density J_x along the line $y = \lambda/2$ obtained by CG-FFT and direct matrix inversion*

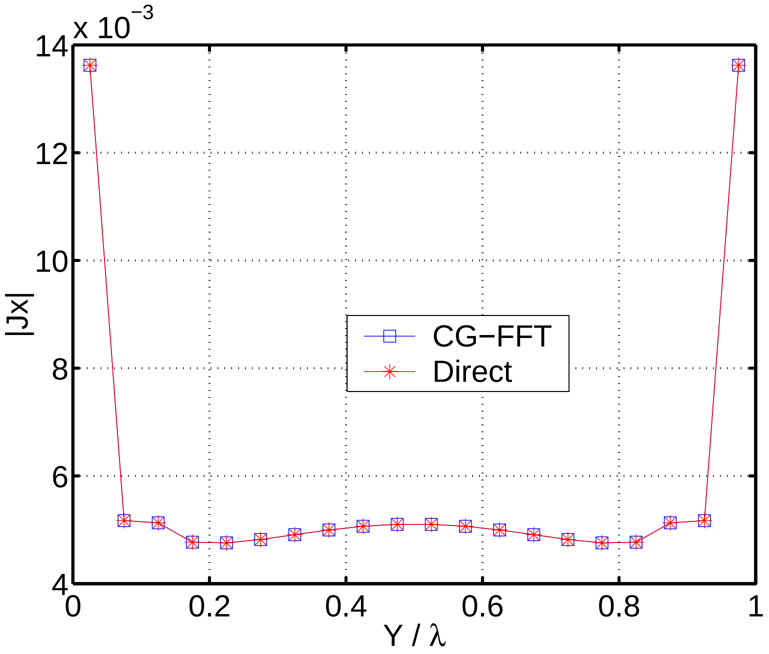

Fig. 6.11: *Comparison of* x*-directed surface current density* J_x *along the line* $x = \lambda/2$ *obtained by CG-FFT and direct matrix inversion*

Chapter 7

De-embedding Techniques

7.1 Introduction

7.1.1 De-embedding

De-embedding generally refers to the process of extracting unknown parameters from a known set of data. However, the concrete meaning of the de-embedding depends on the context. In this chapter, de-embedding refers to the process of extracting scattering parameters from the current density distributions induced on strip structures etched on planar stratified media.

7.1.2 Scattering (S) parameters

S parameters commonly characterize the port behavior of a general multiport network. Such a characterization eliminates the exhaustive electromagnetic wave considerations of the multiport networks and, allows the designer to represent a complex microwave network in terms of a few parameters. S parameters are defined in terms of either voltage-, current- or power waves. Hence they are respectively referred to as voltage, current and generalized S parameters. The transformations among these different types of S parameters are simple and depend only on the characteristic impedances of the ports. For example, the generalized S parameters, which are defined in terms of power waves are simply normalized versions of either voltage or current waves with respective to the corresponding characteristic impedances of the ports [64]. Since planar structures in stratified media are often characterized by their current density distributions, we shall confine ourselves to S parameters defined in terms of current waves. Nevertheless for reciprocal networks, they are equivalent to S parameters defined in terms of voltage waves.

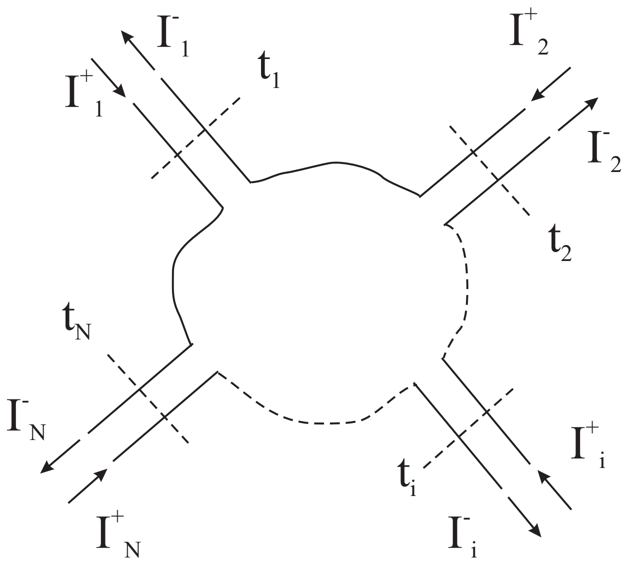

Fig. 7.1: *Arrows denote the propagation direction of the incident and reflected current waves. Furthermore, both I_n^+ and I_n^- are assumed to flow into the port n. t_i denotes the reference plane of the i th port*

For the multiport network shown in Fig. 7.1, the S parameters can be defined as

$$S_{ij} = \frac{I_i^-}{I_j^+} \qquad I_j^+ = 0 \quad \text{for} \quad i \neq j \tag{7.1}$$

where

I_j^+ is the amplitude of the incident current wave on port j and

I_i^- is the amplitude of the reflected current wave on port i.

Therefore, for a given multiport, all currents are coupled together according to

$$\begin{bmatrix} I_1^- \\ I_2^- \\ \vdots \\ I_i^- \\ \vdots \\ I_N^- \end{bmatrix} = \begin{bmatrix} S_{11} & S_{12} & \cdots & S_{1j} & \cdots & S_{1N} \\ S_{21} & S_{22} & \cdots & S_{2j} & \cdots & S_{2N} \\ \vdots & \vdots & & & \vdots & \vdots \\ S_{i1} & S_{i2} & & S_{ij} & \vdots & S_{iN} \\ \vdots & \vdots & & & \cdots & \vdots \\ S_{N1} & S_{N2} & \cdots & S_{Nj} & \cdots & S_{NN} \end{bmatrix} \begin{bmatrix} I_1^+ \\ I_2^+ \\ \vdots \\ I_i^+ \\ \vdots \\ I_N^+ \end{bmatrix} \tag{7.2}$$

or

$$\left[I^-\right] = [S]\left[I^+\right] \tag{7.3}$$

Accordingly, there is a number of N^2 of S parameters for a general N port network. In order to determine them, we excite each port, one at a time, by a delta gap voltage generator and determine the resulting incident and reflected waves on each port. Since

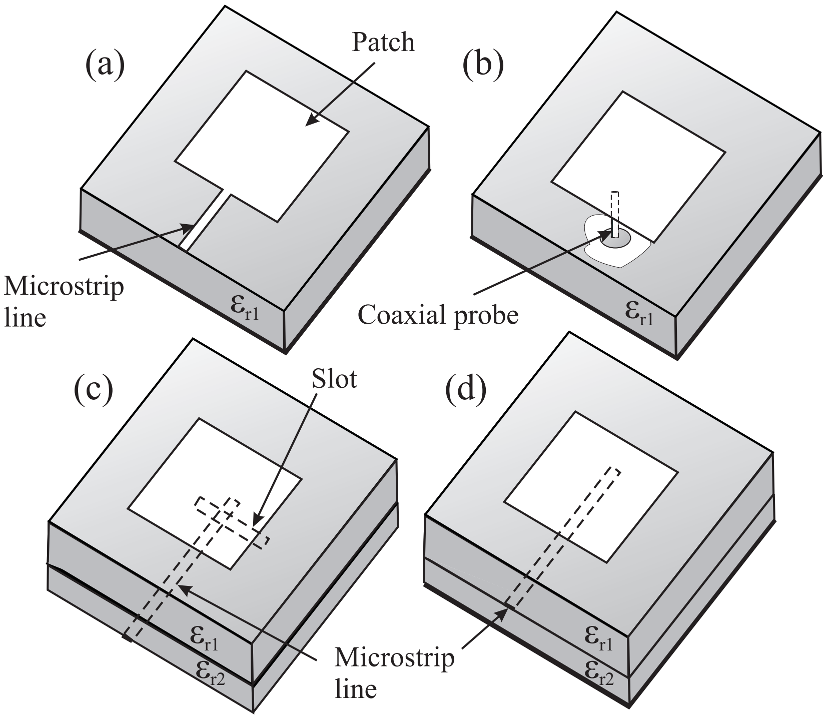
(a)
Patch
Microstrip line
ε_{r1}
(b)
Coaxial probe
ε_{r1}
(c)
Slot
ε_{r1}
ε_{r2}
Microstrip line
(d)
ε_{r1}
ε_{r2}

Fig. 7.2: *Common feeding techniques for patch antenna element (a) Direct excitation using microstrip line (b) Direct excitation using coaxial probe (c) Aperture coupling (d) Proximity coupling*

this process leads to N^2 equations of N^2 unknowns, the corresponding S parameters can be found simply by solving the set of equations. Although this method of determining S parameters is time-consuming and leads to unnecessary large matrix equations, we apply it here due to its simplicity.

7.1.3 Common feeding techniques

There are a few common feeding techniques widely used for exciting planar metal structures defined in stratified media. They are

- Direct excitation
- Aperture coupling
- Proximity coupling

Figure 7.2 illustrates these excitation methods when the excited planar structure is a simple patch antenna. Direct excitation can be done by using either a microstrip line or a coaxial probe. In our future discussions, we shall confine ourselves to microstrip line excitation because the complete structure can then be analyzed by the same methods described in the previous chapters. The extensions to other excitation methods are somewhat complex but mathematically viable.

7.2 Different De-embedding Techniques

The wave propagation along microstrip line is well characterized by the transmission line theory. The dominant mode that propagates along a microstrip line is quasi transverse electromagnetic (TEM). The higher order modes, for example transverse electric (TE) and transverse magnetic (TM) are less significant and are negligible for our purpose. However, the effect of these higher order modes may be significant in the vicinity of a discontinuity in the microstrip line, for example at the transition to a patch antenna or at the generator of the excited wave. It is also known that these higher order modes attenuate rapidly along the line and away from the discontinuity. Hence when de-embedding, the data should be acquired over a region where the effect of the higher order modes is negligible. In particular, when extracting scattering parameters the current density distributions are often calculated along an extended microstrip line. Such extensions increase the computational cost dramatically.

The choice of the de-embedding technique depends mostly on the excitation mechanism and the subsequent mathematical modeling. In order to limit the scope of the de-embedding process, we assume that the stratified configurations encountered here are solely excited by microstrip lines. In common usage, these microstrip lines are kept as close to the ground as possible and are excited by a coaxial line of the same characteristic impedance. Such constructions weaken impedance discontinuities at the excitation point, suppressing possible higher order modes. Therefore a current distribution on a microstrip feed line, sufficiently away from any potential discontinuities, forms a standing wave pattern of a TEM-like mode. Hence such a microstrip feedline can safely be modeled as an ideal transmission line of some proper characteristic impedance. It is already shown in [65], that the reflection coefficient along the microstrip line remains unchanged in amplitude and in phase when the coaxial line feed is modeled by a voltage gap generator and the microstrip line is open circuited at the excitation end.

Using the present MoM, the current standing wave pattern (CSWP) along the microstrip line can easily be determined. For example, Figure 7.3 illustrates the normalized CSWP of a microstrip line fed by voltage gap generator. Here, the width and the length of the line are assumed to be 0.223 cm and 16.04 cm respectively. The dielectric constant of the layer is chosen as 2.55. The operational frequency is fixed at 2.30 GHz. Such patterns can be used to determine the necessary scattering parameters of the stratified structure. Since the S parameters are defined in terms of incident and reflected waves as in (7.1), a method is needed to extract the corresponding amplitude and phase of these wave components from the CSWP. A few different methods are available for this purpose.

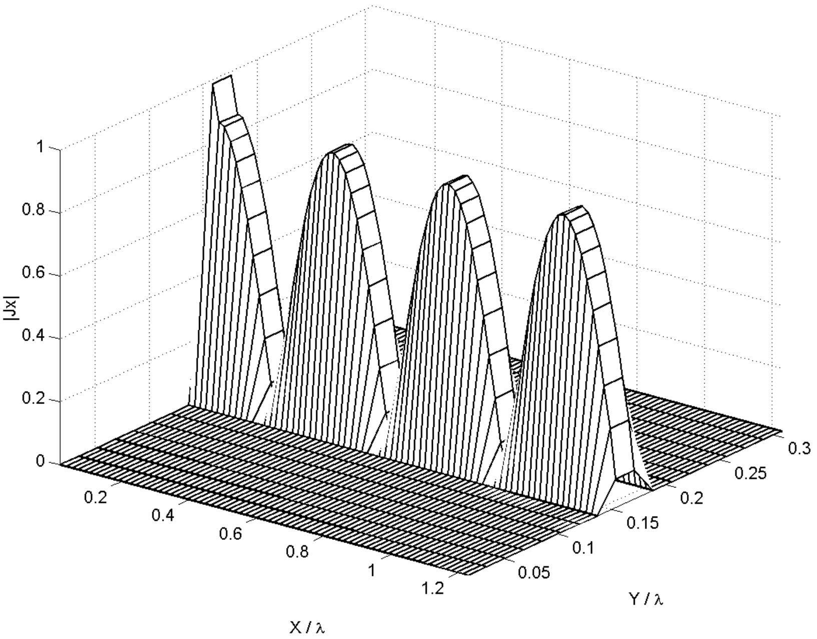

Fig. 7.3: *The normalized current standing wave pattern of a micostrip line of width 0.223 cm and length 16.04 cm. The dielectric constant is 2.55 and operational frequency is 2.30 GHz. λ denotes the wavelength in free space*

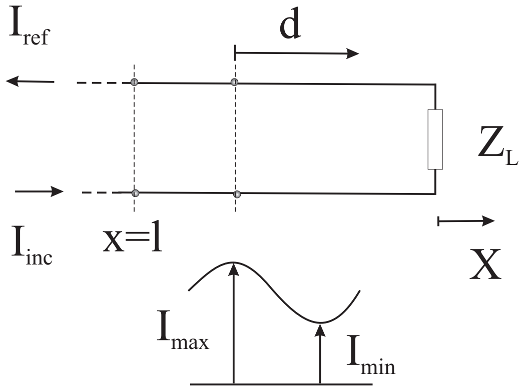

Fig. 7.4: *Current wave propagation in a transmission line terminated by impedance Z_L*

7.2.1 A method based on transmission line theory

Although it is more common in scientific literature on transmission line theory to work with voltage waves, we shall here proceed with current waves instead. This is due to the fact that the outcome of the MoM is inherently a current density distribution. According to the notation given in Fig. 7.4, the current on an ideal lossless transmission line is expressed as [64]

$$I(l) = I_{inc}\exp(-j\beta l) - I_{ref}\exp(j\beta l) \tag{7.4}$$

where

$I(l)$ is the longitudinal component of the current at $x = l$,

β is the propagation constant of the fundamental TEM mode along the line,

l denotes the longitudinal coordinate along the line such that $l = 0$ corresponds to the position of the load Z_L and

I_{inc} and I_{ref} are the complex amplitudes of the incident and reflected current waves at the load Z_L respectively.

The reflection coefficient Γ or equivalently S_{11}, at Z_L is defined as

$$\Gamma = \frac{I_{ref}}{I_{inc}} \tag{7.5}$$

Let us denote the maximum and minimum value of the CSWP as $I_{\max}$ and $I_{\min}$ respectively. Then the current standing wave ratio (CSWR) [64]

$$CSWR = \frac{I_{\max}}{I_{\min}} \tag{7.6}$$

The amplitude of the reflection coefficient Γ is then related to CSWR by [66]

$$|\Gamma| = \frac{CSWR - 1}{CSWR + 1} \tag{7.7}$$

The reflection coefficient Γ at the point located a distance d away from the above considered maximum and towards the load, can be expressed as [64]

$$\Gamma(d) = |\Gamma|\frac{\exp(j\beta d)}{\exp(-j\beta d)} = |\Gamma|\exp(2j\beta d) \tag{7.8}$$

The corresponding impedance Z at the same point is then given by [64]

$$Z(d) = \frac{1+\Gamma}{1-\Gamma}Z_0 = \frac{1+|\Gamma|\exp(2j\beta d)}{1-|\Gamma|\exp(2j\beta d)}Z_0 \tag{7.9}$$

where Z_0 is the characteristic impedance of the transmission line.

Although the previous method based on transmission line theory is simple, it calculates $|\Gamma|$ based on only two discrete values of the derived CSWP, namely $I_{\max}$ and $I_{\min}$. Therefore the result is prone to considerable computational errors. Such errors can be reduced if one uses more points on CSWP in determining $I_{\max}$ and $I_{\min}$ (or alternatively I_{inc} and I_{ref}). The following methods exploit the complete CSWP when evaluating I_{inc} and I_{ref}.

7.2.2 A method based on Prony's method

In chapter 3, Prony's method has been suggested for extracting exponential functions from spectral Green's functions. A very similar and straightforward method can be adapted here for extracting incident and reflected current waves from the corresponding CSWP.

7.2.3 A method based on GPOF method

The generalized pencil of function (GPOF) method described in chapter 3, presents a more robust approach for extracting exponential functions and their amplitudes from a given data set. An analogous approach can also be adapted here for extracting amplitudes I_{ref} and I_{inc} from CSWP.

Since the incident and reflected waves represent two waves traveling in opposite directions along the same microstrip line, the corresponding exponential functions should have equal magnitudes but opposite signs in the imaginary parts of their arguments, i.e. the arguments of these exponential functions should ideally be complex conjugates. Although the method based on transmission line theory explicitly assumes this, both Prony's and GPOF methods independently determine the two exponential functions thus providing an additional mechanism for verifying their accuracy. The degree of equality possessed by the magnitude of the arguments of these two exponential functions, is a measure of the numerical accuracy of the respective method. We shall henceforth utilize the rather robust GPOF based method for determining S parameters from CSWP.

7.2.4 Example 1: Microstrip patch antenna

We shall now determine the reflection coefficient at the input of the patch antenna outlined in Fig. 7.5. This is the same as S parameter S_{11} for one port network. This patch has been studied in [8] and [67], and the measured S parameters are also available. Figure 7.6 compares S_{11} found by the current method, where we use space domain MoM for determining induced current densities and GPOF technique for de-embedding, with the measured results in [8]. In addition, the commercially available software, Agilent Momentum, which is a subsystem of Advanced Design System 2002, has also been used to analyze the same patch structure. Figure 7.6 shows that both simulation results are in fair agreement with the measured values. The minor deviations between the measured and the simulated values may be due to the approximated dimensions used in the simulations in order to match the structure with a proper discretization. It is also obvious that the present antenna is far from being optimum with respect to the impedance match between the feed line and the patch. Moreover, figures 7.7 - 7.9 show the normalized magnitude of the x-current density, the y-current density and the total current density on the patch at the operating frequency of 2.30 GHz.

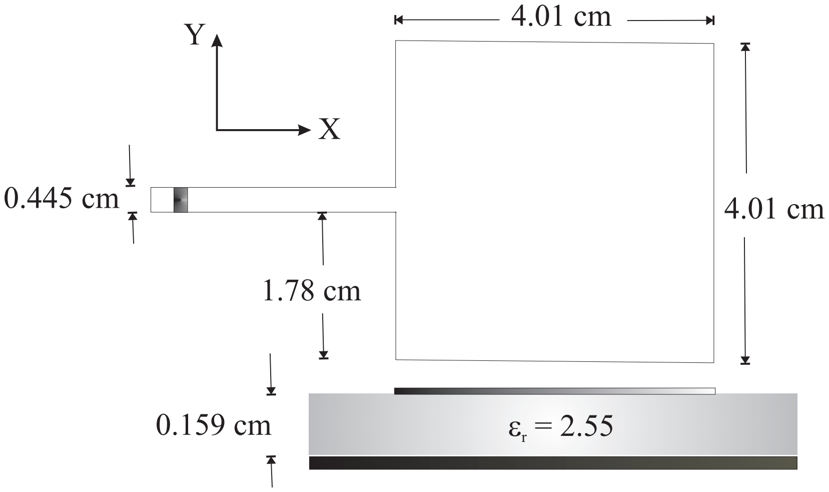
4.01 cm
Y
X
0.445 cm
4.01 cm
1.78 cm
0.159 cm
$\varepsilon_r = 2.55$

Fig. 7.5: *Stand alone patch antenna*

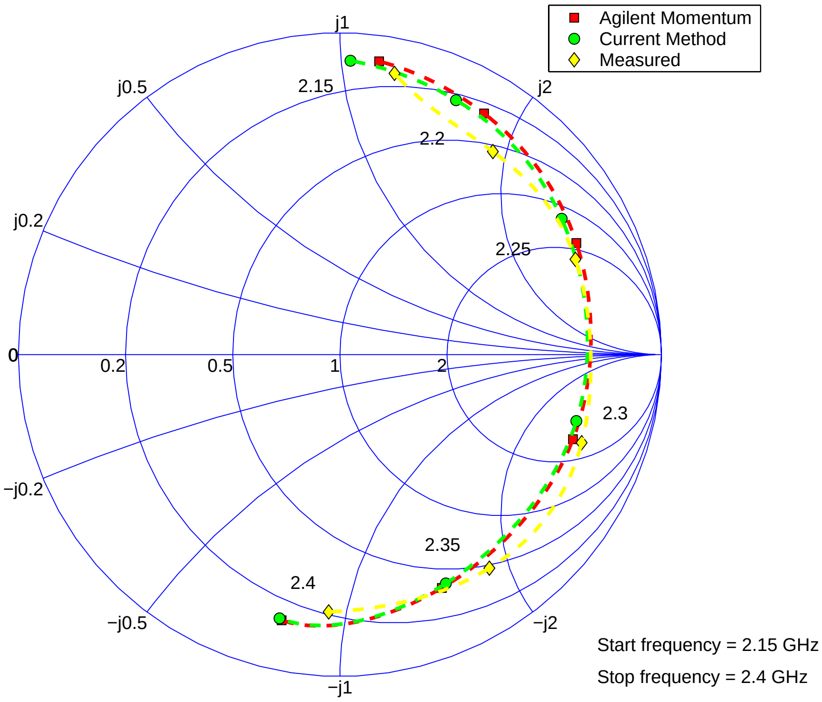

Fig. 7.6: *Comparison of S_{11} obtained for the single patch antenna in Fig. 7.5 using both the current method and Agilent Momentum, with the measured values from [8]*

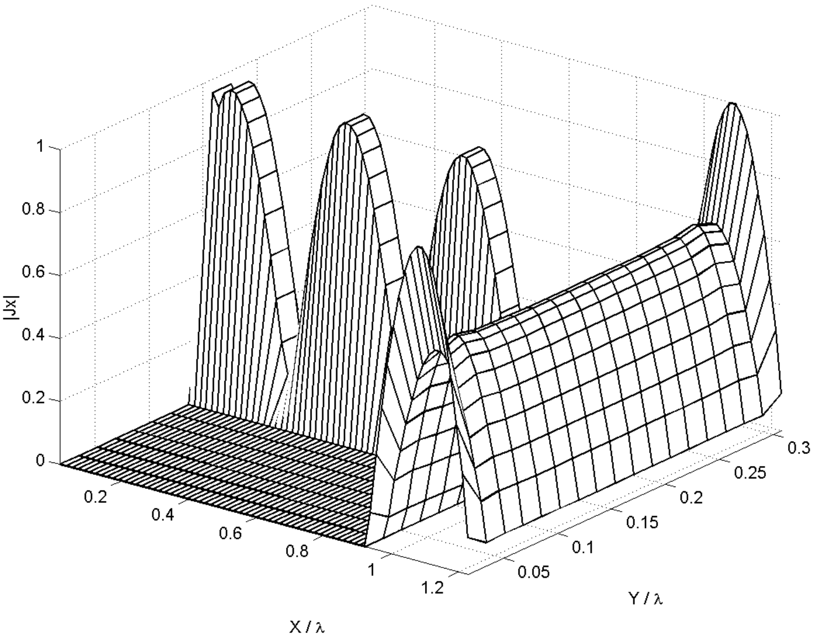

Fig. 7.7: *Normalized magnitude of the induced x-current density of the patch antenna in Fig. 7.5 at the frequency of 2.30 GHz*

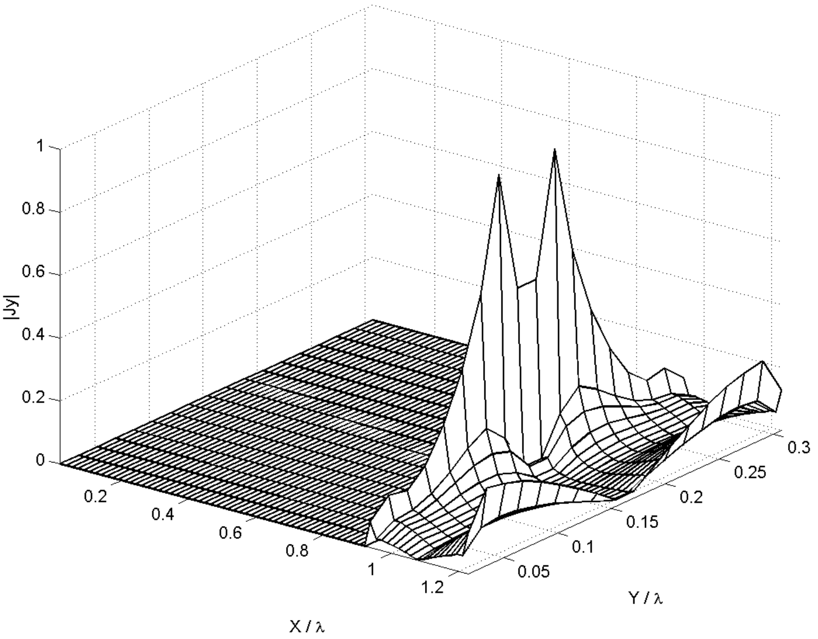

Fig. 7.8: *Normalized magnitude of the induced y-current density of the patch antenna in Fig. 7.5 at the frequency of 2.30 GHz*

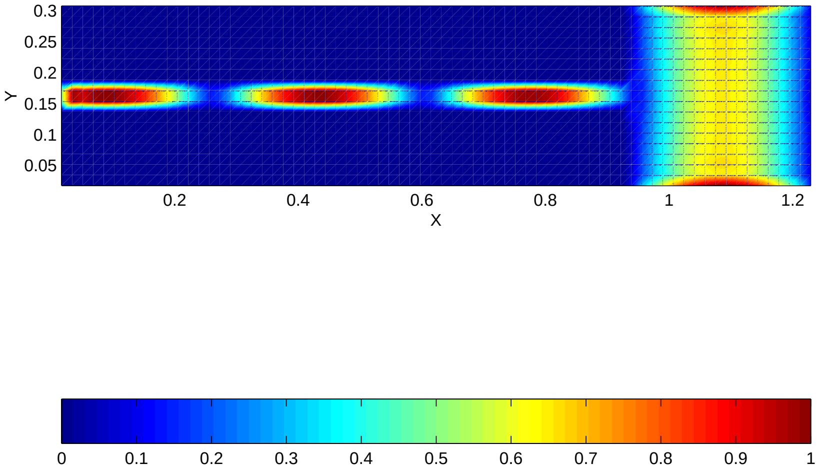

Fig. 7.9: *Normalized magnitude of the total induced current density of the patch antenna in Fig. 7.5 at the frequency of 2.30 GHz*

7.2.5 Example 2 : Two patches close to each other

A simple array consisting of two equivalent patches located close to each other is also simulated. Two patches are etched adjacent to each other as shown in Fig. 7.10. The distance between the two patches is 0.223 cm. S parameters for this structure are determined using the present method and the Agilent Momentum. They are compared in Fig. 7.11 and 7.12. The measured results for this construction are not available. However, we can see from the S parameter plots that the results acquired by the current method are almost equivalent to the results from the Agilent Momentum. The corresponding induced current densities at 2.30 GHz are also shown in Fig. 7.13 - 7.15.

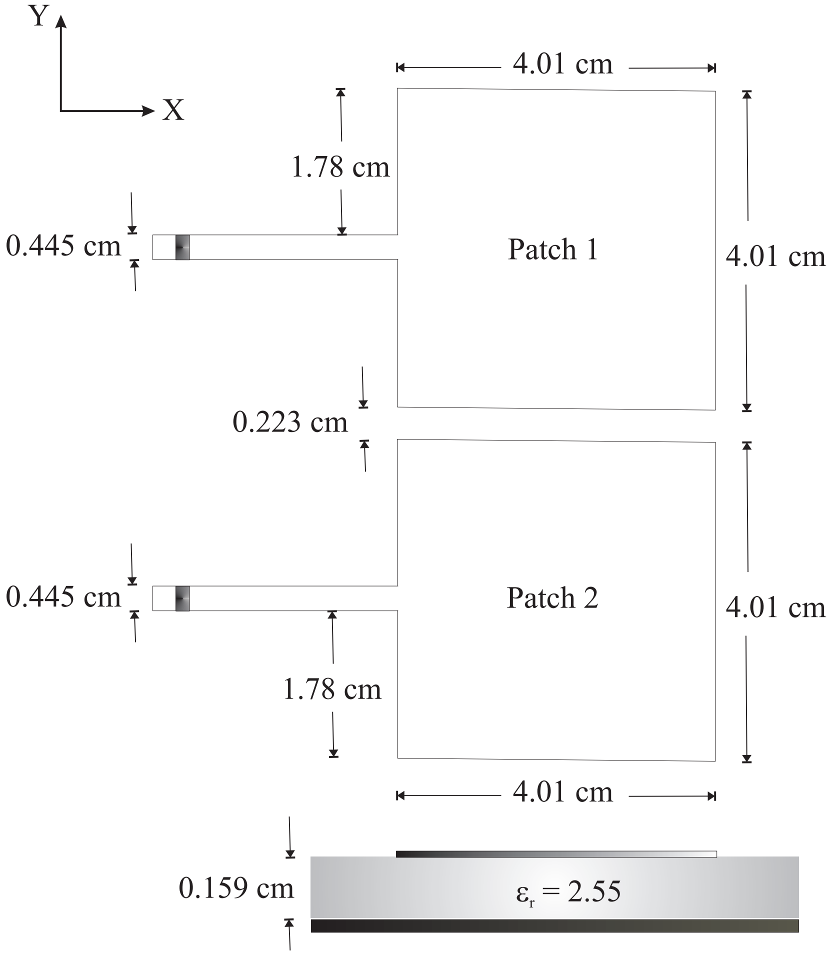
Y
X
4.01 cm
1.78 cm
0.445 cm
Patch 1
4.01 cm
0.223 cm
0.445 cm
Patch 2
4.01 cm
1.78 cm
4.01 cm
0.159 cm
$\varepsilon_r = 2.55$

Fig. 7.10: *Two equivalent patches placed side by side*

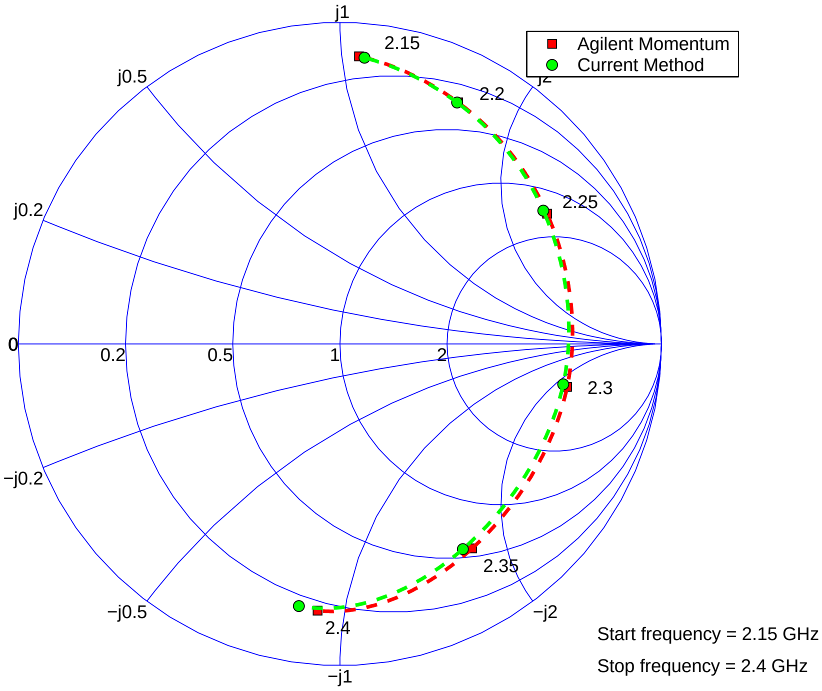

Fig. 7.11: *Comparison of S_{11} (or S_{22}) obtained by the current method and the Agilent momentum for the two patches in Fig. 7.10*

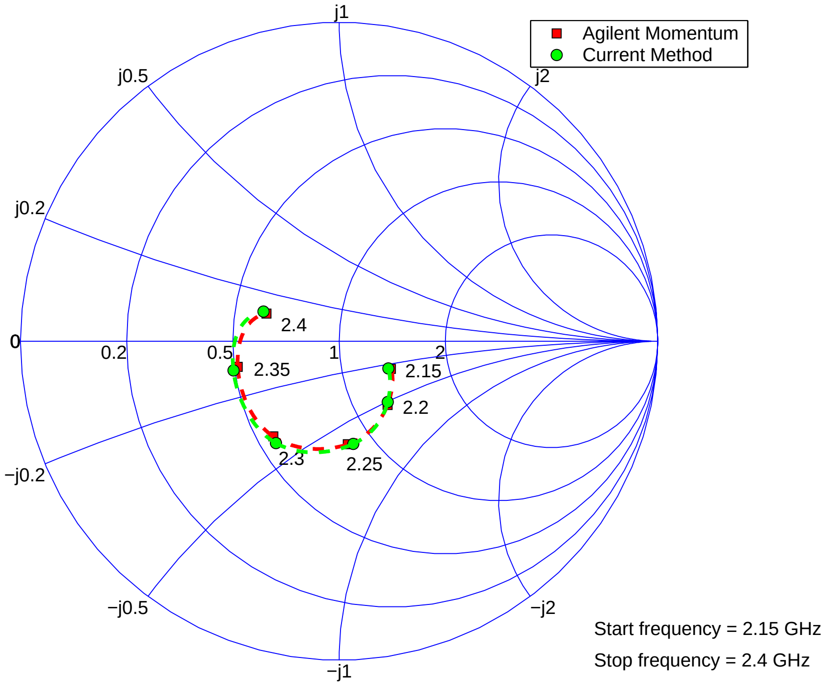

Fig. 7.12: *Comparison of S_{12} (or S_{21}) obtained by the current method and the Agilent momentum for the two patches in Fig. 7.10*

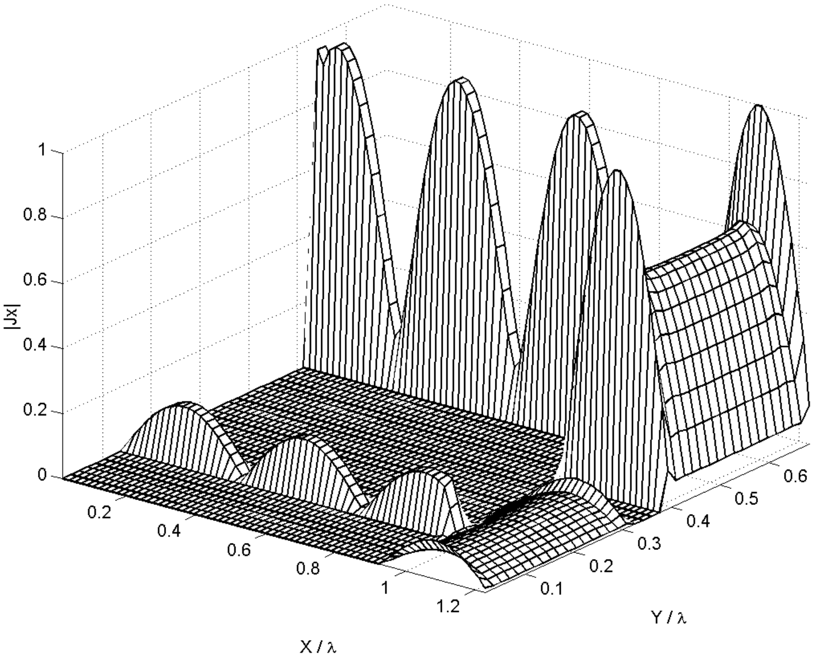

Fig. 7.13: *Normalized magnitude of the induced x-current density of the two patches in Fig. 7.10 when only patch 1 is excited (The frequency equals to 2.30 GHz)*

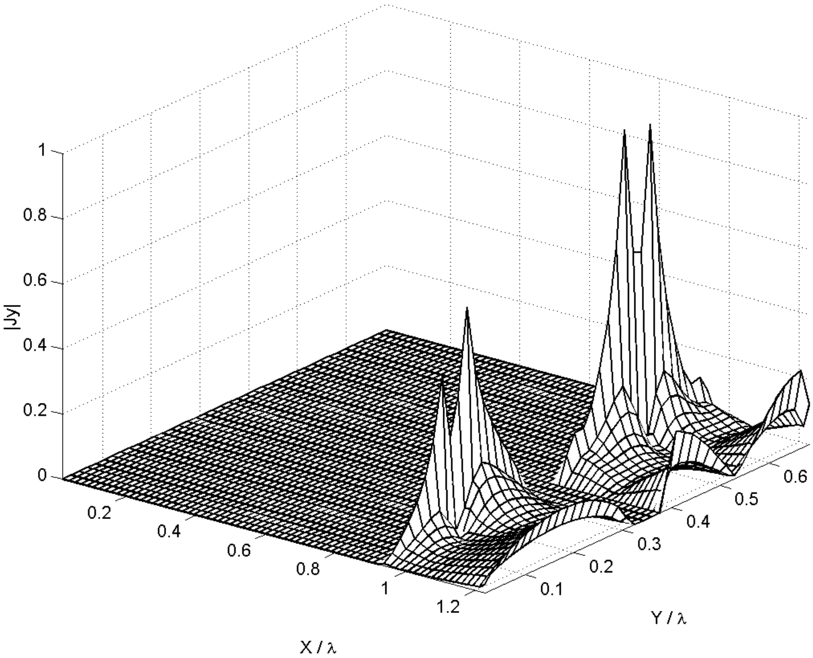

Fig. 7.14: *Normalized magnitude of the induced y-current density of the two patches in Fig. 7.10 when only patch 1 is excited (The frequency equals to 2.30 GHz)*

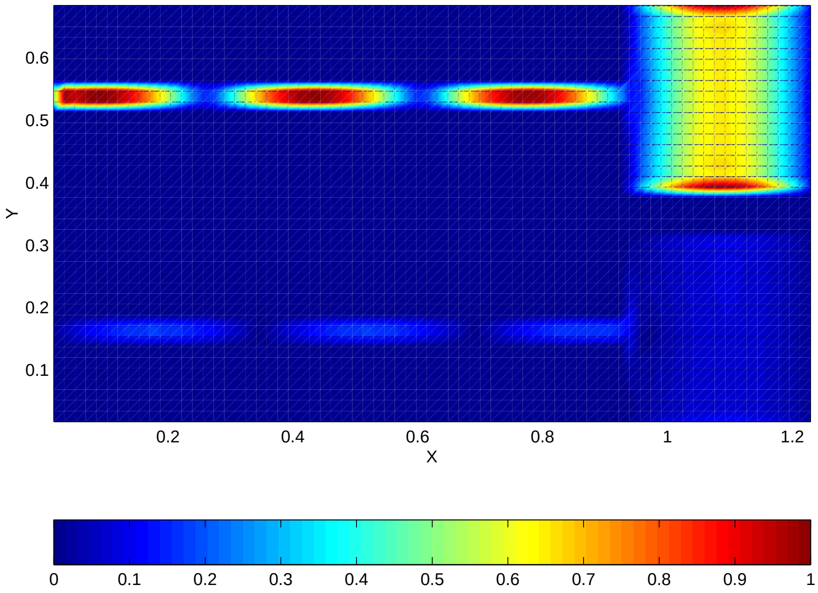

Fig. 7.15: *Normalized magnitude of the total induced current density of the two patches in Fig. 7.10 when only patch 1 is excited (The frequency equals to 2.30 GHz)*

Chapter 8

Results

8.1 Introduction

This chapter presents a few sample results obtained by the current method. The results are twofold.

- Application to linear patch antenna array consisting of three patches etched on a single dielectric layer
- Application to finite frequency selective surface (FSS)

The above examples are chosen due to their simplicity and easy-to-verify nature. Since the current method does not impose any constraint on the shape of the metallic structure, other than that it is planar, analysis of intricate structures is possible with the present codes. Since the codes are written only to implement the method and to verify the current approach with simple algorithms, the intention of this chapter is only to affirm their accuracy rather than to prove their efficiency over commercially available software.

8.2 Application to Linear Patch Antenna Array

8.2.1 Stand alone patch antenna with inset microstrip line feed

A stand alone rectangular patch antenna fed by a microstrip line was first designed. It was etched on a simple dielectric layer of Rogers RT/duroid 5880. The dielectric constant, loss tangent and thickness of the substrate are given as 2.2, 0.0009 and 0.381 mm (15 mil) respectively. In order to match the characteristic impedance of the microstrip line to the impedance seen by the microstrip line, the microstrip line was inset as shown in Fig. 8.1. The dimensions of the structure were determined using mathematical formulas in [42] and other commercial software. A long stripline feed was purposely selected to facilitate the accurate extraction of S parameters during the simulations.

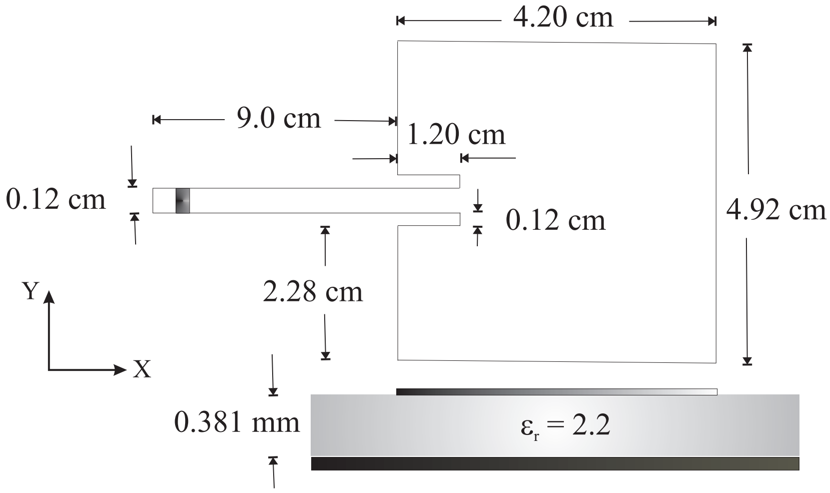

Fig. 8.1: *Layout of the patch antenna fed by microstrip line*

Simulated and measured results

This single patch was analyzed with the present method in the frequency range from 2.35 GHz to 2.45 GHz. This patch was then etched on 15 cm by 13.5 cm Rogers RT/duroid 5880 plate (Fig. 8.2). The reflection coefficient, equivalently S_{11}, was measured in an anechoic chamber using the network analyzer HP8720C. Figure 8.3 compares the measured results with the simulated results. The measurements show a good agreement with the simulated results. The simulated resonant frequency deviates less than 1 percent from the measured resonant frequency. In addition, the x-, y- and total current density distributions at the frequency 2.40 GHz are also given in Fig. 8.4 - 8.6.

8.2.2 Linear antenna array consisting of three patches

Simulated and measured results

A linear array consisting of three equivalent patches in Fig. 8.1 was designed (Fig. 8.7). Their mutual coupling coefficients and reflection coefficients were determined in the frequency range from 2.35 GHz to 2.45 GHz using the present method. When the port feeding patch 1 is excited by a delta gap voltage generator, the resulting x-, y- and total current density distributions at frequency 2.4 GHz are given in Fig. 8.9 - 8.11. Moreover, the same configuration was simulated using Momentum, which is a part of the commercial software package ADS (Advanced Design System).

The linear patch array was etched on 27.5 cm by 14.2 cm Rogers RT/duroid 5880 plate (Fig. 8.8). The S_{11}, S_{22} and S_{33} were measured in an anechoic chamber using the network analyzer HP8720C. The ports which were not connected to probes were terminated with 50 Ω. The measured S-parameters together with the corresponding simulated S parameters, both using the present method and Momentum, are plotted in Fig. 8.12 - 8.14. Likewise,

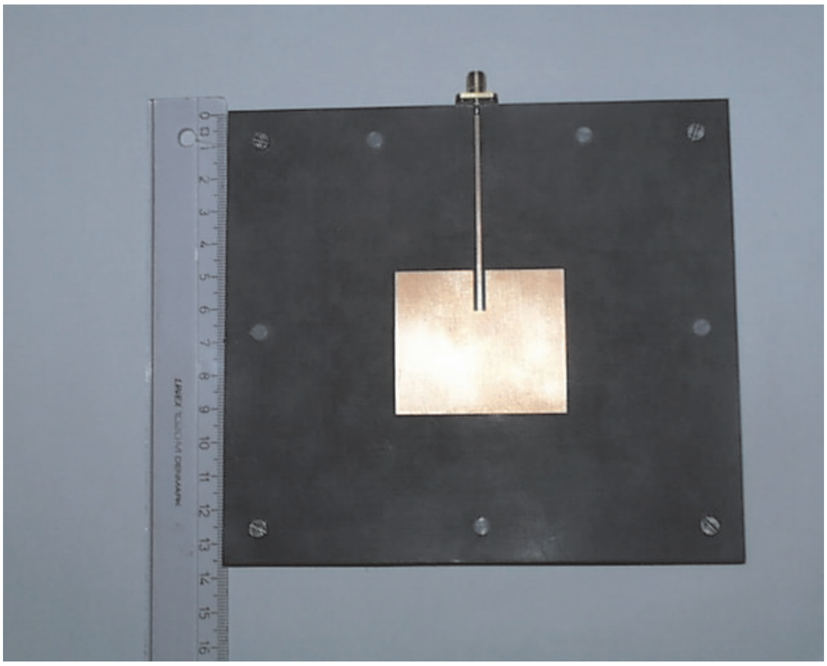

Fig. 8.2: *Prototyped inset patch antenna in Fig. 8.1*

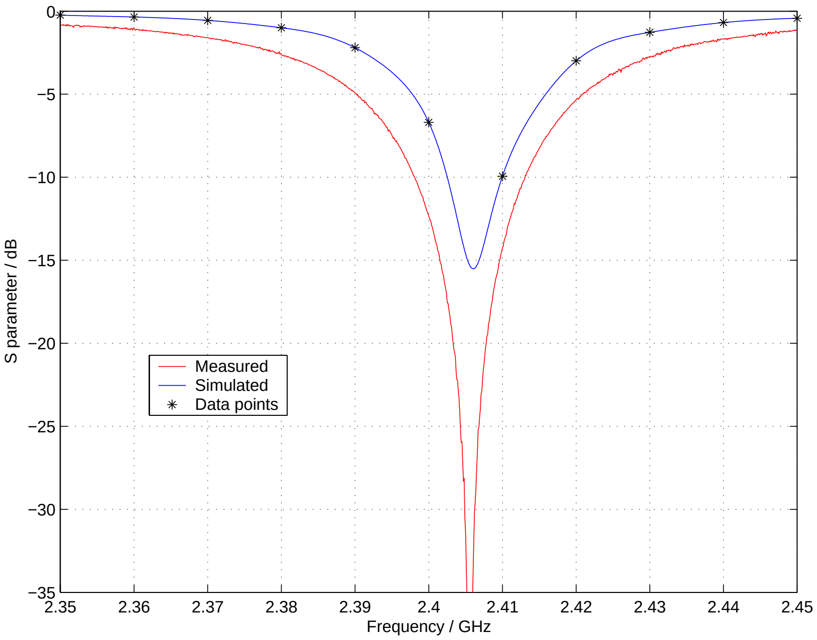

Fig. 8.3: *Measured and simulated reflection coefficient* (S_{11}) *of the stand alone patch shown in Fig. 8.1*

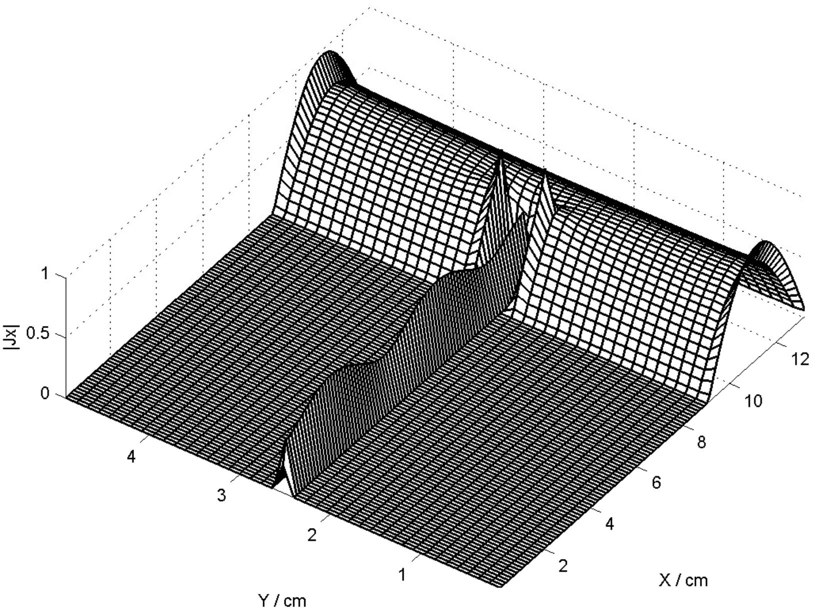

Fig. 8.4: *Converged x-directed surface current density on the stand alone inset patch in Fig. 8.1 at the frequency 2.40 GHz*

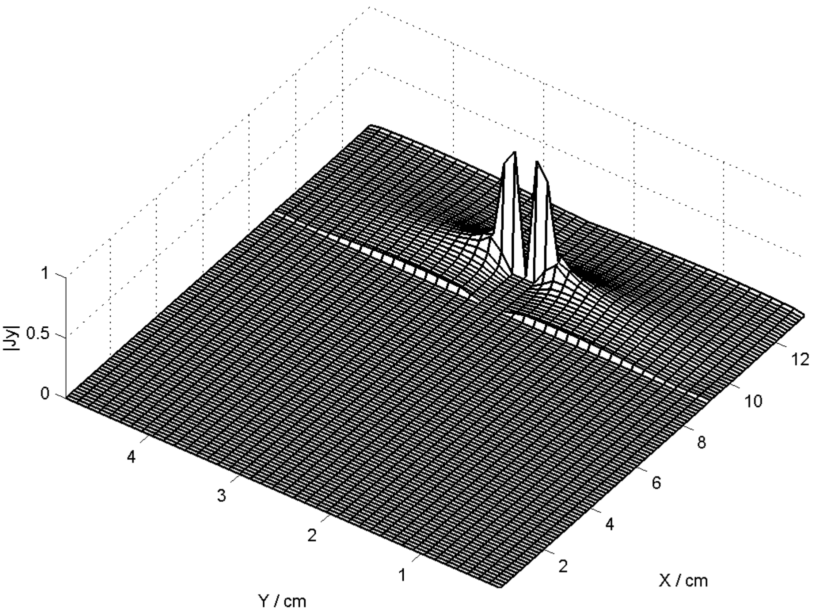

Fig. 8.5: *Converged y-directed surface current density on the stand alone patch in Fig. 8.1 at the frequency 2.40 GHz*

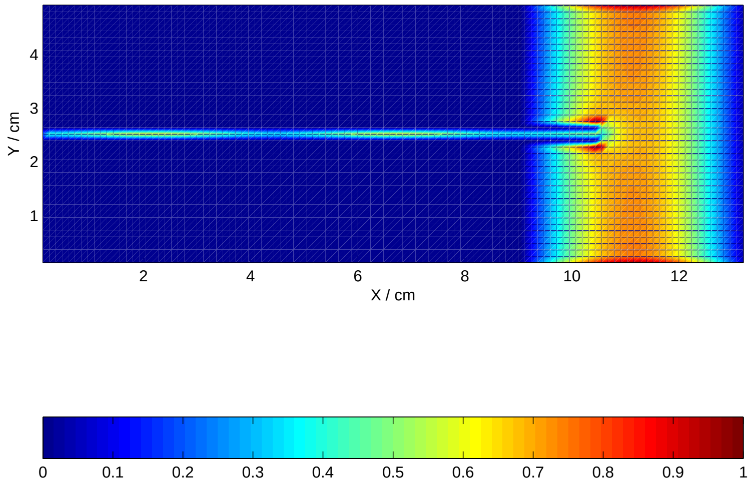

Fig. 8.6: *Converged total surface current density on the stand alone patch in Fig. 8.1 at the frequency 2.40 GHz*

the measured S_{12}, S_{13} and S_{23} together with simulated results are shown in Fig. 8.12 - 8.14. Again, the measurements of reflection coefficients, i.e. S_{11}, S_{22} and S_{33}, show a good agreement with the simulated results. However, the simulated mutual coefficients, i.e. S_{12}, S_{13} and S_{23}, both from the present method and Momentum, show a few decibel deviation at the resonant frequency. Though we can not pin-point the exact reasons for such deviation, the finite nature of the substrate, the loss due to port contacts and feed lines, and the change in properties of the substrate from specified values, may contribute significantly.

8.3 Application to Finite Frequency Selective Surfaces

8.3.1 Introduction

Frequency selective surfaces (FSS) typically consist of either a periodic array with arbitrarily shaped conductors or a periodic array with arbitrarily shaped apertures. The former type is known as normal type whereas the later as inverse type. Both types are often backed by one or several dielectric layers. FSSs are bandpass or bandstop filters of electromagnetic waves and useful for efficient use of the frequency spectrum. Their spectral responses depend on element configuration, element spacing and characteristics of the dielectric layer, if there is any. FSS are used in, for example, hybrid radomes, dichroic reflectors, circuit analog absorbers, polarizers, etc. [68]

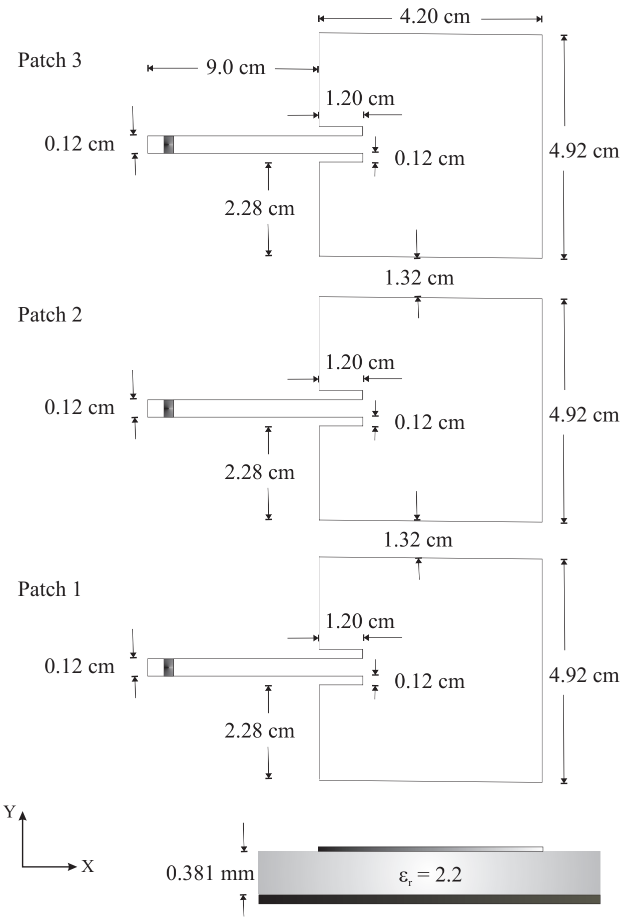
4.20 cm
Patch 3
9.0 cm
1.20 cm
0.12 cm
0.12 cm
4.92 cm
2.28 cm
1.32 cm
Patch 2
1.20 cm
0.12 cm
0.12 cm
4.92 cm
2.28 cm
1.32 cm
Patch 1
1.20 cm
0.12 cm
0.12 cm
4.92 cm
2.28 cm
Y
X
0.381 mm
ε_r = 2.2

Fig. 8.7: *Layout of the linear array consisting of three equivalent patches*

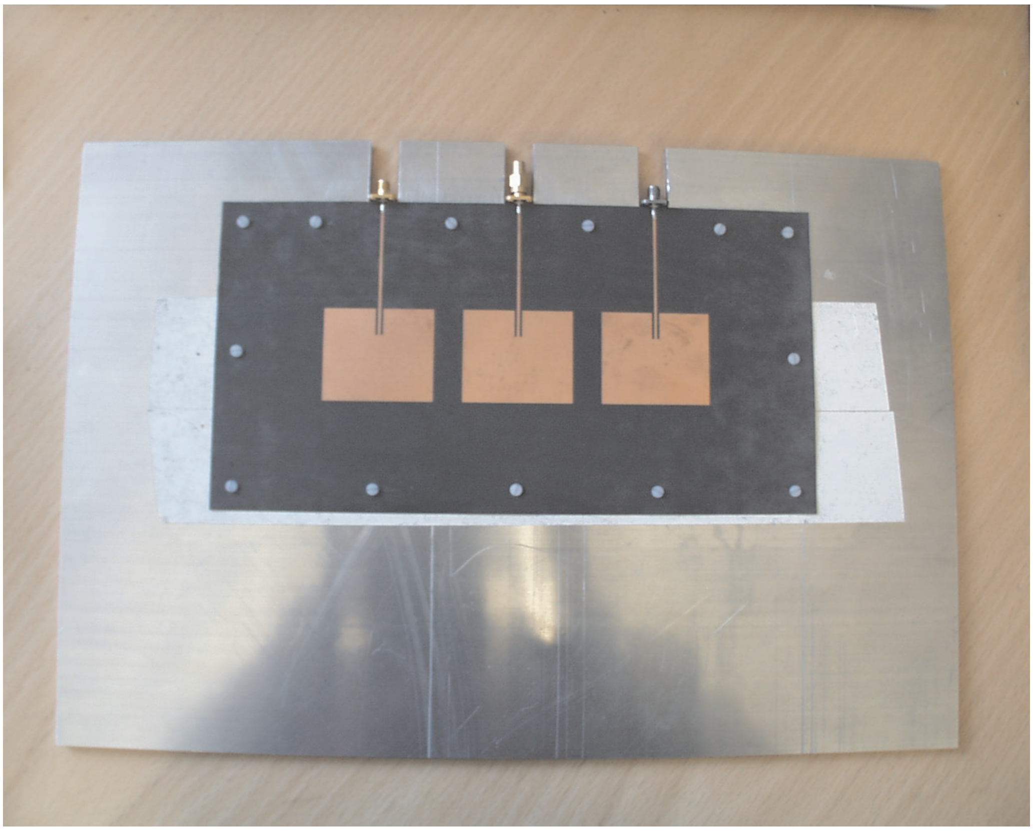

Fig. 8.8: *Prototyped linear patch array in Fig. 8.7*

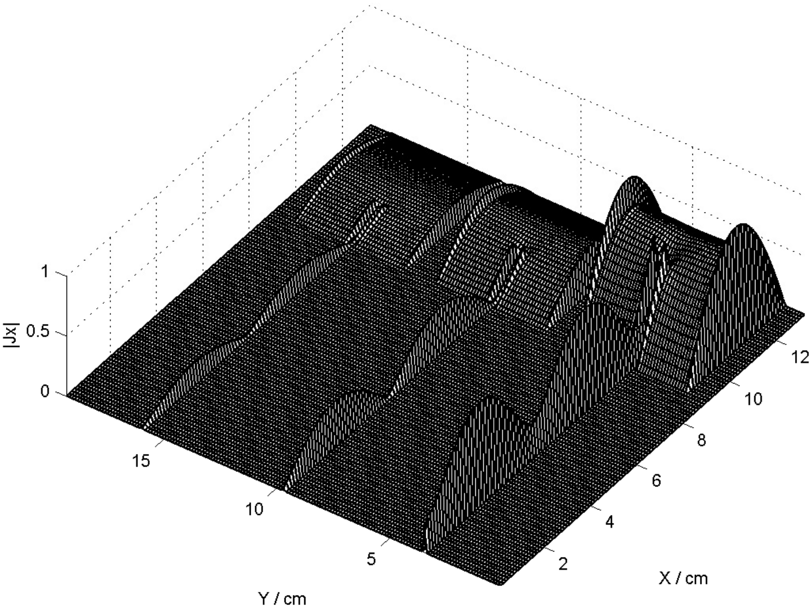

Fig. 8.9: *Converged x-directed surface current density on the linear patch array shown in Fig. 8.7 at the frequency 2.40 GHz*

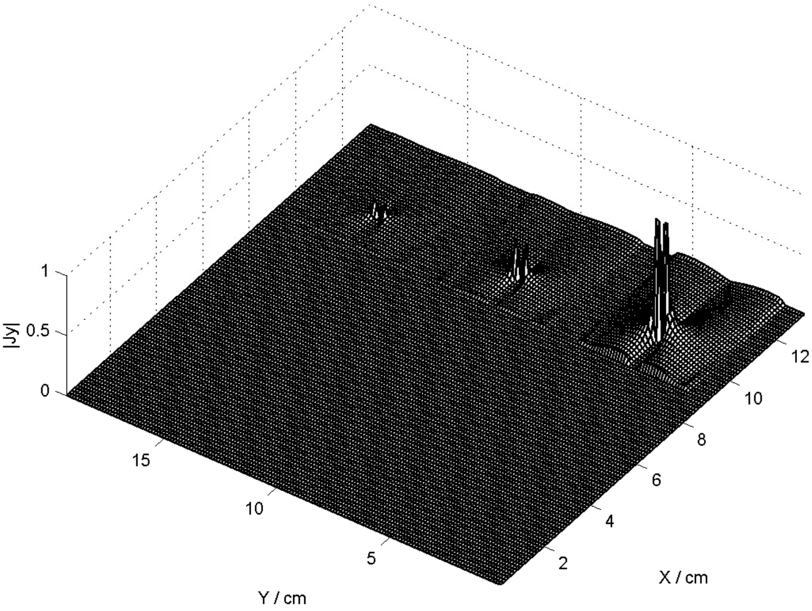

Fig. 8.10: *Converged y-directed surface current density on the linear patch array shown in Fig. 8.7 at the frequency 2.40 GHz*

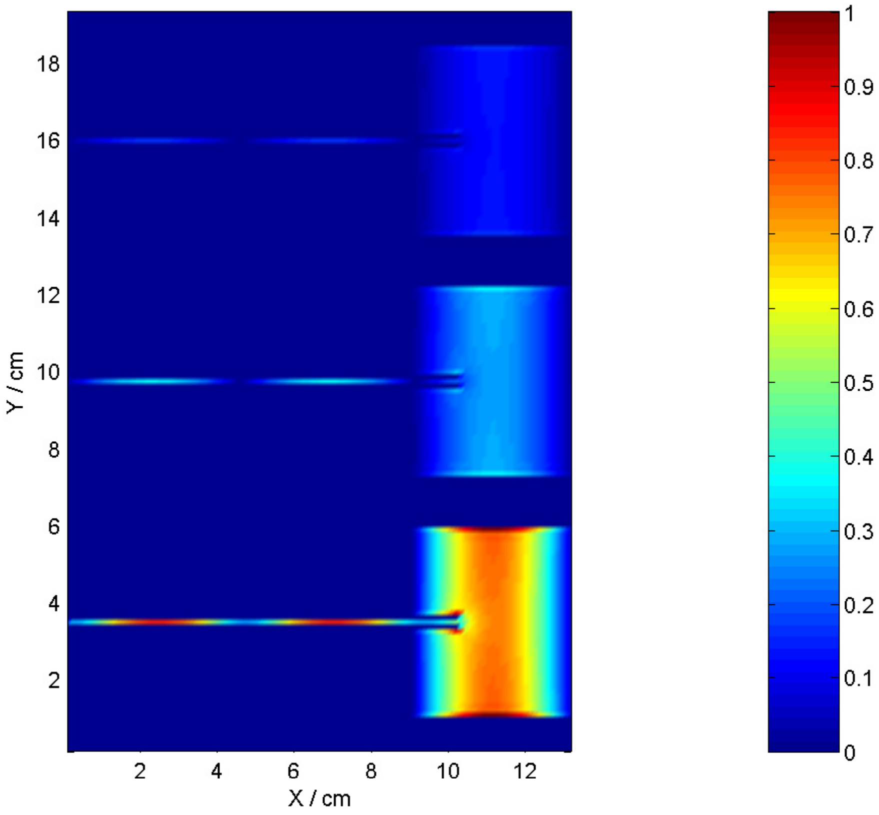

Fig. 8.11: *Converged total surface current density on the linear patch array shown in Fig. 8.7 at the frequency 2.40 GHz*

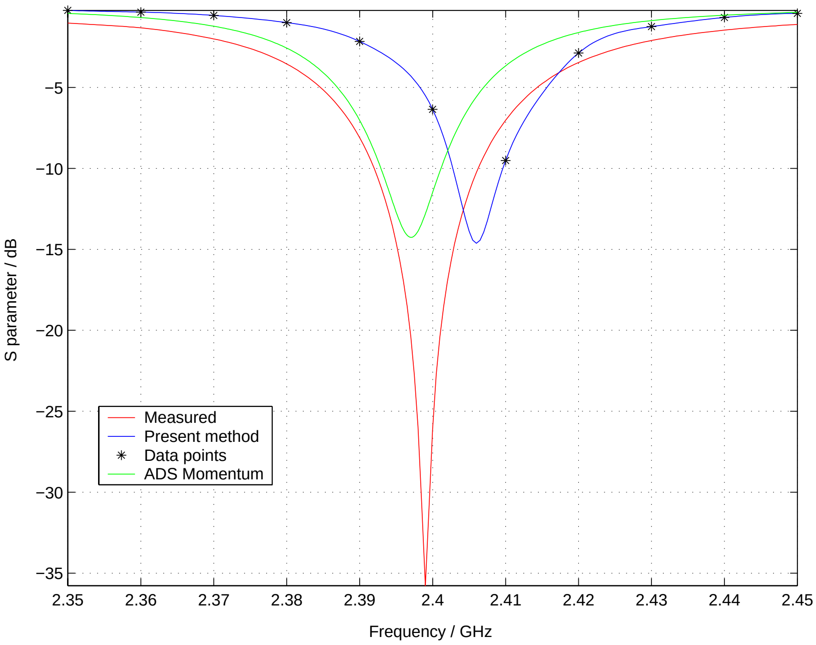

Fig. 8.12: *Measured and simulated reflection coefficient* S_{11} *of the linear patch array in Fig. 8.7*

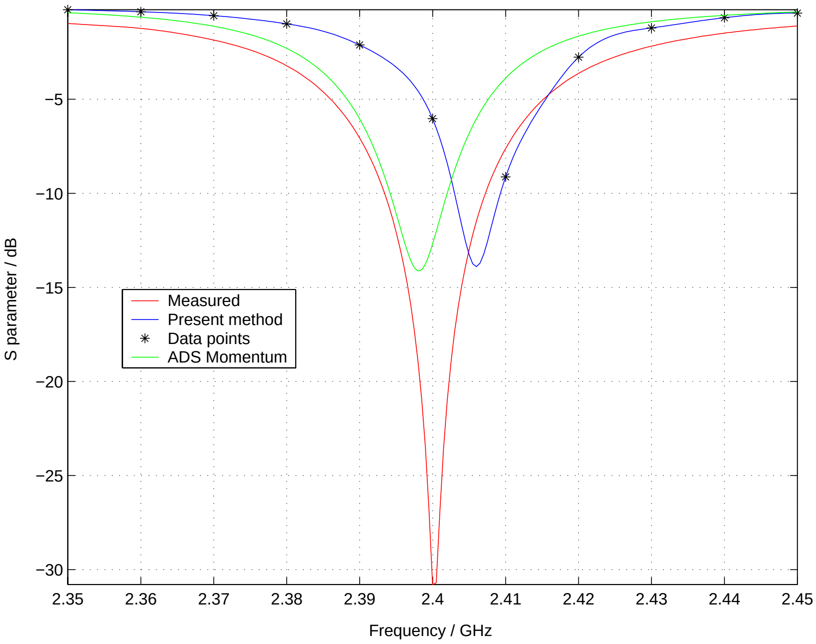

Fig. 8.13: *Measured and simulated reflection coefficient* S_{22} *of the linear patch array in Fig. 8.7*

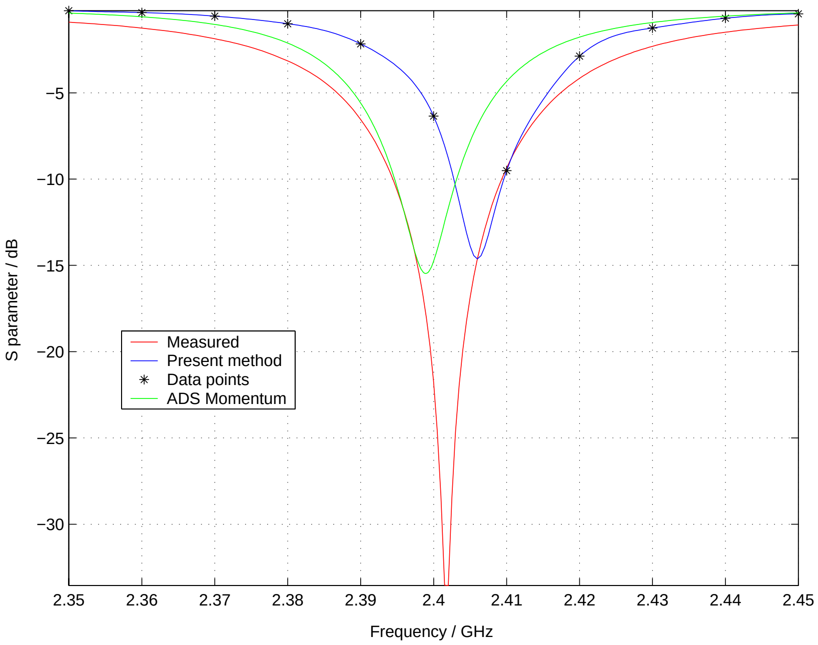

Fig. 8.14: *Measured and simulated reflection coefficient S_{33} of the linear patch array in Fig. 8.7*

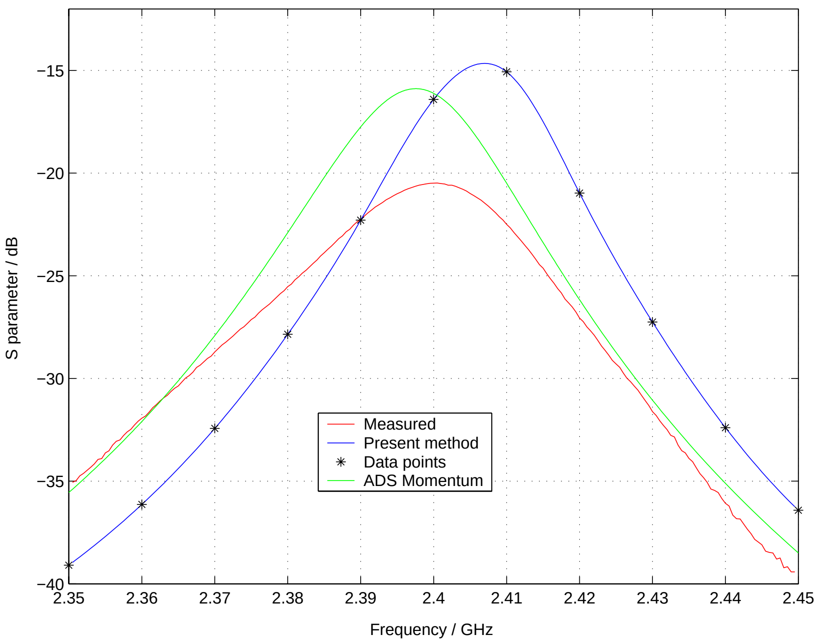

Fig. 8.15: *Measured and simulated mutual coupling coefficient S_{12} of the linear patch array in Fig. 8.7*

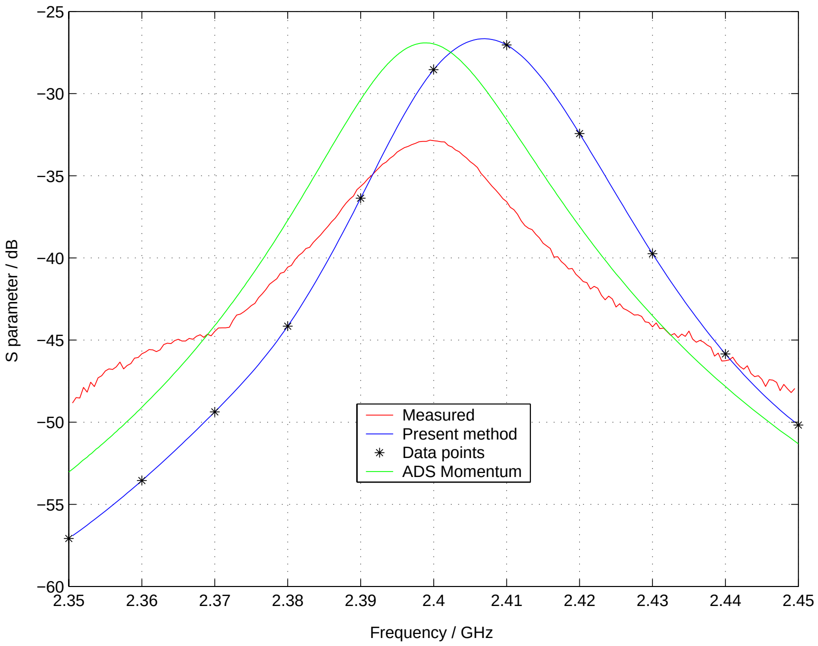

Fig. 8.16: *Measured and simulated mutual coupling coefficient S_{13} of the linear patch array in Fig. 8.7*

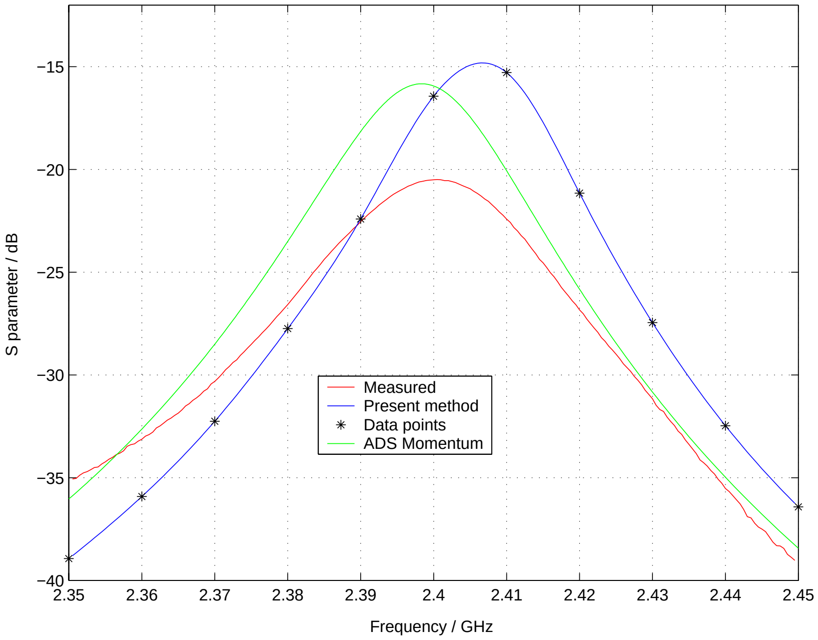

Fig. 8.17: *Measured and simulated mutual coupling coefficient S_{23} of the linear patch array in Fig. 8.7*

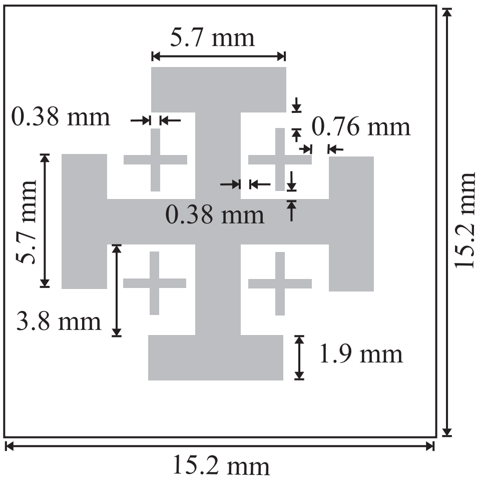

Fig. 8.18: *The layout of the loaded Jerusalem cross [69]*

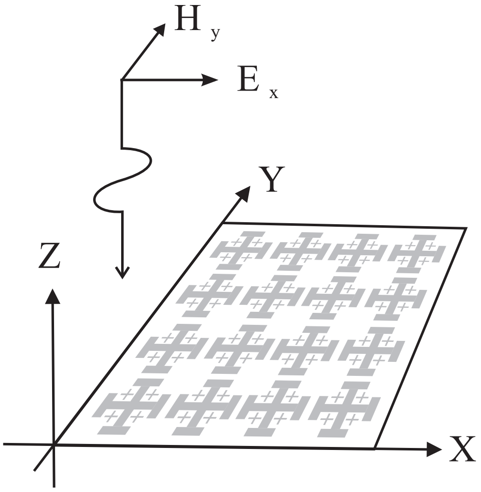

Fig. 8.19: *A plane wave incident on an array of Jerusalem crosses*

8.3.2 Element structure : Jerusalem cross

The geometric shape of the element is utmost important in designing a proper FSS. Fortunately, there are myriads of types of elements available to the designer. We shall in our analysis confine ourselves to a rather complicated geometry known as Jerusalem cross. The loaded version of the Jerusalem cross is shown in Fig. 8.18.

Free standing Jerusalem cross

A free standing loaded Jerusalem cross shown is in Fig. 8.18. It is analyzed when a perpendicularly incident plane wave is scattered from it (Fig. 8.19). The dimensions of the Jerusalem cross are selected following [69], so that the results acquired here can be easily verified. A single cross is first analyzed at 8 GHz applying the grid shown in Fig 8.20. The resulting normalized x-, y- and total current densities are illustrated in Fig. 8.21 - 8.23.

Two configurations of finite arrays of free standing Jerusalem crosses are next simulated: an array of four by four elements and an array of eight by eight elements. Their scattered fields in the direction of incidence, as a function of frequency are calculated based on the induced surface current densities acquired by the present method. Figure 8.24 shows the normalized magnitude of the scattered field in the direction of incidence as a function of frequency for the four by four array. It illustrates that the scattering in the direction of incidence is maximum around 8.2 GHz. The corresponding total surface current densities at 6 GHz, 8 GHz and 10 GHz are shown in Fig 8.25, 8.26 and 8.27 respectively. They illustrate the existence of different types of current modes at these frequencies [68].

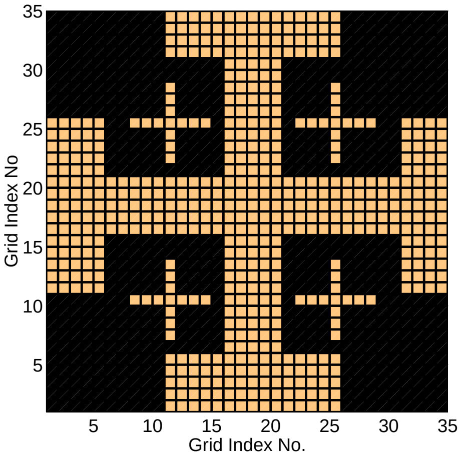
Grid Index No
Grid Index No.
35
30
25
20
15
10
5
5
10
15
20
25
30
35

Fig. 8.20: *Grid applied for a loaded Jerusalem cross*

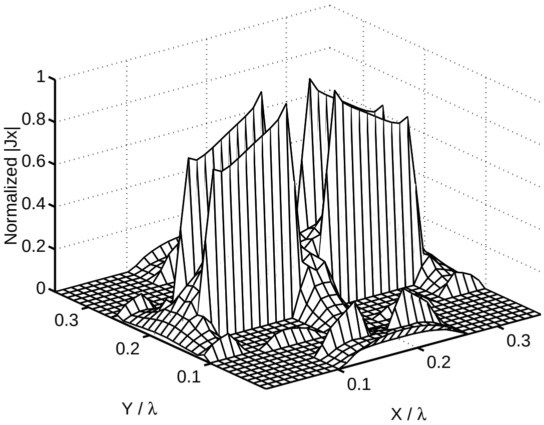

Fig. 8.21: *Normalized x directed surface current density at 8 GHz*

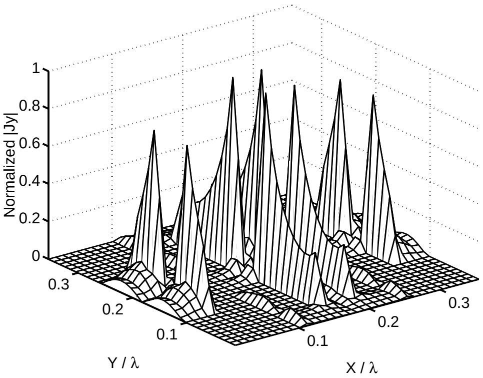

Fig. 8.22: *Normalized y directed surface current density at 8 GHz*

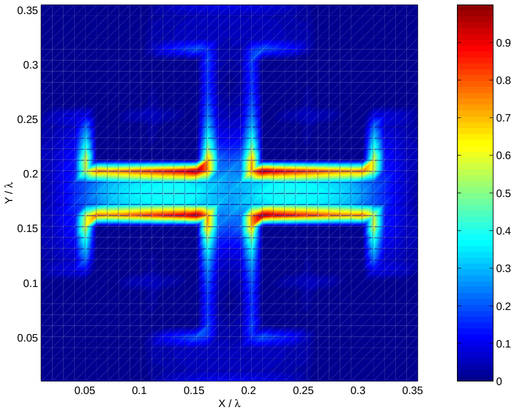

Fig. 8.23: *Normalized total surface current density at 8 GHz*

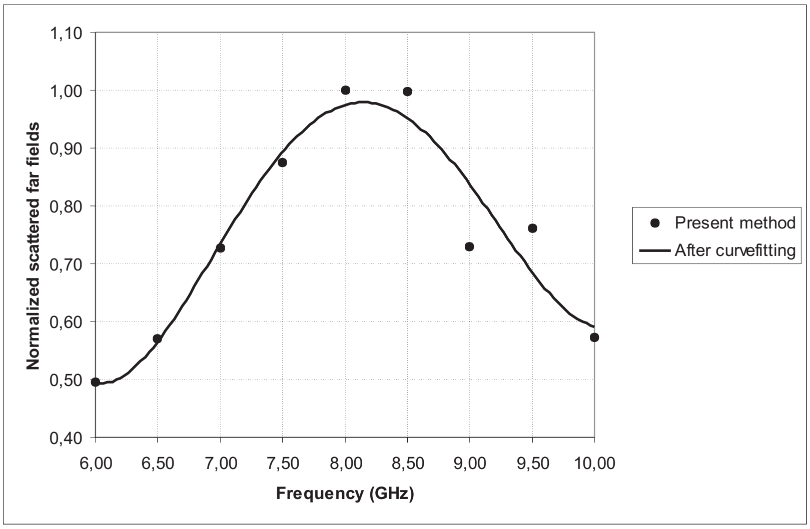

Fig. 8.24: *Scattering patterns of a free standing 4 by 4 array of Jerusalem crosses at frequencies 6 - 10 GHz*

An eight by eight array of loaded Jerusalem crosses is also investigated in the frequency range of 6 GHz - 10 GHz for their scattering properties (Fig 8.28). The normalized total surface current density at 8 GHz is shown in Fig 8.29. It reveals the subtle details of the current distribution of a finite FSS. In order to highlight the accuracy of the present method, an already published result for an infinite FSS consisting of the same elements is given in Fig. 8.30, where the reflection coefficient is illustrated as a function of frequency. It agrees well with both scattering patterns in Fig. 8.24 and 8.28 based on the present method even though the finite FSSs tried out here are quiet small. Hence, the present method would be a significant tool when analyzing different planar finite FSS and optimizing their behavior for some particular application. For example, Fig. 8.25 - 8.27 imply that the small secondary crosses used to load the Jerusalem cross do not have a significant effect on the performance of the FSS due to their negligible surface current densities. This fact is also obvious in Fig. 8.30.

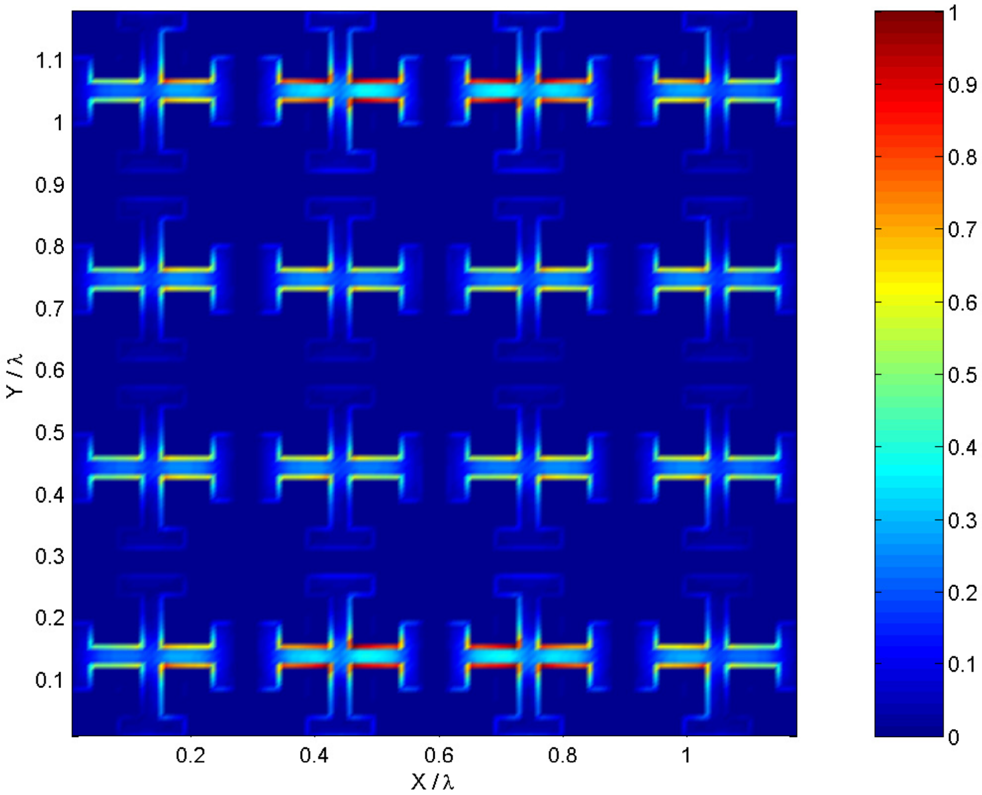

Fig. 8.25: *Normalized surface current density on 4 by 4 array of FSS at 6 GHz*

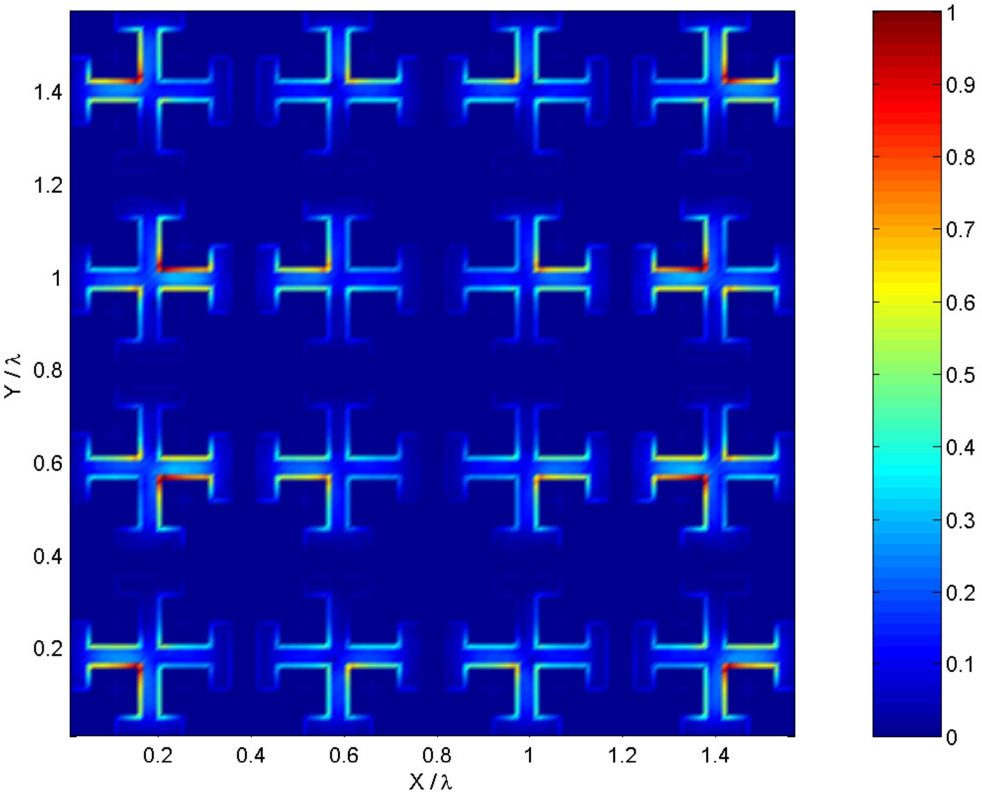

Fig. 8.26: *Normalized surface current density on 4 by 4 array of FSS at 8 GHz*

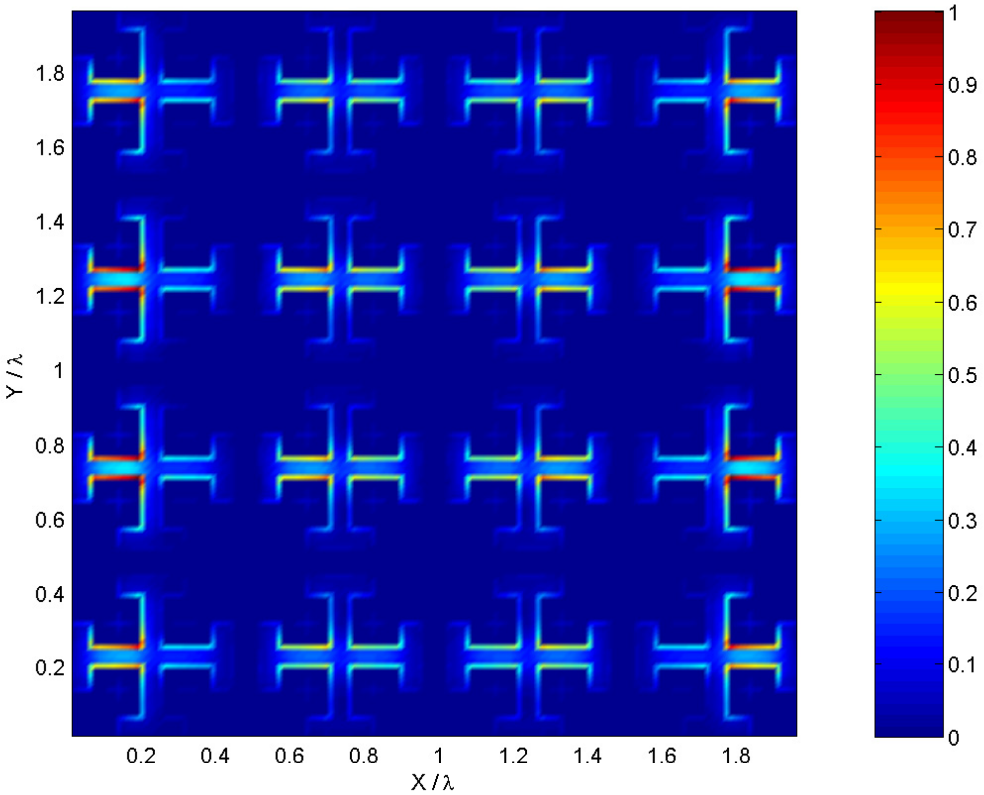

Fig. 8.27: *Normalized surface current densit on 4 by 4 array of FSS at 10 GHz*

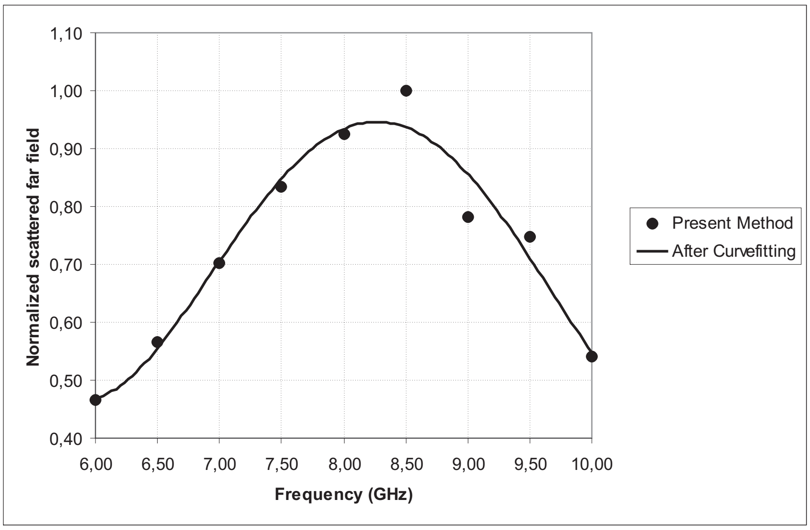

Fig. 8.28: *Scattering patterns of a free standing 8 by 8 array of Jerusalem crosses at frequencies 6 - 10 GHz*

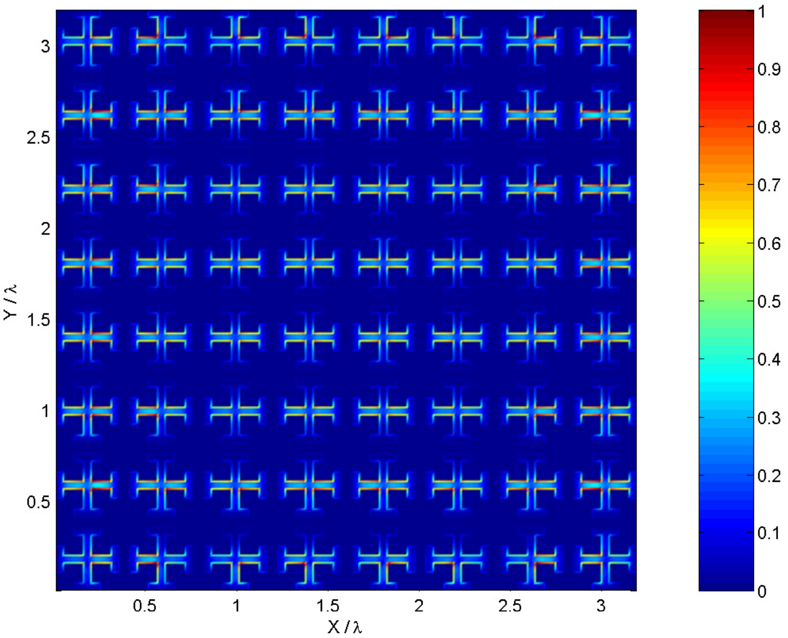

Fig. 8.29: *Normalized surface current density on 8 by 8 array of FSS at 8 GHz*

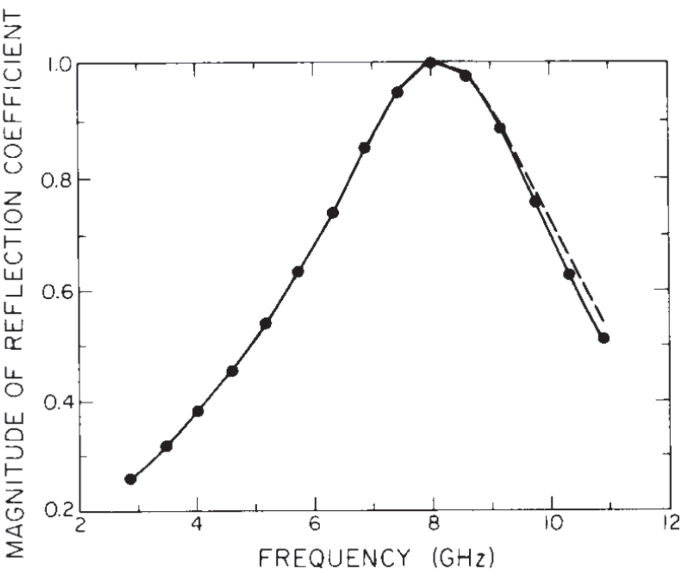

Fig. 8.30: *Magnitude of reflection coefficient versus frequency for an infinite structure of loaded Jerusalem crosses in Fig. 8.18 (solid line) and unloaded (i.e. without the secondary crosses) Jerusalem crosses (dashed line) [69]*

Chapter 9

Discussion and Conclusions

This chapter starts with a brief discussion of the pros and cons of the present method. We then summarize the major conclusions, which have already been drawn in the previous chapters. A short list of future directions is also appended at the end.

9.1 Discussion

The various forms of MoM have been applied in analyzing stratified planar structures for decades. The favorite has been MoM in the spectral domain. The space domain MoM has on the other hand been applied only when the necessary spatial Green's functions are available in closed forms. In the present work, we have focused on applying space domain MoM for arbitrary stratified planar structures even if the spatial Green's functions are not available in such a prerequisite form.

In addition, an attempt has also been made here to develop a more efficient space domain MoM than the conventional space domain MoM. Each major step of the MoM was addressed separately and enhanced independently. Finally, all these subsystems were linked together to form a complete space domain MoM suited for analyzing arbitrary planar stratified structures. The method was then realized in MATLAB codes. MATLAB was selected solely due to its user-friendly interface and easy-to-use software routines available for graphical illustrations. The method was then applied to practical planar stratified structures such as microstrip patch arrays and frequency selective surfaces. The MATLAB codes implementing the present method were far superior to MATLAB codes implementing an conventional MoM. They also led to accurate results that were comparable with the results obtained by commercial software and measurements. We have also attempted to justify the efficiency of the present method by simply comparing each novel method with the corresponding conventional method. These comparisons were done either based on simulations, mathematical or logical reasonings.

Nevertheless, we were unable to affirm the efficiency of the final product of the present method due to unavailability of a proper reference code for the conventional space domain MoM. A direct and very unfair comparison with commercial codes showed that the present method still needs some improvements in order to be commercially competitive. Such comparison is truly unfair because these commercial software are often well optimized with respect to processing time and memory usage. However, this does not imply that the methods behind the commercial software are more efficient than the method developed here.

9.2 Conclusions

In the following, we summarize the conclusions made in the previous chapters.

The DCIM was introduced to find closed form expressions for spatial Green's functions that are critical to the space domain MoM implementation. The present formulation of DCIM was equally accurate and more efficient compared to traditional way of evaluating Sommerfeld integrals based on the corresponding spectral Green's functions. The robust GPOF method was applied in extracting the complex exponential functions from a known discrete data set. The examples of closed form expressions derived by DCIM were very accurate when compared with so-called exact spatial Green's functions found by evaluating the Sommerfeld integrals numerically. Moreover, the DCIM was far more efficient compared with the numerical integration methods. Therefore, we can safely conclude that the closed form expressions derived by DCIM are accurate, and they make the space domain MoM more efficient. In other words, DCIM facilitates the application of space domain MoM to large arbitrary scatterers on planar stratified media.

The resulting closed form expressions for the spatial Green's functions comprise complex exponential terms. During the matrix filling process, some of these terms led to singular two-dimensional exponential integrals, which were time-consuming and inaccurate if evaluated using common quadrature methods. We therefore generalized the method suggested in [49]. This method was shown to be very accurate and efficient when applied to singular 2D exponential integral. Since this particular method could be useful in evaluating 2D generalized exponential integrals encountered in other context, it was formulated as a simple numerical integration algorithm that can easily be integrated with other software as well. It is thus concluded that the present extension results in more efficient space domain MoM that is applicable to large planar scatterers.

Conjugate gradient fast Fourier transform was employed in solving the linear equation system resulting from the space domain MoM. We implemented a compact formulation of CG-FFT by exploiting the implicit symmetries and the linear invariant property inherent in coefficient matrices. It was found that this novel formulation reduces memory requirement significantly without compromising the accuracy. As predicted in the literature, the number of iterations needed to achieve a solution of some given accuracy was shown to be quiet smaller than the theoretically predicted number of iterations required for convergence, which is equal to the number of unknowns. The convergence was mostly monotone and fast. The present algorithm was shown to be far superior to the direct matrix inversion algorithms when large number of unknowns were involved. The method was also flexible, in the sense that one could easily modify the planar metal structure without repeating the process of matrix filling. However, the present form of CG-FFT is unable to solve the same structure for various excitations, either consequently or in parallel, without restarting the iterations. Nevertheless, we can confidently declare that the present version of CG-FFT effectively extends the application of space domain MoM to large planar scatterers in stratified media.

The present method was applied to analyze stratified planar structures and finite FSS structures. The results were found to be in agreement with the results obtained from the contemporary commercial software and the results stated in publications. In the case of the stand-alone patch and three element patch array, the simulated and measured S-parameters were comparable, thus leading to the ultimate conclusion that the present space domain MoM is an accurate and efficient tool for analyzing large arbitrary planar scatterers in stratified structures. However, the current version still requires further optimizations in order to be an attractive competitor to the commercial software based mostly on spectral domain MoM.

9.3 Suggestions for Future Work

The work performed here has basically been focused on methods improving the classical space domain method of moments such that it can handle larger and more complex 2D planar structures. Each step of the classical space domain MoM is improved, thus achieving an overall efficient method. From the experience gained during this work, we believe that there is still room for further improvements. Such improvements are desired and feasible. Hence the following specific research activities are suggested for further elaboration.

9.3.1 Implementation

The method is implemented in MATLAB, which is not efficient compared to more dedicated software languages like C, C++, Fortran, etc. So in order to compare the present method with commercially available software, it is advisable to implement the present method in more efficient programming language and codes. It is also necessary to identify the existing bottlenecks in the present implementation. For example, the calculation of 2D Fourier transforms in implementing the current version of CG-FFT has shown to consume a significant amount of processing time and memory. Such bottlenecks can presumably be eliminated by writing tailor-made program codes.

9.3.2 Discrete complex image method

The present version of DCIM does not explicitly take care of surface wave contributions. For thicker dielectric layers with higher dielectric constant, surface waves contribute significantly to the far field just above the stratified planar structures. Thus, the extraction of surface wave poles as suggested by [28] would be preferred. It will also be necessary to address the issues connected to numerical stability of DCIM more precisely and quantitatively to further confirm its robustness.

9.3.3 Method of moments

The present method is implemented using a uniform grid of rooftop subdomain basis and testing functions. It enables the analysis of arbitrarily complex structures at the cost of efficiency. For this method to be competitive in analyzing general stratified structures, a way of integrating non-uniform grids of subdomain basis and testing functions, or eventually combining them with entire domain basis and testing functions, has to be found. In addition, this should be done in such a way that the existing symmetries in the coefficient matrices do not disappear entirely.

9.3.4 De-embedding

Although we devoted a short chapter to de-embedding methods, it is not by any means intended to cover the de-embedding techniques in detail. Consequently, we only presented the most simple and straightforward feeding technique, the microstrip feedlines and the ways of extracting corresponding S parameters from it. For accurate results, an extended microstrip feedline was used in simulations, subsequently increasing the processing time and memory requirements drastically. Therefore more efficient de-embedding methods need to be suggested for microstrip feedlines and other feeding techniques. For example, in [70], [71] and [72], a novel model suitable for planar stratified media is discussed. It avoids extended feedlines and takes into account the effect of the finite ground plane, thus acquiring more accurate results.

Appendix

9.4 List of publications

Following is a list of articles pulbished by the author during the course of this thesis.

1. J. K. H. Gamage, "Conjugate Gradient Fast Fourier Transform Method: A New Compact Formulation", *Antnene 03 Nordic Antenna Symposium,* Kalmar, Sweden, pp 333 - 340, May 2003
2. J. K. H. Gamage, "An efficient space domain moment method for analysing large planar structures", *9th cost 260 Meeting and workshop on smart antennas*, Gothenburg, Sweden*,* pp 11-14, May 2001
3. J. K. H. Gamage, " Efficient method of moment for comapact large planar scatterers in homogeneous medium", *ICAP 2001(IEE Eleventh International conference on Antennas and Propagation),* Manchester, UK, vol. 2, pp 741- 744, April 2001
4. J. K. H. Gamage, "Accurate numerical evaluation of the two dimensional generalized exponential integral", *APSYM (Antenna and propagation symposium 2000),* cochin India*,* pp 222-227, December 2000.
5. J. K. H. Gamage, "An efficient method for calculating mutual coupling in planar antenna arrays", *Antnene 00 Nordic Antenna Symposium*, Lund, Sweden, pp 69-74, September 2000

References

[1] A. P. M. Zwamborn and P. M. Van Den Berg, “A weak form of the conjugate gradient FFT method for plate problems,” *IEEE Transactions on Antennas and Propagation*, vol. 39, pp. 224–228, February 1991.

[2] C. A. Balanis, *Advanced Engineering Electromagnetics*. New York: John Wiley & Sons, 1989.

[3] B. A. Brynjarsson, *A Study of Printed Antennas in Layered Dielectric Media*. PhD thesis, Institutt for teleteknikk Trondheim, Norges Tekniske Høgskole, Universitetet i Trondheim, 1995.

[4] R. F. Harrington, *Time-Harmonic Electromagnetic Fields*. New York: McGraw-Hill, 1961.

[5] J. R. James and P. S. Hall, *Hamdbook of Microstrip Antennas*. London: Peter Peregrinus on behalf of the Institution of Electrical Engineers, 1989.

[6] K. A. Michalski and D. Zheng, “Electromagnetic scattering and radiation by surfaces of arbitrary shape in layered media, part 1 : Theroy,” *IEEE Transactions on Antennas and propagation*, vol. 38, no. 3, pp. 335–344, 1990.

[7] Y. L. Chow, N. Hojjat, S. Safavi-Naeini, and R. Faraji-Dana, “Spectral Green’s functions for multilayer media in a convienient computational form,” *IEE Proceedings - Microwaves, Antennas and Propagation*, vol. 145, pp. 85–91, February 1998.

[8] R. M. Ikmo Park and M. I. Aksun, “Numerically efficient analysis of planar microstrip configurations using closed-form Green’s functions,” *IEEE Transactions on Microwave Theory and Techniques*, vol. 43, pp. 394–400, February 1995.

[9] J. R. Mosig and F. E. Gardiol, “A dynamical radiation model for microstrip structures,” *Advances in Electronics and Electron Physics*, vol. 59, pp. 139–237, 1982.

[10] H. Thonstad, *Analysis and Design of Cavity-Backed Planar Antennas*. PhD thesis, Institutt for Teleteknikk, Norges Teknisk-naturvienskapelige Universitet i Trondheim, 1996.

[11] A. Sommerfeld, *Partial Differential Equations in Physics*. New York: Academic Press, 1949.

[12] R. C. Hsieh and J. T. Kuo, "Fast evaluation of the sommerfeld integrals for green's functions of open microstrip structures," *IEEE AP-S Int. Symp./URSI Meeting*, vol. 1, pp. 1826–1829, 1998.

[13] U. V. Gothelf and A. Østergaard, "Full-wave analysis of a two slot microstrip filter using a new algorithm for computation of the spectral integrals," *IEEE Transactions on Microwave Theory and Techniques*, vol. 41, pp. 101–108, 1993.

[14] E. Kreyszig, *Advanced Engineering Mathematics.* Canada: John Wiley & Sons Inc, 1988.

[15] T. Itoh, *Numerical Techniques for Microwave and Millimeter-Wave Passive Structures.* New York: Wiley, 1989.

[16] A. Sidi, "The numerical evaluation of very oscillatroy infinite integrals by extrapolation," *Mathematics of Computation*, vol. 38, no. 158, pp. 517–529, 1982.

[17] A. Alaylioglu, G. A. Evans, and J. Hyslop, "The evaluation of oscillatory integrals with infinite limits," *Journal of Computational Physics*, vol. 13, pp. 433–438, 1973.

[18] N. Kinayman and M. I. Aksun, "Comparative study of acceleration techniques for integrals and series in electromagnetic problems," *Antennas and Propagation Society International Symposium*, vol. 2, pp. 1037–1040, 1995.

[19] P. Wynn, "On the covergence and stability of the epsilon algorithm," *SIAM Journal on Numerical Analysis*, vol. 3, no. 1, pp. 91–122, 1966.

[20] D. Shanks, "Non-linear transformations of divergent and slowly convergent sequences," *Journal of Mathematics and Physics*, vol. 34, pp. 1–42, 1955.

[21] M. Abramowitz and I. A. Stegen, *Handbook of Mathematical Functions.* New York: Dover, 1965.

[22] W. T. V. William H. Press, Saul A. Teukolsky and B. P. Flannery, *Numerical Recipes in C++ : The Art of Scientific Computing.* UK: Cambridge University Press, 2002.

[23] A. K. Bhattacharyya, *Electromagnetic Fields in Multilayered Structures : Theory and Applications.* Boston: Artech House, 1994.

[24] P. Silvester, "TEM wave properties of microstrip transmission lines," *Proc. Inst. Elec. Eng.*, vol. 115, pp. 43–48, 1968.

[25] Y. L. Chow, "An approximate dynamic spatial Green's function for microstriplines," *IEEE Transactions on Microwave Theroy and Techniques*, vol. 26, no. 12, pp. 978–983, 1978.

[26] Y. L. Chow, "An approximate dynamic Green's function in three dimensions for finite length microstripline," *IEEE Transactions on Microwave Theroy and Techniques*, vol. 28, no. 4, pp. 393–397, 1980.

[27] I. V. Lindell and E. Alanen, "Exact image throry for the Sommerfeld half-space problem, part 1: Vertical magnetic dipole," *IEEE Transactions on Antennas and Propagation*, vol. 32, pp. 126–133, February 1984.

[28] D. G. Fang, J. J. Yang, and G. Y. Delisle, “Discrete image theory for horizontal electric dipoles in a multilayered medium,” *IEE Proceedings-Microwaves, Antennas and Propagation*, vol. 135, pp. 297–303, October 1988.

[29] M. I. Aksun, “A robust approach for the derivation of closed-form green’s functions,” *IEEE Transactions on Microwave Theory and Techniques*, vol. 44, pp. 651–658, May 1996.

[30] Y. L. Chow, J. J. Yang, D. G. Fang, and G. E. Howard, “A colsed-form spatial Green’s function for the thick microstrip substrate,” *IEEE Transactions on Microwave Theory and Techniques*, vol. 39, pp. 588–592, March 1991.

[31] R. A. Kipp and C. H. Chan, “Complex image method for sources in bounded regions of multilayer structures,” *IEEE Transactions on Microwave Theory and Techniques*, vol. 42, pp. 860–865, May 1994.

[32] L. Alatan, M. Aksun, and M. Birand, “Computationally efficient analysis and design of printed structures,” *Proceedings of IEEE AP-S International Symposium and URSI Radio Science Meeting,, Baltimore, Maryland*, vol. 1, pp. 276–279, July 1996.

[33] de Prony Baron Gaspard Riche, “Essai éxperimental et analytique: Sur les lois de la dilatabilité de fluides élastique et sur celles de la force expansive de la vapeur de l’alkool, à différentes températures,” *Journal de l’École Polytechnique*, vol. 1, pp. 24–76, 1795.

[34] G. Strang, *Linear Algebra and its Applications.* New York: Sunders College Publishing, third ed., 1988.

[35] M. S. Lawrence, *Digital Spectral Analysis with Applications.* Prentice-Hall, 1987.

[36] C. W. Therrien, *Discrete Random Signals and Statistical Signal Processing.* Englewood Cliffs, NJ: Prentice Hall, 1992.

[37] A. J. Mackay and A. McCowen, “An improved pencil-of-functions method and comparisons with traditional methods of pole extraction,” *IEEE Transactions on Antennas and Propagation*, vol. 35, pp. 435–441, April 1987.

[38] Y. Hua and T. K. Sarkar, “Generalized pencil-of-function method for extracting poles of an EM system from its transient response,” *IEEE Transactions on Antennas and Propagation*, vol. 37, pp. 229–234, February 1989.

[39] C. B. Moler and G. Stewart, “An algorithm for generalized matrix eigenvalue problems,” *SIAM journal on numerical analysis*, vol. 10, no. 2, 1973.

[40] M. L. V. Blaricum and R. Mittra, “Problems and solutions associated with Prony’s method for processing transient data,” *IEEE Transactions on Antennas and Propagation*, vol. 26, no. 1, pp. 174–182, 1978.

[41] R. F. Harrington, *Field Computation by Moment Methods.* New York: Macmillan Company, 1968.

[42] C. A. Balanis, *Antenna Theory : Analysis and Design.* New York: John Wiley & Sons, Inc., second ed., 1997.

[43] J. J. Wang, *Generalized Moment Methods in Electromagnetics.* New York: Wiley, 1991.

[44] M. I. Aksun and R. Mittra, "Choices of expansion and testing functions for the method of moments applied to a class of electromagnetic problems," *IEEE Transactions on Microwave Theroy and Techniques*, vol. 41, no. 3, pp. 503–509, 1993.

[45] M. I. Aksun, "Admissible class of basis and testing funcitions for the method of moments in electromagnetic problems," in *Antennas and Propagation Society International Symposium, 1992*, vol. 3, pp. 1657–1660, 1992.

[46] M. I. Aksun, "On the use of discontinuous expansion and testing functions in the method of moments for electromagnetic problems," in *Antennas and Propagation Society International Symposium, 1993*, vol. 1, pp. 68–71, 1993.

[47] L. Alatan, M. I. Aksun, K. Mahadevan, and M. T. Birand, "Analytical evaluation of the MoM matrix elements," *IEEE Transactions on Microwave Theory and Techniques*, vol. 44, pp. 519–525, April 1996.

[48] R. C. Hsieh and J. T. Kuo, "Fast full-wave characterization of arbitrary planar microstrip geometries," in *Microwave Conference Proceedings*, (Asia Pacific Microwave Conference), pp. 685–688, 1997.

[49] S. A. Martin Gimersky and J. Bornemann, "Numerical evaluation of the two-dimensional generalized exponential integral," *IEEE Transactions on Antennas and Propagation*, vol. 44, pp. 1422–1425, October 1996.

[50] D. Kincaid and W. Cheney, *Numerical Analysis : Mathematics of Scientific Computing.* New York: Brooks/Cole Publishing Company, 2nd ed., 1996.

[51] R. L. Burden and J. D. Faires, *Numerical Analysis.* Boston: PWS-Kent, 5th ed., 1993.

[52] T. N. L. Patterson, "The optimum addition of points to quadrature formulae," *Mathematics of Computation*, vol. 22, pp. 847–856, 1968.

[53] T. N. L. Patterson, "Algorithm for automatic numerial integration over a finite interval [D1](Algorithm 468)," *Communicatins of the ACM (CACM)*, vol. 16, pp. 694–699, November 1973.

[54] F. T. Krogh and W. V. Snyder, "Algorithm 699 : A new representation of Patterson's quadrature formulae," *ACM Transactions on Mathematical Software*, vol. 17, pp. 457–461, December 1991.

[55] C. H. Edwards Jr. and D. E. Penney, *Calculus and Analyitc Geometry.* New Jersey: Prentice-Hall Inc, third ed., 1990.

[56] M. F. Cátedra, J. G. Cuevas, and L. Nuño, "A scheme to analyze conduction plates of resonant size using the conjugate gradient method and the fast Fourier transform," *IEEE Transactions on Antennas and Propagation*, vol. 36, pp. 1744–1752, December 1988.

[57] D. H. Preis, "The toeplitz matrix : ITs occurence in antenna problems and a rapid inversion algorithm," *IEEE Transactions on Antennas and Propagation*, vol. 3, pp. 204–206, 1972.

[58] M. F. Catedra, R. P. Torres, J. Basterrechea, and E. Gago, *The CG-FFT Method : Application of Signal Processing Techniques to Electromagnetics.* Boston: Artech House, Inc., 1994.

[59] T. K. Sarkar, K. R. Siarkiewicz, and R. F. Stratton, "Survey of numerical methods for solution of large systems of linear equations for electromagnetic field problems," *IEEE Transactions on Antennas and Propagation*, vol. AP-29, pp. 847–856, 1981.

[60] J. G. Proakis and D. G. Manolakis, *Digital Signal Processing Principles, Algorithms, and Applications.* New York: Macmillan Publishing Company, 1992.

[61] A. F. Peterson and R. Mittra, "Convergence of the conjugate gradient method when applied to matrix equations representing electromagnetic scattering problems," *IEEE Transactions on Antennas and Propagation*, vol. 34, no. 12, pp. 1447–1454, 1986.

[62] C. W. Yuan Zhuang, Ke-Li Wu and J. Litva, "A combined full-wave CG-FFT method for rigorous analysis of large microstrip antenna arrays," *IEEE Transactions on Antennas and Propagation*, vol. 44, pp. 102–109, January 1996.

[63] A. F. Peterson, S. L. Ray, and R. Mittra, *Computational Methods for Electromagnetics.* New York: IEEE Press, 1997.

[64] D. M. Pozar, *Microwave Engineering.* New York: Addison-Wesley Publishing Company, Inc., 1990.

[65] P. B. Katehi and N. G. Alexopoulos, "Frequency-dependent chracteristics of microstrip discontinuities in millimeter wave intergrated circuits," *IEEE Transactions on Microwave Theory and Techniques*, vol. 33, no. 10, pp. 1029–1035, 1985.

[66] S. V. Marshall and G. G. Skitek, *Electromagnetic Concepts and Applications.* Englewood Cliffs, N.J.: Prentice-Hall, 1990.

[67] M. D. Deshpande and M. C. Bailey, "Input impedance of microstrip antennas," *IEEE Transactions on Antennas and Propagation*, vol. 30, pp. 645–650, 1982.

[68] B. A. Munk, *Frequency Selective Surfaces : Theory and Design.* NewYork: John Wiley & Sons Inc, 2000.

[69] R. Mittra, C. H. Chan, and T. Cwik, "Techniques for analyzing frequency selective surfaces - a review," *Proceedings of the IEEE*, vol. 76, no. 12, pp. 1593–1615, 1988.

[70] G. V. Eleftheriades and J. R. Mosig, "On the network characterization of planar passive circuits using the method of moments," *IEEE Transactions on Microwave Theroy and Techniques*, vol. 44, no. 3, pp. 438–445, 1996.

[71] F. Tiezzi, A. Alvarez-Melcon, and J. R. Mosig, "A new excitation model for microstrip antennas on finite size ground planes," *AP-2000 Millennium Conference on Antennas and Propagation*, 2000.

[72] F. Tiezzi, A. Alvarez-Melcon, and J. Mosig, "A new excitation model for probe-fed printed antennas on finite ground planes," *Journal of Applied Computational Electromagnetics Society*, vol. July, pp. 115–125, 2000.